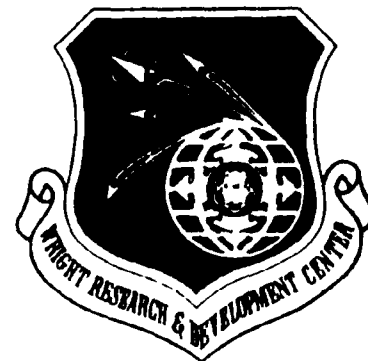


WRDC-TR-89-2047



HEAT PIPE AND THERMAL ENERGY STORAGE AND CORROSION STUDIES (1988)

Arizona State University
Department of Chemical
Bio & Materials Engineering
Tempe AZ 85287

June 1989

Final Report For Period October 1987 - September 1988

Approved for public release; distribution is unlimited

AD-A212 655

AERO PROPULSION AND POWER LABORATORY
WRIGHT RESEARCH AND DEVELOPMENT CENTER
AIR FORCE SYSTEMS COMMAND
WRIGHT-PATTERSON AIR FORCE BASE, OHIO 45433-65635



89 9 06 075

NOTICE

When Government drawings, specifications, or other data are used for any purpose other than in connection with a definitely Government-related procurement, the United States Government incurs no responsibility or any obligation whatsoever. The fact that the government may have formulated or in any way supplied the said drawings, specifications, or other data, is not to be regarded by implication, or otherwise in any manner construed, as licensing the holder, or any other person or corporation; or as conveying any rights or permission to manufacture, use, or sell any patented invention that may in any way be related thereto.

This report is releasable to the National Technical Information Service (NTIS). At NTIS, it will be available to the general public, including foreign nations.

This technical report has been reviewed and is approved for publication.

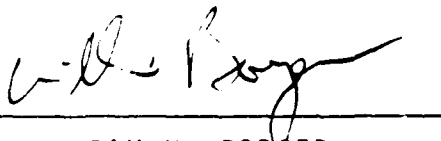


MICHEAL J. MORGAN
Power Technology Branch
Aerospace Power Division
Aero Propulsion and Power Laboratory



JERRY E. BEAM
Power Technology Branch
Aerospace Power Division
Aero Propulsion and Power Laboratory

FOR THE COMMANDER



WILLIAM U. BORGER
Chief, Aerospace Power Division
Aero Propulsion & Power Laboratory

If your address has changed, if you wish to be removed from our mailing list, or if the addressee is no longer employed by your organization please notify WRDC/ProS, WPAFB, OH 45433-6563 to help us maintain a current mailing list.

Copies of this report should not be returned unless return is required by security considerations, contractual obligations, or notice on a specific document.

UNCLASSIFIED

SECURITY CLASSIFICATION OF THIS PAGE

REPORT DOCUMENTATION PAGE

Form Approved
OMB No. 0704-0188

1a REPORT SECURITY CLASSIFICATION UNCLASSIFIED		1b RESTRICTIVE MARKINGS N/A	
2a SECURITY CLASSIFICATION AUTHORITY N/A		3 DISTRIBUTION/AVAILABILITY OF REPORT Approved for public release, distribution is limited	
2b DECLASSIFICATION/DOWNGRADING SCHEDULE N/A		4 PERFORMING ORGANIZATION REPORT NUMBER(S)	
6a NAME OF PERFORMING ORGANIZATION Arizona State University		6b OFFICE SYMBOL (If applicable)	
6c ADDRESS (City, State, and ZIP Code) Dept of Chemical, Bio & Materials Engineering Tempe AZ 85287 ATTN: Dr Dean Jacobson		7a NAME OF MONITORING ORGANIZATION Aero Propulsion and Power Laboratory Wright Research & Development Center (WRDC/POOS-3)	
8a NAME OF FUNDING/SPONSORING ORGANIZATION Strategic Defense Initiative		8b OFFICE SYMBOL (If applicable) SDIO/SLKT	
8c ADDRESS (City, State, and ZIP Code) The Pentagon Washington DC 20301-7100		9 PROCUREMENT INSTRUMENT IDENTIFICATION NUMBER F33615-86-C-2723	
10 SOURCE OF FUNDING NUMBERS		10 SOURCE OF FUNDING NUMBERS	
PROGRAM ELEMENT NO 63224C		PROJECT NO 4L12	TASK NO 40
WORK UNIT ACCESSION NO 14			
11 TITLE (Include Security Classification) Heat Pipe and Thermal Energy Storage and Corrosion Studies (1988)			
12 PERSONAL AUTHOR(S) Krishnamurthy, Mohan, Dalton, Patrick, and Jacobson, Dean			
13a. TYPE OF REPORT Final Report	13b. TIME COVERED FROM 20OCT87 TO 30SEP88	14. DATE OF REPORT (Year, Month, Day) JUNE 1989	15. PAGE COUNT
16. SUPPLEMENTARY NOTATION			
17. COSATI CODES		18. SUBJECT TERMS (Continue on reverse if necessary and identify by block number)	
FIELD	GROUP	SUB-GROUP	
		Thermal Energy Storage, eutectic fluoride, corrosion -	
19 ABSTRACT (Continue on reverse if necessary and identify by block number) PART I - Corrosion degradation analysis was performed on a set of three Inconel 617 Thermal Energy Storage capsules filled with different eutectic fluoride mixtures of LiF, MgF ₂ , NaF and KF which were thermally cycled near 1000 K for 10,000 hours. These capsules were cut out and various sections were metallographically studied by Optical and Scanning Electron microscopy and by elemental X-ray mapping. Chemical analyses on the metallic container were performed using the Electron Probe Micro-analyser and that of the salts by Atomic Absorption Spectroscopy. It was determined that the container material did not suffer significant micro-structural damage except for tiny pits near the edge in contact with the salts and some voids near the surface exposed to vacuum which could not be positively identified as due to corrosion. The region extending to about 50 microns from the inner edge is contact with salt and about 30 microns from the outer edge exposed to vacuum were found to be depleted mainly of Aluminum and to a lesser extent Chromium. The profile of the depletion near the inner edge was fitted with a model diffusion curve and a semi quantitative estimate of the diffusion (Continued on back)			
20 DISTRIBUTION/AVAILABILITY OF ABSTRACT <input checked="" type="checkbox"/> UNCLASSIFIED/UNLIMITED <input type="checkbox"/> SAME AS RPT <input type="checkbox"/> DTIC USERS		21. ABSTRACT SECURITY CLASSIFICATION UNCLASSIFIED	
22a NAME OF RESPONSIBLE INDIVIDUAL MICHEAL J. MORGAN/JERRY E. BEAM		22b TELEPHONE (Include Area Code) (513) 255-2922	22c OFFICE SYMBOL WRDC/POOS-3

DD Form 1473, JUN 86

Previous editions are obsolete.

SECURITY CLASSIFICATION OF THIS PAGE

UNCLASSIFIED

19. coefficient of Al yielded a value of $D_{Al} = 1.0 \times 10^{-13} \text{ cm}^2/\text{sec}$. The outer edge depletion was attributed to vaporization in vacuum at this temperature based on the vapor pressures of the alloy constituents. Some thermodynamic equilibrium calculations were performed to explain the presence of Al in the salts and concluded that equilibrium had not reached in the reaction between the container and the salts due to a possible diffusion control in the transport of Al from the container to the salt.

PART II - The spectral emissivity of a material is a basic material property. The intent of this investigation is to measure this property by measuring the bidirectional reflectivity of various superalloys and stainless steels at 10.6 microns, the nominal output wavelength of a carbon dioxide laser. The measurements of the spectral emissivity of these materials will be conducted as a function of temperature and angle of incidence of the laser beam. The tests will be run in air so the results will reflect the spectral emissivity of the oxidized, not polished, alloys.

Accession For	
NTIS GRA&I	<input checked="" type="checkbox"/>
DTIC TAB	<input type="checkbox"/>
Unannounced	<input type="checkbox"/>
Justification	
By	
Distribution/	
Availability Codes	
Avail and/or	
Dist	Special
A-1	

**HEAT PIPE AND THERMAL ENERGY
STORAGE AND CORROSION STUDIES**

Final Report for 1988

for

TEXAS A & M RESEARCH FOUNDATION

Room 121

Old USDA Bldg.

Wellborn and University

College Station, TX 77843

Attention: Dr. Fletcher

Prime Contract: F33615-86-C-2723,T3

Agreement: L700039

Project: RF 5729

by

Mohan Krishnamurthy

Patrick Dalton

Dean L. Jacobson

Department of Chemical, Bio & Materials Engineering

Arizona State University

PART I

HIGH TEMPERATURE CORROSION ANALYSIS OF INCONEL 617
THERMAL ENERGY STORAGE CAPSULES

TABLE OF CONTENTS

	Page
LIST OF TABLES	2
LIST OF MICROGRAPHS AND FIGURES	3
INTRODUCTION	5
BACKGROUND AND LITERATURE REVIEW	7
THEORETICAL BACKGROUND	12
EXPERIMENTAL PROCEDURE AND ANALYSIS	18
DISCUSSION	27
CONCLUSION	35
APPENDIXES	
A ELECTROCHEMICAL METHODS	36
B MICROGRAPHS AND FIGURES	40
C DATA TABLES	76
REFERENCES	80

LIST OF TABLES

Table I.	Weight Percent Compositions of the Eutectic Salts.....	77
Table II.	Nominal Composition of Container Alloy in Weight Percent.....	77
Table III.	Weight Percent Composition of Alloy #17 Near Inner Edge.....	78
Table IV.	Weight Percent of Al and Cr in the Tested Salts.....	78
Table V.	Weight Percent Composition of Alloy #17 Near Outer Edge.....	79

LIST OF MICROGRAPHS AND FIGURES

Figure	Page
1. Graph showing calculated equilibrium amounts of metal in salts [13].	41
2. Internal fluoridation in a Ni - Cr alloy with F atmosphere[18]	41
3. Thermal Energy Storage (TES) capsule.....	42
4. Cut section photographs showing salt solidification profile	43
5. Radiographs of TES capsules showing no detectible.....	44
6. Sample preparation and mounting	45
7. General microstructure of test samples.....	46
8. Microstructure of untested sample of I617.....	47
9. TES capsule wall showing inner edge in contact with salts and outer edge exposed to vacuum.	48
10. Inner edge damage at various magnifications.....	49
11. Section of tube wall showing damage on outer edge exposed to vacuum	50
12. Micrograph showing outer edge damage at higher magnification.....	50
13. End cap regions at various magnifications.....	51
14. Microstructure across the gap near the end cap region	52
15. Similar micrograph showing microstructure across gap	52
16. Microstructure near end cap showing edge (X 500).....	53
17. Microstructure on opposite side of gap (X 500).....	53
18. Series of discontinuities in the end cap region.....	54
19. Discontinuous gaps in the end cap regions	55
20. Elongated grains probably due to extrusion or heat effects	55
21. SEM images of tested samples	56
22. SEM images of sample #20.....	57

23.	Composite SEI and BSE image of sample # 17 for comparison	58
24.	Energy Dispersive X-ray spectrum (EDS) of tested sample (#20).....	58
25.	EDS plots of the various phases in the samples	60
26.	EDS plot of untested sample of I 617	60
27.	Details of composition of untested sample of I 617.....	61
28.	Microstructure of the inner edge in contact with the salt.....	62
29.	Images near the inner edge of sample # 17.....	63
30.	Microstructural damage near the outer edge exposed to vacuum	64
31.	Extent and form of outer edge damage	65
32.	Characterization of the eutectic salt	67
33.	Composite X-ray map of Cr K_{α} and Video image on the right	67
34.	General microstructure and elemental distribution	68
35.	Al distribution showing slight indication of near edge depletion	69
36.	Elemental maps near end cap region.....	70
37.	Al distribution near end cap showing alumina in crevice due to polishing.....	71
38.	Normalised change in concentration of constituents in #14	71
39.	EPMA determinations of the concentration profile across the tube wall upto 50 microns from inner edge	72
40.	Plots of the weight percent concentration of Al versus the distance from the inner edge of the tube wall as determined by EPMA.....	73
41.	Plot of the average concentration of Al as determined from Fig.40.above.....	73
42.	Plots based on the diffusion model with varying C_0 and D and compared to the average experimental values obtained from above	74
43.	Diffusion curve based on the best fitting C_0 and D from least squares analysis and compared with the experimental curve.....	74
44.	Concentration profile of Al near the outer edge exposed to vacuum	75

INTRODUCTION

Thermal energy storage using the latent heat of fusion phase change is an attractive concept for use in solar dynamic space power systems and other terrestrial applications [1- 4]. The basis of this type of heat storage is the absorption of latent heat by a solid phase change material during melting and the subsequent evolution of this heat during resolidification. This process has been envisaged for use in supplying isothermal energy to power heat engines which would provide refrigeration to orbiting spacecraft [5]. Ideally, during the sunlit portion of each orbit, these phase change materials would melt and thereby store the heat in the form of latent heat which could be utilized during the eclipse portion of the orbit. Presently the work in this area has been directed towards providing reliable technology for the development of integral heat pipe and thermal energy storage system [2].

Multicomponent eutectic fluorides were selected as energy storage materials in the 1000 K - 1400 K regime owing to their high heat of fusion per unit mass and melt volume [1]. Moreover, these salts were expected to be chemically stable and compatible with available commercial high temperature alloys. Three eutectic fluorides A: $\text{LiF} \cdot \text{MgF}_2 \cdot \text{KF}$, B: $\text{LiF} \cdot \text{MgF}_2 \cdot \text{NaF}$ and C: $\text{LiF} \cdot \text{MgF}_2$ having their transformation temperatures near 1000 K were selected as candidate energy storage salts for further research. A thermal energy storage capsule was then fabricated by sealing a measured amount of the salt in a metallic container. The selection of containment materials was a serious problem since it involved thermomechanical and thermochemical compatibility with the salts at the temperatures of interest for an expected lifetime of five to seven years [2,5]. In the event of any container corrosion, a loss of energy storage material by leakage could result or at worst the complete destruction of the thermal energy storage system due to increased mechanical stresses on the corroded container could occur.

Inconel 617 (I 617) (composition in wt % is : Cr 22, Mo 8, Co 13, Al 1, Ni 55 and rest Fe, C and Ti) was selected as a candidate material on the basis of thermodynamic calculations based on Gibbs free energy [6] since it was determined by simple oxidation-reduction reactions

that the fluorides of Li, Mg, Na and K under standard conditions were more stable than the fluorides of any of the alloying elements of I 617. Experiments were conducted under various conditions to obtain the corrosion compatibility of I 617. Steady state tests showed no significant degradation [6, 7], while a set of samples thermally cycled to simulate actual conditions failed due to defects and impurities in materials [8]. The present experiment was carried out at the Air Force Wright Aeronautical Laboratories, where certified I 617 thermal energy storage capsules were filled with ultrapure salt eutectics A, B and C under controlled conditions and then thermally cycled till failure occurred. Three of these samples were then removed after 10,000 hours and then transferred to Arizona State University for detailed post test evaluation of the corrosion degradation of the storage capsules. The analysis of these samples was carried out using several techniques. After initial Radiography to detect material flaws, microstructural analyses were performed with the Optical and Scanning Electron Microscopes to detect any changes in the microstructure. Microchemical analysis was then performed on the I 617 container with the Electron Probe Microanalyser to quantify any elemental depletion while the salts were analysed by Atomic Absorption Spectroscopy. Energy Dispersive X-ray and X-ray elemental mapping produced qualitative information about material inhomogeneity and elemental distribution. Semiquantitative estimates and probable mechanism for corrosion will result from these studies.

BACKGROUND AND LITERATURE REVIEW

Space stations and future space missions require a steady and reliable supply of heat for thermally driven refrigeration systems [2,5]. Solar dynamic space power systems are being proposed to provide the electric power needed in spacecraft refrigeration. A solar dynamic system comprises focussed mirrors to gather light, receivers to absorb energy, thermal energy storage and Rankine, Stirling or Brayton cycle heat engines for power generation [9]. Although there are other ways to store heat, thermal energy storage based on phase change is particularly attractive for turbine engines because it can provide a constant inlet temperature and minimizes the use of sensible heat which involves large structures and long heat flow paths [1,9].

Selection of phase change materials

Among the phase change processes, the solid to liquid transformation was more attractive than solid to solid or liquid to gas transformations [9]. This was because the solid to liquid phase change has higher energy density than the solid to solid transformations and does not require high strength containment vessel to accommodate the pressure build up as in the case of liquid to gas phase change. Thus the selection of energy storage materials suitable for the fusion phase change and with optimum properties becomes important. General criteria for the selection was that the storage material should possess a high heat of fusion per unit mass and melt volume since space applications demand restrictions on weight. Moreover, the transformation temperature should be near the temperature of interest and the material should have chemical stability and high thermal conductivity. The search for suitable energy storage materials in the 1000-1400 K regime was carried out by several researchers [1,6,10]. Feasibility study of metallic fluorides and inorganic salts was carried out by determination of their thermophysical properties and phase diagrams [6,11]. Pure fluoride salts were found to have the best combination of desirable properties such as high enthalpies of fusion and low mass per unit melt volume. However, the molten salts could be used only if the operating temperature of the heat engine was compatible with their melting points. This limitation was removed and greater flexibility in operating temperature was obtained by

considering congruently melting mixtures or multicomponent eutectics. Fluorides of Li, K, Mg, Na, Ca and other metals were considered as possible candidates. Due to the limited literature and availability of data on phase diagrams and properties of relevant fluorides, several experiments and approximations were made to obtain the heats of fusion and other pertinent data [11]. It was determined as a result that the fluorides of Li and Mg have the highest heats of fusion per unit mass and by the addition of Na or K, other eutectic compositions could be established in the 1000 K range being considered presently.

Selection of containment materials

The selection of an alloy for the fabrication of thermal energy storage capsules is very critical and is based on its mechanical and physical stability at high working temperatures and thermochemical compatibility with long term exposure. Initial research on fluoride corrosion of metals was conducted in nuclear applications where molten fluoride salt mixtures first became popular as carriers of fissile materials and as unfueled coolant salts in molten salt reactors [12]. Among other fluoride constituents, corrosion by LiF, NaF and KF salts were also studied with various materials of construction such as Inconel 600, stainless steels, nickel, monel and many other variations of nickel based alloys with varying amounts of chromium and iron. Experiments in static capsules as well as forced circulation loops were carried out around 1000 K. Most alloys exposed to molten salts showed void formation to various depths and depletion of chromium [12]. Analysis of attacked metal and salt clearly established that selective removal and outward diffusion of chromium resulted from oxidation by the fluoride mixtures. The observation of unconnected subsurface voids was explained as follows. Cr leached out from the surface of the metal causing an activity gradient which resulted in Cr atoms from the underlying region to diffuse out toward the surface, leaving behind a zone enriched with vacancies since the solute atoms of a given type diffuse faster than the other atoms of the crystalline lattice to fill the vacancies (Kirkendall effect). These vacancies agglomerated at grain boundaries or twins to form voids. As a result of the findings, a new alloy INOR-8 (now available as Hasteloy N) was developed at Oak Ridge national

laboratory on the following basis . Nickel, being most resistant to salt corrosion was considered the basic constituent, Mo was added for solid solution strengthening and Fe for flexibility in raw materials composition. The amount of Cr was reduced since it was least noble, but a minimum quantity was added for oxidation resistance. This alloy basically eliminated the problem of Cr depletion and void formation.

Alloy selection for Eutectic fluoride thermal energy storage materials was being attempted at Air Force Wright Aeronautical Laboratories by Davison [6]. Calculations of the free energy of simple oxidation-reduction reactions between elemental constituents of the alloy and each of the selected fluorides in their standard states were carried out for the temperature range 298-1500 K. The results showed that fluorides of Li, Na, K and Mg were more stable than the fluorides of any of the alloying constituents of I 617. Thus in a sealed, isothermal container the fluorides selected as thermal energy storage media were not expected to attack the metallic container.

Two sets of I 617 samples were tested to confirm the theoretical predictions of thermodynamic stability and post test evaluations were carried out by Beam [7]. One set was tested at a constant temperature in a vacuum furnace while the second set was electrically thermal cycled. Both showed no significant corrosion after an initial 2000 hrs and the isothermal sample showed no effect even after 10,000 hrs. Thermal cycle irreversible solubility effects were tested on a different batch of Samples fabricated with Inconel 600 (nominal wt % Fe 14, Cr 23, Al 1.2, and Ni 60.5) due to non availability of Inconel 617. Thermal cycling in a vacuum resulted in complete corrosive attack of the container after 200 hours of cyclic operation. Post test evaluations by Jacobson [8] showed that this corrosion could have occurred due to calcium impurities in metal and salt which may have acted as a solvent for nickel. Moreover, pinholes in the bar stock and the fabrication of the sample in an atmosphere of oxygen could have accelerated the damage. Microprobe analysis of the salt near the capsule walls showed that Fe, Cr, and Ni were leached into the salt. It was not clear if oxygen or nitrogen could have interacted in this corrosion or how this leaching may have occurred. Inconel 600, though inferior to I 617, has good high temperature oxidation resistance but it was not clear why it was unsatisfactory in this application. It was then

concluded that the corrosion and life capabilities of Inconel must be established conclusively and to that effect experiments with ultrapure salts and controlled fabrication procedures were devised to provide a clean environment.

In a program initiated at NASA Lewis research center, Misra [5,13] have conducted studies of salt - containment alloy combinations which have potential as thermal energy storage materials. Corrosion studies on a large number of Ni, Fe, Co based and other high temperature alloys were carried out by exposing these alloys to several fluoride eutectics. Only metallographic examination of the exposed metals was utilized to identify damage, since many of the salts cling tenaciously to the metal and prevent weight loss measurement [5]. Alloys were individually sealed with the salts in quartz capsules to prevent galvanic effects if more than one alloy were in contact. Spectrographic analysis showed that salts contained small amounts of Cr and Al but higher amounts of Mo and W. Though the majority of the alloys examined were Fe, Co, or Ni based, substantial amounts of these elements were not found. It was concluded [5] that NiF_2 may have formed a passivation layer and the presence of moisture may have increased corrosivity of MgF_2 melts by the formation of HF. Most high temperature alloys showed poor performance by uniform or grain boundary attack while mild steel, pure nickel and Nb-1Zr were resistant to fluorides. Nb-1Zr was hence the only suitable high temperature alloy but because of fabrication difficulty with such refractory alloys, there was much reluctance in using this as a candidate containment material. The poor showing by most common high temperature alloys was attributed to the fact that these materials were designed for use in an oxidizing environment where they would form Cr or Al rich protective scales but this defense mechanism may not be suitable for molten fluorides which can flux the oxides. It was possible that moisture or reactions with the crucible could bias the results and hence the only identifiable trend in this study was that Ni was quite stable to the attack of molten fluorides. Actual working conditions may not be as severe as this and one way of approaching the true conditions would need an all metal capsule as the specimen.

The present experiment being carried out at the AFWAL [2] employs an all metal specimen filled with fluoride eutectics which are vacuum thermally cycled and details of the experiment and analysis are presented in a later chapter.

THEORETICAL BACKGROUND

High temperature molten fluoride corrosion is a relatively unfamiliar and little studied system [12]. Several forms of attack such as elemental leaching, dissolution or chemical reaction are expected in a metal -molten salt system.

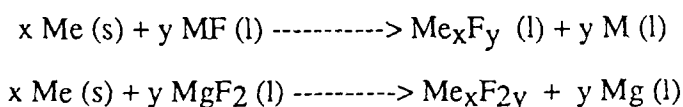
Corrosion in molten salts can be determined by either thermodynamics or kinetics or a combination of both [3]. The thermodynamic stability of a metal -molten salt system combination guarantees that kinetics are not important. This may be achieved in a few systems and molten fluorides offer the widest range of stability with largest number of metals i.e, there is no spontaneous reaction between the metal and the melt. Factors that control molten salt corrosion are the nobility of the metal, the stability of the pure melt and the redox potential of the melt [3]. The first two relate to the relative stability of the pure melt and the metal or alloy while the third includes the effect of dissolved impurities, such as water or oxygen. Such impurities would be cathodically active and could increase the anodic dissolution rate of the metal especially for systems in which the metal has no passivity as is usually the case with halides. Careful removal of impurities and equilibration of the molten salt with a very active metal had made it possible to reduce the corrosion of normal structural alloys to negligible values in many alkali halide melts. In general, molten halides require that stability of container material be maintained in a thermodynamic sense and this suggests that vigorous attention must be paid to maintain high purity systems.

The selective removal or leaching of an element from a solid alloy is a relatively unfamiliar form of corrosion . In aqueous systems where specific elements are removed from alloys, it was not clear whether the nobler element is oxidized and subsequently plated out or whether it agglomerates by a surface diffusion mechanism. Bulk diffusion was unlikely to play a major part and hence an alloy with the largest constituent behaves in a noble manner. In high temperature systems, leaching of the less noble component was probable even when present in low concentrations. The rate of leaching is probably related to the diffusivity in the solid of the constituent being removed. In general, during a process in which a fluoride is formed, the

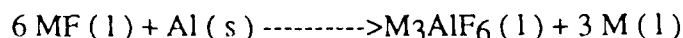
constituent that has a higher free energy of formation for the compound will react to the greatest extent. The other considerations are the diffusivity of the constituents and their activity coefficients in the alloy. From the free energy of formation of Ni, Cr and Fe fluorides, Cr was seen to have a more negative free energy of formation. As a result of several experiments Koger [12] proposed a corrosion mechanism by suggesting that fused salt and aqueous corrosion are similar in that both involve electrochemical factors, but in fused salts, solid state diffusion of alloy constituents become important unlike aqueous systems. Since protective films are unlikely, thermodynamic equilibrium of the reactions control the corrosion of the system and it may hence be necessary to maintain sufficiently reducing conditions in the melt to minimize leaching of the least noble alloying element.

Thermodynamic equilibrium calculations were carried out in detail by Misra et al [13] for reactions in a simple model of a system consisting of a pure salt sealed inside a metallic container. Since the initial atmosphere was inert, direct reaction if any, was expected between the alloy and the melt. Since the equilibrium state represents the maximum extent of corrosion [14] under a given set of conditions it is important in assessing the long term life of a containment vessel.

Possible corrosion reactions were defined as follows:



Where 'Me' is the metal Fe, Co, Cr or Ni and 'M' is Na, K or Li. The reaction with Al should yield AlF_3 but from the heat of mixing data it was inferred [13] that a complex M_3AlF_6 forms from the reaction of Al with the salts as



The equilibrium content of the compounds Me_xF_y and M_3AlF_6 in the melt determine the maximum extent of corrosion and hence the knowledge of these concentrations indicate the relative stability of each alloying element. Calculations based on an ideal solution for the melt and

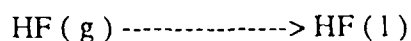
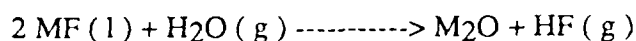
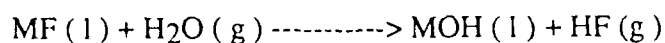
assumption of unit activity of the metal in the three systems LiF, NaF and KF show that the tendency to corrode increases in the order Ni, Co, Fe, Cr and Al. M_3AlF_6 concentration in the molten salts was so high that alloys containing significant amount of Al were expected to corrode severely. Even when these calculations were performed for Al at a reduced activity, for example in the gamma prime (γ') phase in superalloys, significant concentration of Al was still found in the salts indicating that corrosion was still important. Figure (1) shows the equilibrium concentrations of metals found in pure salts from calculations performed by Misra et al [13]. The equilibrium concentration of Ni, Co and Fe are much smaller than one mole parts per million (ppm) and are hence expected to be resistant to corrosive attack while Cr is likely to be corroded in NaF and KF melts because of higher solubility of CrF_2 in these melts. MgF_2 melts are much less reactive than the NaF and LiF melts. Calculations show that the concentration of CrF_2 and NiF_2 in MgF_2 melts are about three orders of magnitude less than in NaF or KF melts at 1100 K.

Non ideal solution behavior was assumed and these calculations were repeated. The non availability of data on activity coefficients for the $MF - Me_xF_y$ system resulted in the estimation from known phase diagrams [15]. A strong negative interaction seemed to exist from the very low values of the activity coefficients. On using these values to calculate concentrations of the Me_xF_y at 1100 K, and comparing them to the ideal solution case it was seen that there was an order of magnitude increase in the concentrations of the Me_xF_y salts in the LiF melt. Even then the Ni and Fe values were sufficiently low not to cause serious concern but Cr may become important at high temperatures. In NaF and KF melts, Cr concentration was quite high and can cause significant corrosion in Cr containing alloys. Hence, thermodynamic calculations indicated that Cr and Al were the most probable corroding elements and the effect of LiF was somewhat less than that of NaF or KF melts.

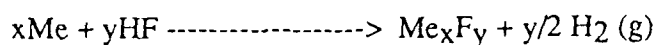
Refractory metals like Mo react with the melt and since only gaseous refractory fluorides exist in the 1000 -1400 K range, partial pressure of these gaseous fluorides are important in determining the extent of corrosion. The empty volume is then a parameter which affects the pressure but is usually quite small. The calculations for a system showed that about 10^{-7} mole of

metal would be reacted per mole of salt and it can hence be inferred that Mo is unlikely to corrode to any great extent in LiF, KF or NaF melts.

Water is very difficult to remove completely from the melt . Impurities or moisture alters the thermodynamic stability of the alloy - melt system since other deleterious reactions occur. Reactions such as



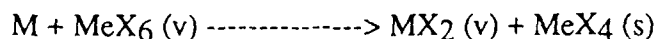
would cause the generation of HF and its subsequent reaction with the metal container causes severe corrosion problems. Furthermore the generation of H₂ by the reaction



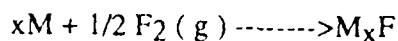
increases the pressure inside the container and may lead to mechanical failure of the containment vessel [16]. At 1100 K at an initial total pressure of 0.001 atmospheres the gas pressures generated inside the container are strongly dependent on the initial moisture content irrespective of the free volume.

Halogenation reactions

Studies carried out on the reactions between halogens and metals may be of interest in predicting the properties of halides that may form in a metal - molten salt system. Passivation of certain metals by halides or deposition of solid reduction products on metal surfaces could be of relevance in the stability of a corroding system [17]. A reaction like



where MeX₄ (s) blocks further rapid $M \longrightarrow MeX_6 (v)$ reaction. On the other hand such product compounds could accelerate reaction rates if volatile or liquid oxyhalides form and prevent passivation. For the formation of the lowest halide product M_xF in metal M,



and

$$\Delta G_{M_xF} = \Delta G^{\circ}_{M_xF} + RT \ln [a_{M_xF} / (a_M \cdot p^{1/2}_x)]$$

Where $\Delta G^{\circ}_{M_xF}$ is the standard Gibbs energy of formation for M_xF based on unit fugacity standard state for the F_2 gas and coexistence standard states for condensed phases, i.e. M saturated with respect to M_xF and MyX_F saturated with respect to M. If the metal and product phases are formed in the standard states (at unit activity), then critical F_2 pressure for the formation or existence of bulk halides is given by :

$$p^*(F_2) = \exp (2\Delta G^{\circ} (M_xF) / RT)$$

for the fluorides of Cr, Ni, Fe, et. which may form during reaction with molten fluoride salts. Though the pure form of these fluorides may have melting points higher than the operating temperature, the mixture of product compounds can establish a liquidus temperature far below those of the constituent compounds.

Halides exhibit predominant ionic conduction and even promote the phenomena of local action cells due to which metals can be consumed by halide scale formation. As an example, Ni, reacts with fluorine to form NiF_2 which adheres tenaciously to the metal substrate. It has a melting point of 1723 K and a low vapor pressure of 10^{-6} at 1073 K and hence passivates Ni and diffusion through scales is required for further fluoridation [17].

Studies carried out on internal fluoridation of a dilute Ni-Cr alloy exposed to high temperature showed CrF_3 precipitates at an advancing reaction front within the Ni matrix [18]. The advancement of this front was usually limited by diffusion of fluorine atoms through the zone of previous CrF_3 precipitation in the solid Ni. The presence of F and its solubility in Ni leads to this kind of internal precipitations as shown in Figure (2).

Vaporization

Experiments conducted on thermal energy storage capsules were done in vacuum in many instances to prevent oxidation of the alloy container which may lead to multiple facets to corrosion study. Vaporization is an important factor at the high temperatures of interest when exposed to vacuum. Metals may vaporize and diffusion of metallic components to the outside may ultimately lead to the formation of voids due to the 'Kirkendall' effect. When I 600 was heated in a 0.1 torr vacuum for 42 hours at 1648 K [19] Cr depletion and void formation at grain boundaries and twins was observed. Since the vapor pressures of various components are different, depletion of one component may occur in preference to another which may result in a loss of high temperature properties. The vaporization of a metal may be assumed to follow the Hertz-Langmuir equation given

$$G \text{ (g/cm}^2\text{sec)} = \sum p_i \text{ (atm)} / 2.26 \times 10^{-2} \text{ (M}_i / T)^{1/2}$$

where p_i is vapor pressure in atmospheres, M_i is molecular weight of vapor species and G is the weight of vapor species lost in vaporization. Vaporization rates were reported for Incoloy 800 by Jacobson [20] and was seen that Mn and Cr were more volatile than Ni and also that the vaporization rates for an element is different when pure and when present as an alloy constituent.

EXPERIMENTAL PROCEDURE AND ANALYSIS

Experimental Procedure

Inconel 617 was identified as a candidate material for comprehensive testing under conditions which are expected in a real situation. The present experiment was designed to overcome the drawbacks of the previous tests [6,7] and conclusively evaluate the corrosion compatibility of this alloy. The experiment was set up and conducted at the Wright Patterson Air Force Base, Ohio [2].

The procedure consisted of processing ultrapure samples of eutectic fluoride salt -clad metal thermal energy storage specimens under controlled conditions. This included mixing and melting of the salt under an inert gas atmosphere and welding of the specimen capsules by electron beam welding in contrast to previously used methods of air environment melting and end cap TIG welding [2]. Because of its severity, vacuum thermal cycling of the salt clad capsules between salt eutectic +100 K and eutectic -100 K was carried out for life with cumulative cycle and test hours accumulation in order to obtain valuable data on the compatibility and corrosion.

The salt candidates selected for consideration were

Eutectic A	LiF.MgF ₂ .KF
Eutectic B	LiF.MgF ₂ .NaF
Eutectic C	LiF.MgF ₂

with a container material of Inconel 617. Tables (1,2) give the compositions of the salt and container respectively.

The salt samples were prepared by in-situ casting where the salt was placed and melted in the containers in which they would be life tested. This method faced two minor problems of exposing the salt to ambient atmosphere during loading of the capsules into the melting chamber and also during the cleaning of the end cap mating area before electron beam welding. However, no ill effects were believed to have occurred on the overall testing program. Ultrapure fluoride salts LiF, MgF₂, NaF and KF were obtained in plastic bottles, tightly packed under an

argon/nitrogen atmosphere. These were then measured and mixed inside a glove box maintained inert at contamination levels of oxygen and moisture below 3 ppm and 0.2 ppm respectively. The container was 3 inch long and 1 inch in diameter and fabricated from extruded Inconel 617 tube and bar stock as shown in Figure (3,4). Only 45 grams of the eutectic was loaded into each capsule to allow for liquid expansion. Seventeen capsules were processed and filled with the eutectics A, B or C, electron beam welded and then tested by vacuum thermal cycling [2].

The conduction of this test in a vacuum furnace eliminated external corrosion of the capsules and provided for the safety of the personnel in the event of a leak or capsule breach. The seventeen capsules were arranged in three groups, stacked in mounting brackets symmetrically around the tube axis. A roughing pump maintained 60 millitorr vacuum and the power supply to the furnace was controlled through a set point programmer and timer to control the thermal cycle requirement. The cycling was continued at a rate of 4 hours per cycle, 6 cycles per day and 2190 cycles in a year. The plan was for continuous thermal cycling until failure occurred in any of the capsules with subsequent analysis. If none fail, the test will be discontinued after 21,900 hours or five years of life. Three samples, designated #14, #17, and #20 and filled with eutectics B, C and A respectively were removed after 10,000 hours of testing and were sent to Arizona State University for detailed post test analysis which is reported below.

Analysis

The analysis involved the following procedures:

Radiography

Optical and Scanning electron microscopy

Electron microprobe and X-ray analysis

Bulk chemical analysis

Radiography

X-ray radiography was carried out on the samples prior to cutting them. The purpose of the radiographs was to reveal internal flaws or weld defects so that regions of interest could be

identified for further detailed observation. Side and top view X-ray radiographs were obtained using 250 kv to 350 kv . The radiograph in Figure (5) shows the solidification profile as well as the wall and end cap. The brighter regions are solid and the darker are hollow or of lower material density. Within the capability of the instrument resolution, no flaws were observed in the two directions of projection.

Metallography

The specimens were cut into sections for metallographic examination which were selected on the basis of evaluation of important regions. The initial cutting was done by hacksaw to avoid contaminating the salt by coolants and cutting oils. Samples of the salt from the interior or regions away from the cut were used for chemical analysis. The metallic samples used in microscopy were then cut with a diamond saw to avoid mechanical damage. The schematic of the sections of the energy storage capsules used in metallography are presented in Figure (6). Visual examination of the salts did not reveal any significant discoloration.

The specimens were prepared by further cutting the above sections followed by hot pressure mounting them with bakelite or lucite . Some of the samples used for Scanning electron microscopy were mounted with conductive graphite to avoid 'charging' by the electron beam. Standard procedure for sample preparation included sanding with 180, 240, 320, 400, 600 silicon carbide grit followed by polishing with 6 micron diamond paste, 1 micron and .05 micron alumina successively. There was some difficulty in obtaining scratch free samples since mechanical removal of some of the hard inclusions like TiN resulted in unavoidable damage during polishing. Samples were then thoroughly cleaned with water and ethanol and etched for further observation. Several etching solutions were tried to obtain a clean microstructure but the most consistent was 'aqua regia' (3 HCl : 1 HNO₃ by volume) and 'glyceragia', (3 HCl : 3 Glycerol : 1 HNO₃ by volume).

Optical Microscopy

The general microstructure of the samples (# 14,17 or 20) consisted of well defined and large grains of unequal size with the grain boundaries decorated with irregular carbide precipitates. Some of these were blocky while others were elongated in the direction of the grain boundaries. These carbides are most probably Cr or Mo based. The bulk grains contained some chunky precipitates and orange cuboidal inclusions which were likely carbides and titanium nitrides respectively and are shown in Figure (7).

A new tube of I 617 was cut and the samples prepared in a similar manner to that of the tested ones in order to compare the microstructure of the tested samples with an untested I 617 specimen. This untested sample was not fabricated from the same stock as the thermal energy storage capsules nor was it's exact heat treatment history known, but a safe assumption would be that these were procured in the annealed condition. It was observed that the microstructural phases visible were substantially the same as for the tested samples except that the distribution was different as observed in Figure (8). The grain boundaries in the untested sample became visible only after a longer etch and the boundaries were not seen to be decorated with precipitates as in the case of the tested samples. This could have been due to the long heating (10,000 hours at 1000 K , which is in the sensitization range) of the tested samples and may have caused the precipitation of carbides on grain boundaries [12].

Microstructural changes on the inner edge (exposed to the molten salts), outer edge (exposed to vacuum) and across the thickness of the wall was studied at various magnifications. At magnifications of 50 X and 100 X, the inner edge showed some roughness but little observable damage as seen in Figures (9,10). The dark spotty features are seen at higher magnifications to be the precipitates of titanium. At higher magnifications the pits are seen close to the inner edge, some of which are irregular while others conform to the shape of the precipitates. These pits could have formed due to the removal of these inclusions during mechanical polishing or due to reactions with the salt. At the very edge of the tube wall the precipitates may have dissolved or reacted with the salts.

The outer edge of the sample which was constantly in 0.06 torr vacuum, showed some surprising damage. Though it was initially thought to be a specimen preparation artefact, careful cutting and polishing did not eliminate the feature and was consistently observed in all the samples as seen in Figures (11,12) . Some of the voids and precipitates, occurred along grain boundaries and were elongated similar to the sigma precipitates [21]. These could be due to preparation, internal reaction due to residual oxygen in the vacuum or some diffusional effect caused by vaporization at the high operating temperatures.

The thermal energy storage capsule was fabricated by electron beam welding a tube of 1 inch diameter and 3 inches long, at both its ends with caps. As seen in Figure (13), in the region close to the weld here is a gap between the end cap and the tube wall possibly due to design or insufficient weld depth. The microstructure of the cross section near the gap is not very different from the other regions but the grains appear to be slightly smaller than the tube wall further away as in Figures (14,15) . Even at higher magnifications as shown in Figures (16,17), damage is barely visible at the edges. From Figures (18,19) it is seen that the gap between the end cap and the tube wall extends perpendicular to the tube wall discontinuous in some cases but extending in some to almost half the thickness of the tube wall. Some of the grains near the gap are irregular and appear to be deformed, as seen in Figure (21) possibly due to the heat effects during welding. These gaps may turn out to be the weakest point in the capsule and prone to failure due to internal pressure buildup or some form of localized corrosion caused by the presence of the gap.

Scanning Electron Microscopy

The Scanning Electron Microscope offers good resolution and depth of field at much higher magnification than the optical microscope. Two types of imaging signals have been utilized to study the microstructure of the samples. In the secondary electron imaging mode (SEI), topographic features of the sample were imaged to study the shape, morphology and microscopic physical damage to the grain and precipitates that may have occurred due to corrosion. In the backscattered electron mode (BSE), atomic number dependence or compositional contrast was

obtained with the help of which compositional inhomogenities were detected qualitatively. An advantage of this technique was that precipitates and inclusions were approximately identified by their relative brightness in the pictures since phases with a higher average atomic number show up brighter than those with a lower mean atomic number. The phases in the microstructure were also qualitatively identified by recording Energy Dispersive X-ray spectra (EDS) from the area of interest.

The general microstructure of the tested samples is shown in Figures (21,22). The samples were deeply etched in aqua regia to reveal the grain boundaries and it was observed that the irregular and blocky precipitates were arranged along the grain boundaries discontinuously. There were other similar precipitates along with the cuboidal inclusions which were randomly distributed. From the BSE image and EDS spectra shown in Figures (23,24,25), it can be inferred that most of the precipitates lining the grain boundaries were either Cr or Mo rich where the brighter ones were Mo rich. These are known from literature [21,22] to be either M_6C or $M_{23}C_6$ carbides where M refers to Cr or Mo. The cuboidal precipitates appeared darker than the rest and were seen to be Ti rich, most probably titanium nitride. The EDS and microstructure of the untested I 617 shown in Figures (26,27) is comparable to the tested ones but these precipitates were seen to have a more random distribution than the tested ones and the deep etch showed the grain boundary better but no precipitates decorating it. It was seen that none of the precipitates in the BSE image were comparable to the bright Mo rich phases visible in the tested samples. It may be likely that Mo did not precipitate in this case, since it was not exposed to the high temperatures for the time that the other tested samples were exposed to.

Inner Edge Profile

The region near the edge of the wall which was in contact with the salt was examined for microscopic indications of corrosion. At a magnification of about 1400 X as shown in Figure (28), the voids could be due to reaction or mechanical polishing as stated earlier since some of the pits have a similar profile to that of the titanium nitrides. Some of these pits close to the edge might

have been caused by dissolution or reaction with the salt. Voids due to diffusional effects were also likely, but since these were present non uniformly along the edges, it may be improbable. The damage extends to about 10 microns and it was seen that precipitates and grain boundaries were not quite visible near the very edge. This may be because of corrosion effect on the grain boundary precipitates near the edges or an effect of uneven etching resulting from rounding of the sample edge. The grain boundaries slightly away from the edge were visible as seen in Figure (29) but no significant damage was seen to have occurred.

Outer Edge Profile

As in the optical micrographs about 10 - 30 micron damage was seen to occur near the outer edge as shown in Figures (30,31). This damage was seen to be of the form of irregular or enlarged precipitates or voids. These could be the result of removal of precipitates during polishing or due to high temperature exposure to the vacuum. The feature uniformity indicates that it was possibly due to some reaction with residual gases or voids formed by diffusional effect and vaporization.

Salt Solidification Structure

The eutectic solidification structure of A and B taken in the BSE mode shows bright and dark regions which were identified qualitatively by the EDS spectrum as seen in Figure (32). The brighter region due to a higher atomic number was obviously the Na, K or Mg rich phase while the dark regions were F and Li rich. Li cannot be identified by X-ray analysis because of its low atomic number which prevents the excitation of X-ray.

X-Ray Mapping

Energy Dispersive X-ray Spectra (EDS) analysis was used to distinguish elements by obtaining a spectrum of their characteristic energies. By selecting certain energy windows so as to collect the X-ray signal corresponding to a particular element, an elemental distribution map can be obtained. This was done with the amplified signal of the selected energy from the detector system

to modulate the brightness of a CRT scanned in synchronism with the electron probe. The X-ray map of the element shows the regions rich in that element to be bright in a dark background. X-ray maps were taken to detect any inhomogenities or depletion that may have resulted due to the corrosion processes. Figures (33,34) show the details of the region on a composite video image on the left and X-ray map on the right of the micrograph. Images of the general microstructure near the inner edge and end cap are shown in Figures(35,36). The maps do not clearly show significant change in the edge composition probably because of the limited resolution of the X-rays which are generated from a larger interaction volume as compared to the SE images. Since alumina polishing was used in the preparation of the sample some errors were incurred due to accumulation of particles inspite of ultrasonic cleaning evidenced by the bright region just near the edge in the gap between the mounting material and the sample as seen in Fig (37).

Electron Probe Microanalysis

The electron probe microanalyser (EPMA) consists basically of an electron source and detection systems for X-rays. It is in fact a modification of a SEM with additional spectrometers to speed the analysis of many elements simultaneously. The JEOL EPMA consists of four crystal spectrometers using the Wavelength Dispersive (WDS) technique for quantitative analysis. Standards are used and the ZAF corrections are made using the 'Task' program in the 'Tracor Northern' software. Weight percent compositions were obtained for metallic and salt specimens for up to 12 elements simultaneously with a 2 micron beam diameter and 10 nA beam current. During analysis it was important to focus the beam in the area of interest which had to be necessarily flat if accurate quantitative information was to be obtained. Representative data are presented for the alloy in Table (3).

The concentration variations across the wall thickness were measured to determine if any elemental depletion had occurred. This was carried out by measuring the composition of the bulk grain at 10 micron intervals. Errors were likely to occur if the beam was impinged on regions close to the edge since edge rounding causes a loss of signals. An optical microscope was

attached, the focussing of which insured that the area of interest was flat enough for the spectrometers to obtain a reliable reading. Sample spots very near precipitates or voids were avoided to prevent signals of those features from interfering with the bulk analysis.

It was observed from the values obtained in these profile analyses that there was a significant relative reduction in the quantities of Al and somewhat smaller change in that of Cr in regions near the inner and outer edges of the tube wall. Other elements did not seem to be affected in any remarkable manner. The normalized changes in the concentration of the various alloying constituents of samples #14, 17 and 20 are shown in Figure (38,39). The points selected for probing were selected so as to avoid non planar points and features smaller than about 2 microns since the analysis would then be inaccurate. The small probe size may cause the scatter in the data points obtained.

The salt was analysed to detect the presence of any alloying constituent that may have leached out or dissolved. Except for some Al detected occasionally, no consistent quantities of any other element were detected. The difficulty in the use of the microprobe was that the elements which were probably in the salt may have been present in a particular phase of the eutectic structure and it becomes difficult to detect these, if not known apriori. Hence, additional chemical analyses were conducted for the detection of Al and Cr in the salts by alternative techniques such as Atomic Absorption Spectroscopy (AAS).

Chemical Analysis

The average analysis of the presence of any metallic element in the salt was not possible with the EPMA and hence wet analysis was resorted to. The quantitative analysis for Al and Cr were performed by Laboratory Consultants Ltd. by flame Atomic absorption spectroscopy using standards. The salt samples were dissolved in concentrated nitric acid and digested for several hours after which the solution was subjected to flame spectroscopy. The results are presented in Table (4).

DISCUSSION

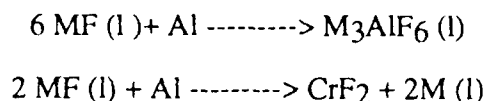
The results of the detailed analysis by the various techniques indicates that the corrosion effects have not yet become severe. Though no gross metallographic damage was observed, data from the EPMA and chemical analysis shows the possibility of some elements being removed from the metallic alloy and displaced into the salt resulting in the degradation of the container material. Moreover, comparison of the observed values with some thermodynamic calculations indicates an interesting trend in the variation which could probably aid in the prediction of lifetime.

Depletion of Al near the inner edge

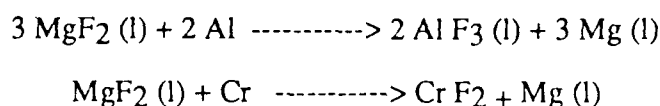
The purpose of the present experiment was to determine the effect of long term exposure of the metal to the salt. Quantitative microprobe measurements made across the wall of the container tube indicate a decrease in Al and to a lesser extent Cr near the inner edge in contact with the salt. Though the numerous data indicate a consistent trend, several sources of error should be kept in mind when interpreting this data. First, the probe size was approximately 2 microns and any inhomogeneity of this order would lead to differences in measurements from similar or closely located points. As stated in the previous chapter, readings taken very near the edge or on uneven regions are likely to be erroneous due to loss of signals. Moreover measurement of distance from the edge was carried out by visual observation through graduations in the optical microscope and the resulting errors prevented any rigorous quantitative treatment. With due consideration of the possible errors it can still be stated that a normalized change in concentration shows a depletion in Al and to a much smaller extent in Cr, while the other alloy constituents are virtually constant. The results of the chemical analysis by atomic absorption spectroscopy indicates a small amount of Al and traces of Cr in the salt.

The removal of Al and Cr from the salt can be considered in light of thermodynamic calculations performed by Misra et al [13], where they used in their model one mole each of pure salt LiF, KF, NaF and MgF_2 reacting with pure metals assuming both ideal and non ideal behaviour. Their results indicate that the equilibrium amounts of the Al salt were the highest,

followed by Cr among the group of elements constituting alloy I 617. Simple dissolution of the pure metal in the salt is uncommon except in their own salts and hence it is more probable that these elements leached out by direct reaction with the salt. Assuming individual reactions such as



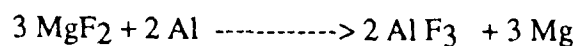
Where M is Li, K or Na and



for the sake of thermodynamic calculations.

In the present experiment the reaction was between the metals and eutectics of several combinations among these salts. Solution of the exact equilibrium amounts under actual conditions involves tedious and complicated numerical calculation. This effort would still not yield exact values because of the non availability of activity coefficient data for the various systems at the temperatures of interest resulting in the use of estimated values. Hence in the present case, a simplified approach was taken to evaluate an approximate amount of metal fluoride that could be expected at equilibrium.

The temperature was taken to be 1100 K, the upper limit of thermal cycling in this experiment, since more data were reported at this temperature. In the case of Al, the salt expected was the complex fluoride M_3AlF_6 in the case where M is Li, Na or K while it is probably AlF_3 in the case of reaction with MgF_2 since no complex fluoride is reported. In the calculation by Misra et al [13], 0.1 mole of M_3AlF_6 forms with every mole of NaF or KF while 0.001 mole of the salt forms with LiF. Calculation for MgF_2 is not reported but by a similar approach it is determined using the relations and from available data [23] as follows:



$$a(\text{MgF}_2) = a_{\text{Al}} = 1$$

$$\Delta G^{\circ}_f = -RT \ln a^3(\text{Mg}) \cdot a^3(\text{AlF}_3)$$

$$\exp(-\Delta G^{\circ}_f / RT) = a^3(\text{Mg}) \cdot a^3(\text{AlF}_3)$$

When ideal behaviour was considered the concentration of AlF_3 was about 1.9×10^{-4} moles. The number of moles of each salt in each eutectic A, B and C was calculated from their weight fraction and by simple proportion the corresponding weight of the Al salt expected in each eutectic was calculated. In A, for example, 0.73 moles of LiF , 0.35 moles of MgF_2 and 0.07 moles of KF were present from which the amounts of Al salt were found to be 7.3×10^{-4} , 6.5×10^{-5} and 7.0×10^{-3} moles respectively. The total weight percent expected was then calculated from the initial weight of the eutectic added i.e, 45 grams and determined to be 0.47% in A, 0.89% in B and 0.05% in C. The values of weight percent of Al determined from AAS measurements showed 0.31% in A, 0.25% in B and .29% in C. The similarity in the experimentally determined amounts in A, B and C and the wide range of values in the calculated amounts could be the possible effect of excluding the non ideal behaviour in the Mg salt or some incorrectly assumed reactions. Moreover, it was not possible for the experimentally determined amounts to be larger than the equilibrium values which set the limit for the extent of reaction under constant conditions in a closed system.

In certain other calculations [13] it was seen that the introduction of non ideal behaviour of solutions increased the molar quantities of the metallic salt by an order of magnitude. The results of chemical analysis showed that the three eutectics had almost the same amounts of Al and since among the constituents of the eutectics, MgF_2 is the one which is almost constant in A, B and C it was more likely that a calculation with MgF_2 needed correction. Though it was known that the complex fluorides formed from Li, Na and K were closely ideal solutions, not much was reported about Mg fluorides such as the $\text{MgF}_2 - \text{AlF}_3$ system. Hence as in some other cases [13], an

activity coefficient of 0.001 was assumed for AlF_3 and 0.01 for Mg. The results of such calculations resulted in the equilibrium values as A : 0.93%, B: 1.33%, C: 0.55% .

If the approximations and assumptions are valid to a reasonable degree, it can be concluded that though the reaction has probably started, equilibrium amounts have not yet been achieved. Hence, if the conditions do not alter drastically, the Al reaction should occur till thermodynamic equilibrium is reached after which corrosion is not theoretically expected. By this time, depending on the kinetics, either equilibrium is achieved and the alloy becomes weak to the point of failure or it may not reach equilibrium in the life time of the TES device reducing depletion and hence preventing failure.

Diffusion relations

The graphs plotted for the concentration profile of Al across the tube wall near the inner edge as shown in Figures (40,41) resembled very closely the solid state diffusion curve of a binary system in a one dimensional, semi infinite bar. To test for any similarity, a diffusion model was established with two independent variable parameters, the diffusion coefficient and the boundary condition. The model assumed that the concentration profile observed was a result of the concentration gradient caused by the reaction of the Al at the inner edge with the salt which resulted in the depletion of Al from the edge and forced the Al to diffuse from the bulk towards the edge at the high temperatures of interest.

The diffusion relation and model was based on the assumption of a one-dimensional cartesian coordinate system where the salt clad interface was at a low concentration of Al and the bulk which was taken as extending to infinity was considered as having the constant composition of the original alloy. The validity of this equation was based on the fact that the diffusion length was much smaller than the wall thickness [24]. A slight modification of the error function relation to suit the boundary condition resulted in curves which were matched with those determined experimentally. The expression is as follows:

$$C_x = C_0 + (C_s - C_0) \operatorname{erf} (x / 2 (D \cdot t)^{1/2})$$

C_s = bulk concentration of the alloy

C_o = Al concentration of alloy at salt clad interface

C_x = Al concentration at any point x along the tube wall from the inner edge.

D = diffusion coefficient of Al in alloy

t = time of testing (10,000 hours)

The parameters which were varied to get the curves of x versus C_x were C_o and D . This was because the value C_o could not be determined from the microprobe since the beam cannot be pointed at the very edge of the tube wall. The curves were plotted for various values of C_o approximated from the analysis of the salts and several D values from available literature on similar alloys as presented in Figure (42). The closest fitting curve was determined from a least squares algorithm was considered to be the most probable diffusion curve under the existing conditions. This resulted in a $D = 1.0 \times 10^{-13} \text{ cm}^2 / \text{sec}$ and the $C_o = 0.38 \%$ by weight of Al. The algorithm used in the determination of the best fitting parameters was an IMSL routine 'ZXSSQ' which is a finite difference method for solving the least squares of M nonlinear functions of a parameter X (X_1, X_2, \dots, X_n) of N parameters to be estimated. In the present case the X 's were D and C_o and the function was the diffusion equation stated above. This procedure was sensitive to the assigned initial values and determined the local minimum least squares. The calculated values were then plotted along with the average values obtained from experiment as shown in Figure (43)

There were no reported values of D for Al in I 617 in literature but the data for Ni - Al and Ni - Cr - Al alloys indicated that the order of magnitude determined was quite close to the values of D available from literature [25]. The concentration at the very edge, which had been determined from the calculations in this model was 0.38 % which shows that a reduction from an original 1.3 % has occurred from the salt clad interface leading to a likely weakening of the material. The close matching of the experimental and calculated curves lends further credence to the possibility of the diffusion control in the corrosion reaction causing a reduced corrosion rate. An alloy with a low

diffusivity of Al would then be advantageous and can be used to design TES capsules with reduced wall thicknesses. With further exposure, the salt - metal reaction and the diffusion of Al through the wall will be competing processes till the thermodynamic equilibrium is reached. Once the supply of Al by diffusion leads to its equilibrium, the concentration gradient would vanish but result in a lower average concentration of Al. If this concentration is not high enough to maintain the required strength in the alloy then the mechanical integrity will be under suspicion. It is interesting to note that the time required for Al to diffuse across the wall under these conditions could be many times longer than the time span for which the TES capsules are intended for and would hence not be relevant to the life time of the device.

Cr depletion from the inner edge

Cr is the only other alloying element of I 617 which showed a very slight reduction in the EPMA across the wall. The results of the AAS analysis on the salt for Cr indicated traces of Cr of the order of $10^{-4}\%$ by weight of the salt. It can hence be stated that Cr corrosion was minimal. Thermodynamic calculations conducted in a similar fashion for the salts indicate that at equilibrium A, B and C were expected to have 1.6×10^{-3} , 3×10^{-3} and $4 \times 10^{-4} \%$ respectively. Hence the equilibrium values have either not reached or are approaching but it is not of serious concern because a minor depletion of Cr is not expected to cause a severe degradation in properties. If some changes in the activities do cause increased corrosion it can still be confidently stated that the diffusion of Cr through the matrix, which is slower than Al by almost an order of magnitude would certainly prevent rapid corrosion.

Damage on the outer edge

The outer edge of the wall was in constant exposure to a vacuum of about 0.06 torr at high temperature and showed some microstructural damage consisting of voids and some elongated and irregular inclusions. The EPMA conducted on those regions showed a strong depletion of both Al and Cr from the alloy. Difficulty in probing near these voids and inclusions prevented a profile analysis but the data obtained near this edge at various points indicated a sharp drop in Al as seen

in Figure (45) and Cr to a lesser extent. Representative data for a set of points are presented in Table (5). The thin coating on the outer surface was probably an oxide formed during fabrication or from residual oxygen in the vacuum furnace. The possible explanation for this damage can be attempted by considering the effect of exposure of alloys at high temperature to vacuum [12,19]. The most probable reason could be the vaporization of elements from the I 617 matrix. When vapor pressure calculations were made to predict the vaporization tendencies, it was observed that the vapor pressures of gaseous elements at 1100 K increase in the order as Mo, Co, Ni, Cr and Al. Assuming that the vaporization rates are proportional to their vapor pressures, it was not difficult to realize why Al and Cr are depleted and since Ni, the base metal is also simultaneously vaporizing, Mo and Co were expected to register an increase in normalised composition which was observed in several data points. There were no clear indicators to the identity of the elongated precipitates found near the outer edge but the shape of some of these are characteristic of sigma precipitates. Internal oxidation or fluoridation are other possibilities which result in very similar looking inclusions [18].

Microstructural effects

Changes in the microstructure of the samples were not very significant. The major difference in the tested and untested I 617 was the absence of the Mo rich precipitates in the untested samples which suggests that (Mo, Cr) carbides were probably favored at long exposure to high temperatures, especially near the sensitization range. The tiny pits at the edge could not be positively identified as due to sample preparation or corrosion and hence further exposure was needed to confirm the cause. One possibility was that the pits near the edge may be Kirkendall voids caused by diffusion of Al which could have traversed a small distance only due to the short time of exposure compared to the diffusion length of Al through the I 617. The movement of these pits away from the edge in the course of time will confirm the diffusion hypothesis. The region between the end cap and tube are a source of worry since the expansion of the salt during melting may cause these gaps to enlarge resulting in a catastrophic failure during service. It is hence

essential to either change the design of the end cap area or increase the welding penetration to prevent any gaps and thereby remove this weak point.

CONCLUSIONS

The results of the detailed metallographic and analytical study indicates a certain trend of events and gives an insight into the direction of further work needed to accomplish the objective of choosing an acceptable containment material for the energy storage applications.

The present samples removed after 10,000 hours of testing seem to be in reasonably good condition as far as the microstructure is concerned. The exposure to thermal cycles in a vacuum is a severe test and its success so far is encouraging. The chemical analyses which indicated Al removal may not turn out to be very serious. As seen from calculations, the effect of reaching thermodynamic equilibrium would prevent further reaction; better still, the diffusion control over the rate of depletion may cause sufficient delay in reactions so as to exceed the projected life time of such a device. One way of reducing the risk is to equilibrate the salt with a precalculated amount of Al and Cr during sealing of the salt. This requires exact thermodynamic calculations for which critical data on activity coefficients and phase diagrams of the various molten salt systems are needed. Precise knowledge would then aid in risk free selection of TES tubes with lower wall thicknesses which is a great advantage in space applications. One method of obtaining useful information about the kinetics and mechanisms of reactions, and activity coefficient data is a versatile electrochemical cell detailed in Appendix A. Polarisation curves and other potentiometric measurements would allow generation of data which could be used in designing the ultimate failure proof and economical container for thermal energy storage.

APPENDIX A

Electrochemical Methods

Corrosion phenomena are basically electrochemical in nature and hence electrochemical techniques can be used to determine corrosion rates, mechanisms and other useful data. Corrosivity of molten salts generally increases with time since they become oxidized and contaminated with metal impurities [1]. Fortunately, metals seem to be appreciably soluble only in their own salts and corrosion by dissolution is hence not very important. The corrosion of metals and alloys in molten salts is determined by the redox potential of the galvanic cell. The potential is related to the activities of the metallic ions and those of the reducing species present in solution in the melt. Accelerated corrosion studies using electrochemical I - V curves have been used to estimate the corrosion characteristics of the environment on metals and alloys.

The polarization in the electrodes affects the corrosion rate; this polarization rate depends on the nature of the material, properties of the medium and the impurities in the medium. The equilibrium corroding current I_{corr} and V_{corr} are measured experimentally and converted to corrosion rates. The I_{corr} and V_{corr} are measured indirectly by accentuating the anodic and cathodic processes on the alloy specimen with the help of an inert counter electrode and a reversible reference electrode. I - V measurements have been made for I 600 in a NaCl - NaNO₃ - Na₂SO₄ eutectic have been reported [26]. Several other studies of corrosion in molten salts have been done by potentiostatic polarization curves [2]. The Tafel extrapolation method is difficult to use because of the limited Tafel region in molten salts. Nishikata used the polarization resistance technique and concluded that the correlation between the polarization resistance and the corrosion current obeyed the Stern - Geary equation. Molten fluoride corrosion tests in the 1000 K regime have not been reported. With the setting up of an electrochemical high temperature cell, data about corrosion rates, effects of impurities in changing the kinetics, details of corrosion mechanisms and with some slight modifications much needed activity coefficient data can be obtained.

The setting up of such a cell involves selection of materials for high temperature applications which do not react with fluorides, eg. Boron nitride [3]. Studies to establish reference electrode, fabrication of reference electrode and finally enclosing them under ultra high purity to vacuum or inert atmosphere is quite difficult. The preliminary cell as shown in Figure (A1) is

designed to help establish working parameters for a versatile cell [4]. This incorporates a Boron nitride cell ($< 5\% \text{ B}_2\text{O}_3$) which is probably the best material available for withstanding high temperature and with good corrosion resistance and inert environment. The electrode system is designed to allow different alloys to be easily attached for experiments.

a. Electrochemical cell electrode.

b. Electrochemical cell setup.

Figure A1. High temperature Electrochemical cell design for Fluoride experiments.

APPENDIX B

Micrographs and Figures

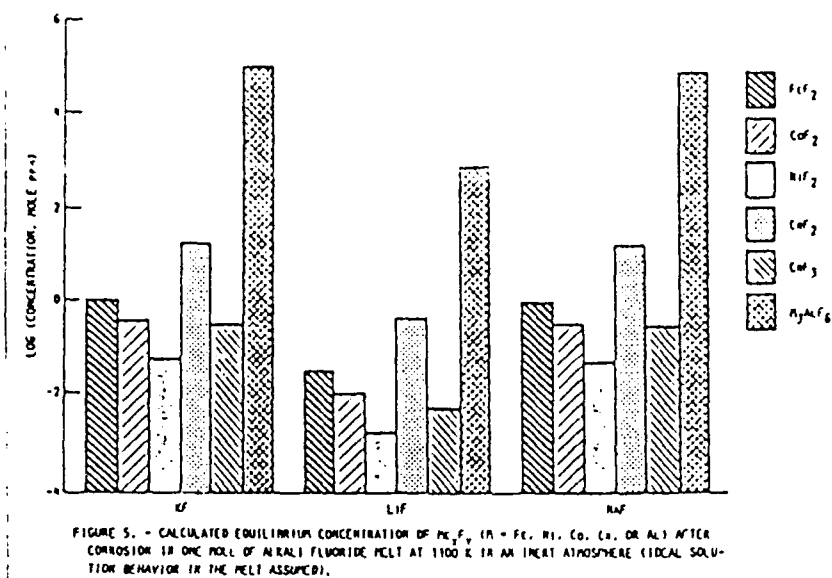


Figure 1. Graph showing calculated equilibrium amounts of metal in salts [13].

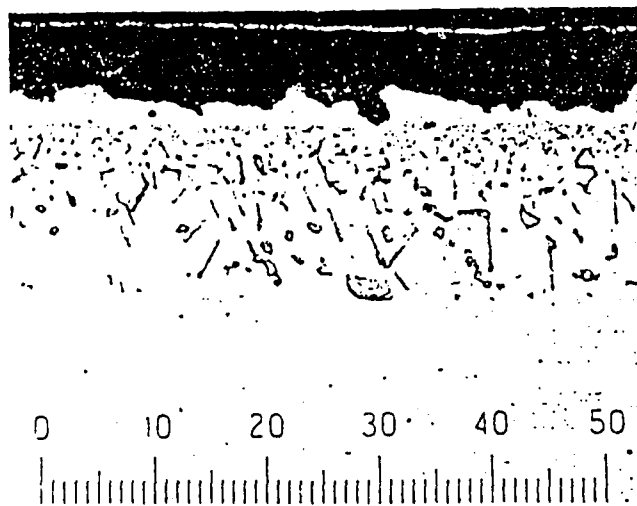
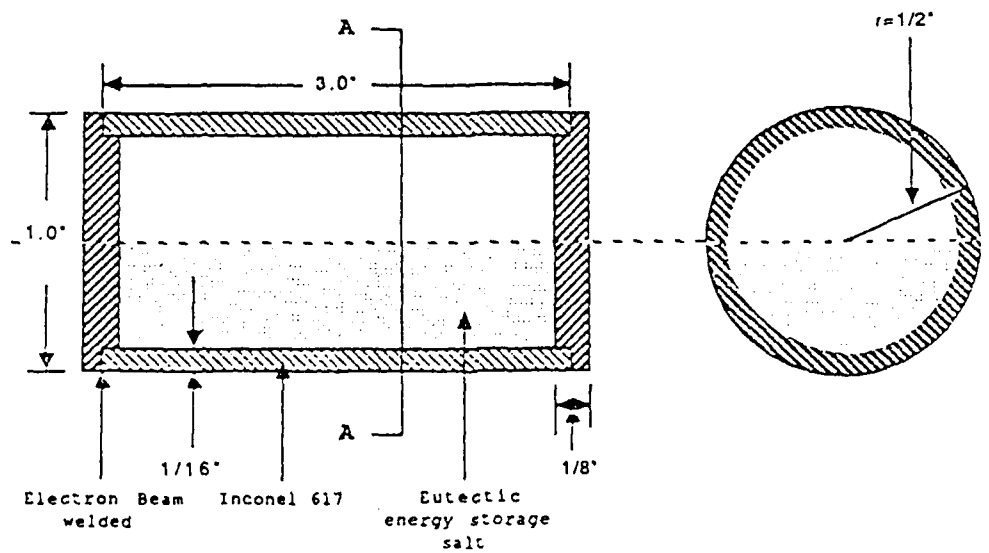


Figure 2. Internal fluoridation in a Ni - Cr alloy with F atmosphere[18].



a. Photograph of a Thermal Energy storage capsule.



b. Section drawing of a TES capsule

Figure 3. Thermal Energy Storage (TES) capsule.



a. Longitudinal section of TES capsule.

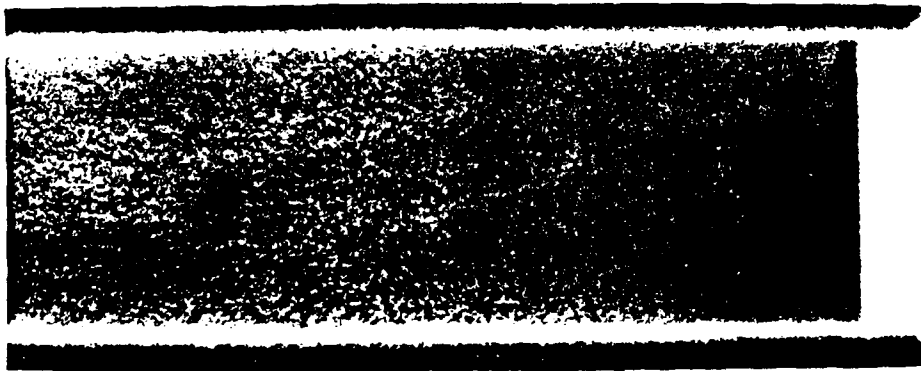


b. Transverse section of TES capsule.

Figure 4. Cut section photographs showing salt solidification profile.

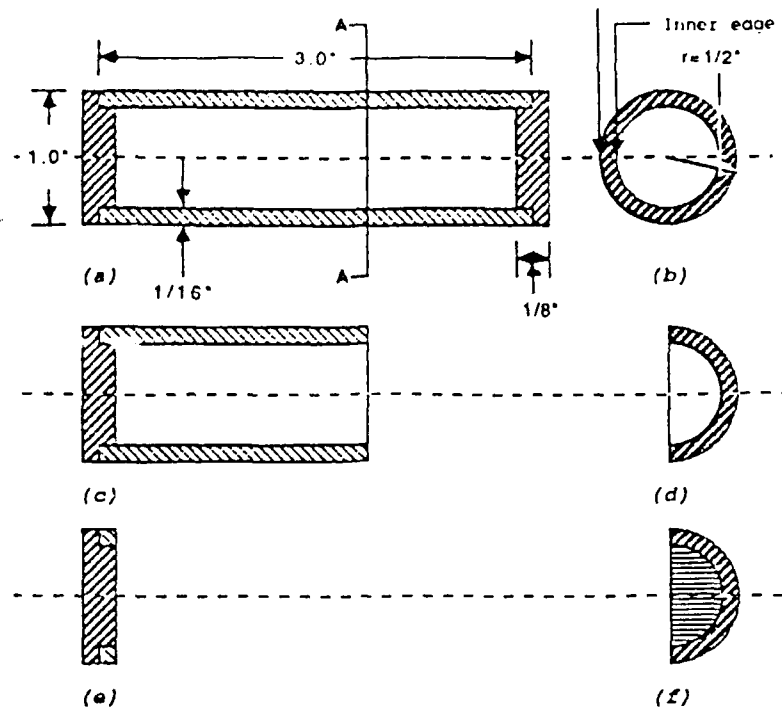


a. Radiograph of a TES capsule.

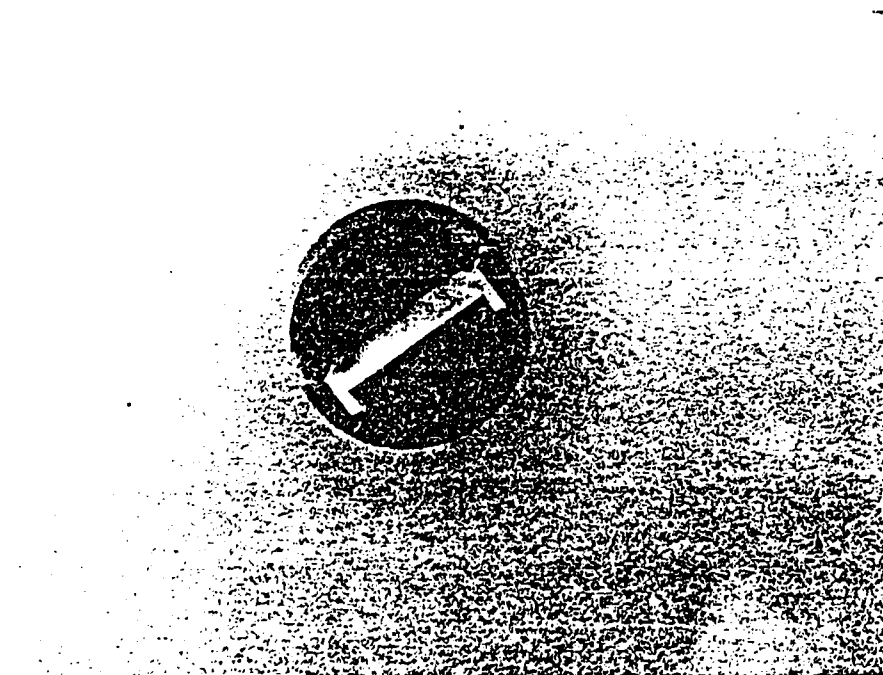


b. Radiograph from part of sample #20 magnified.

Figure 5. Radiographs of TES capsules showing no detectible flaws.

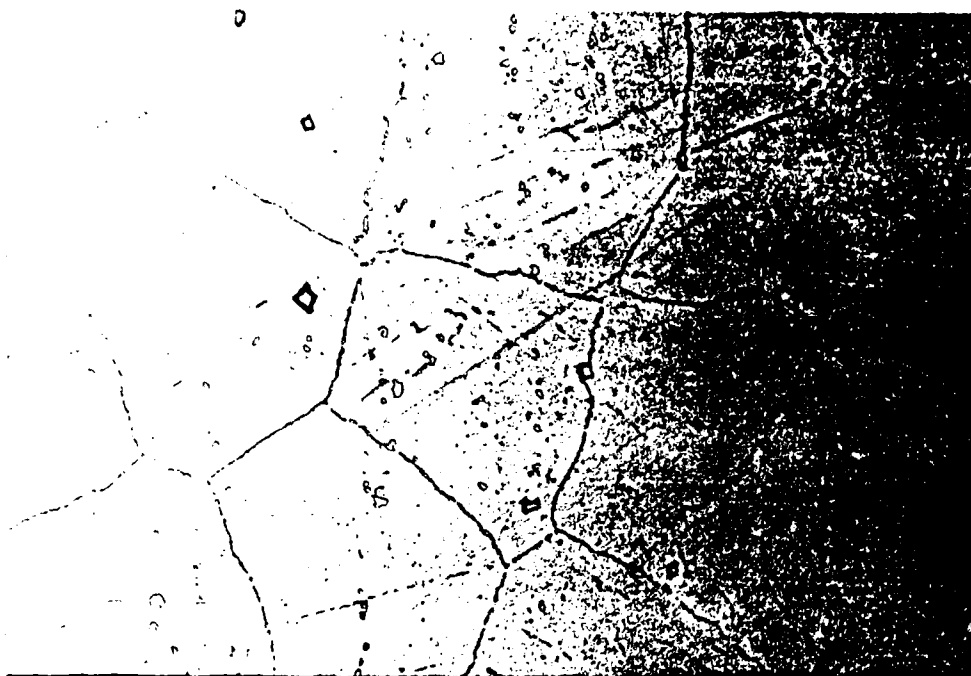


a. Sample cutting schematic from TES capsules.

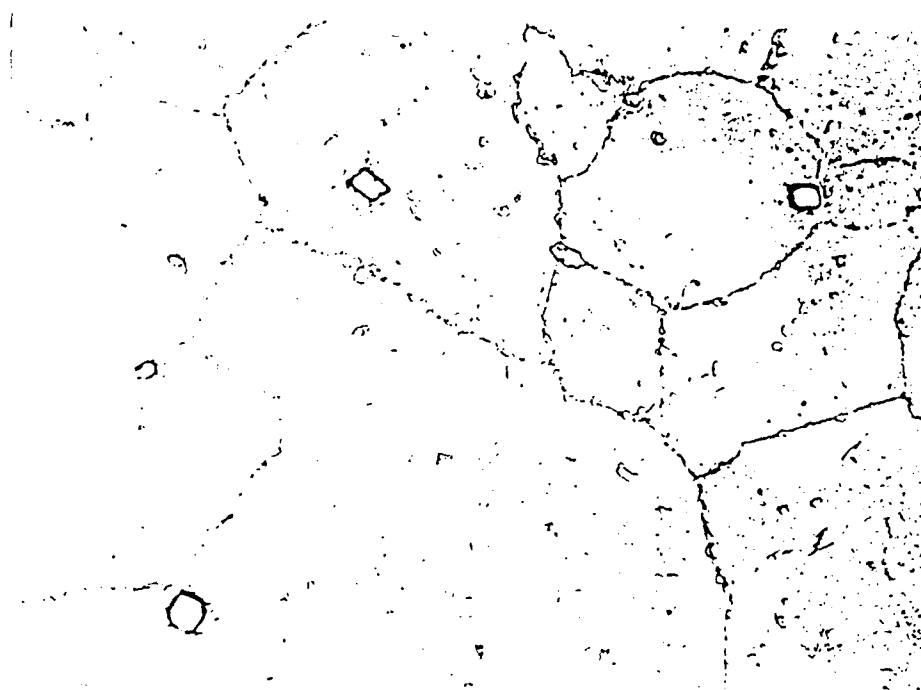


b. Specimen mounted on bakelite.

Figure 6. Sample preparation and mounting

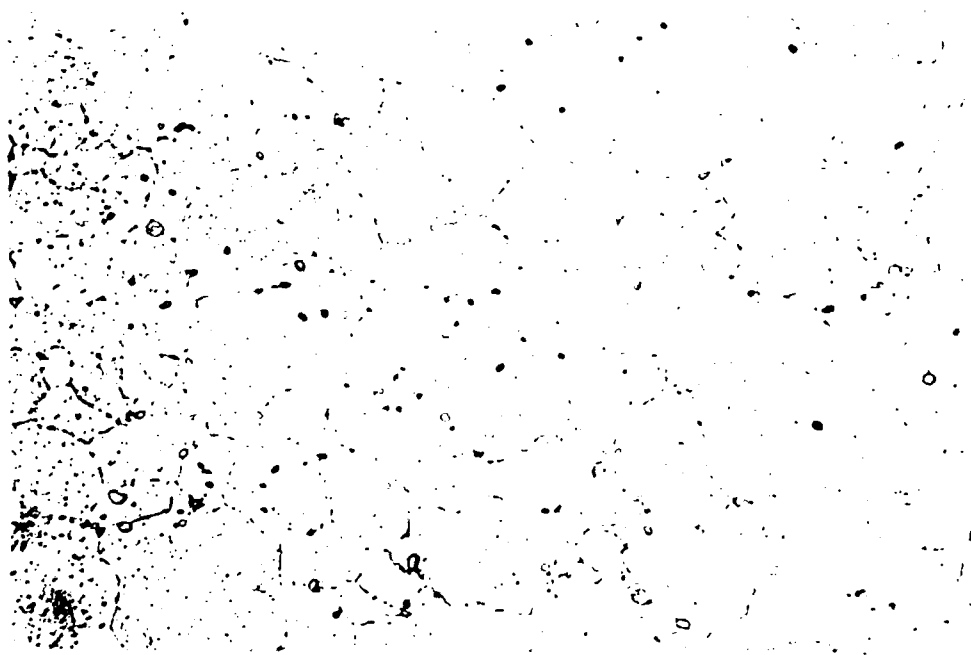


a. Optical micrograph of sample # 14, Aqua regia etch, 500X.

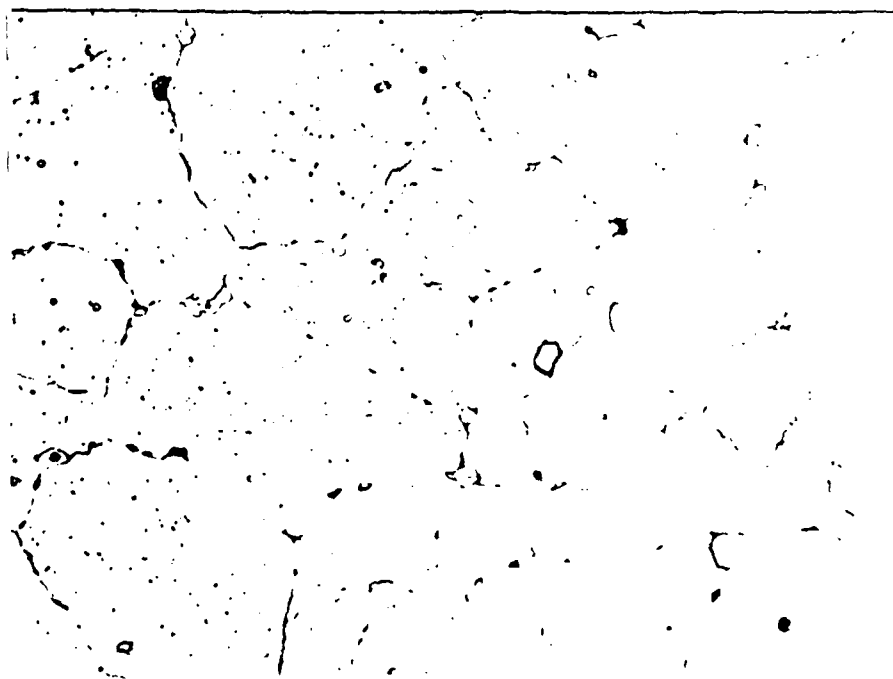


b. Micrograph of sample # 17, 500X

Figure 7. General microstructure of test samples.



a. Optical micrograph of untested I 617 (200X), aqua regia etch.

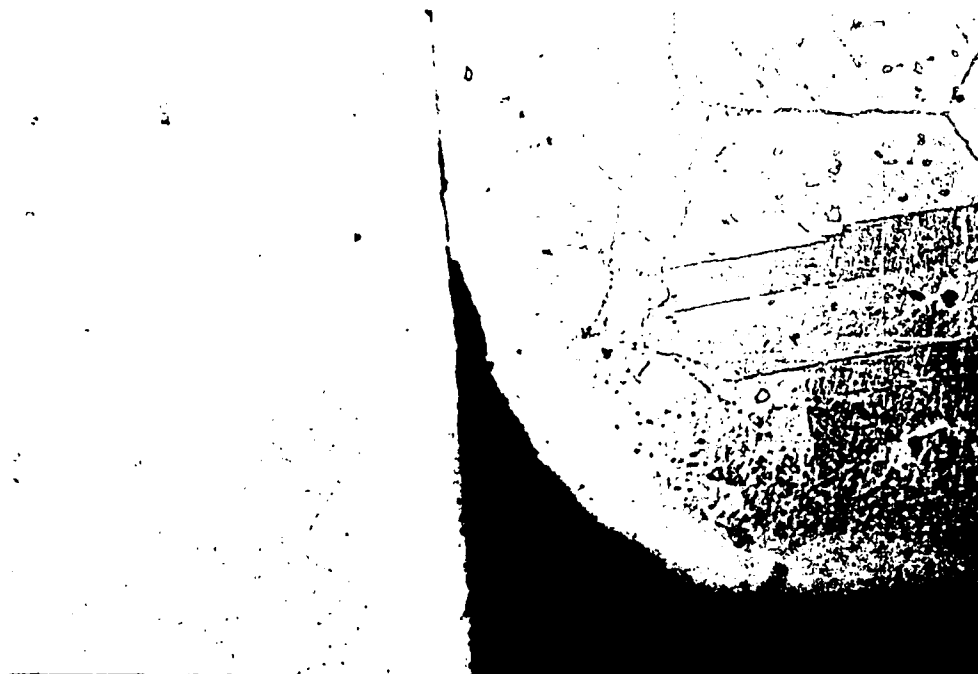


b. Untested I 617 at a higher magnification

Figure 8. Microstructure of untested sample of I 617.

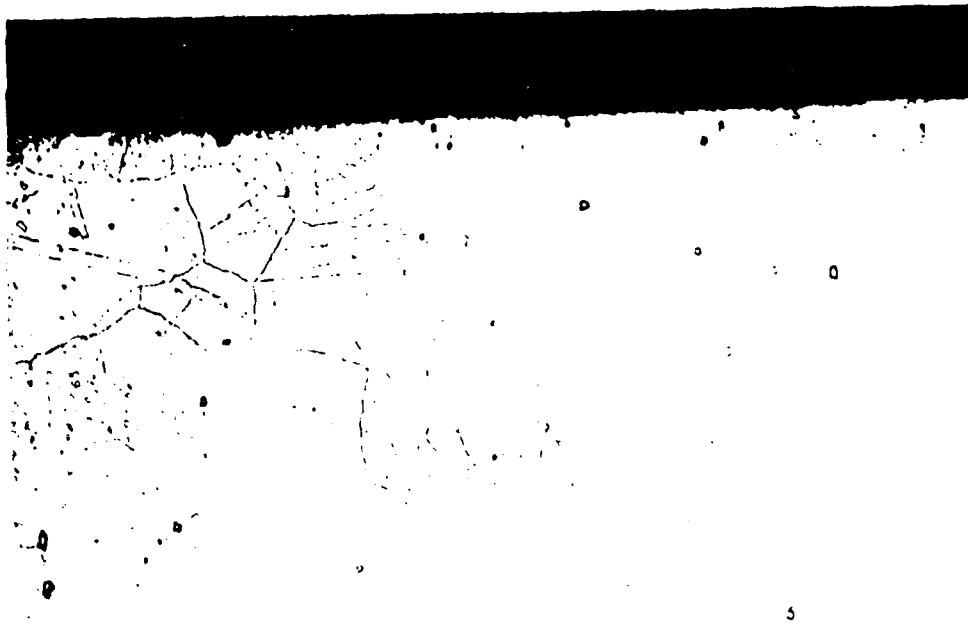


a. Wall profile at low magnification showing the inner edge

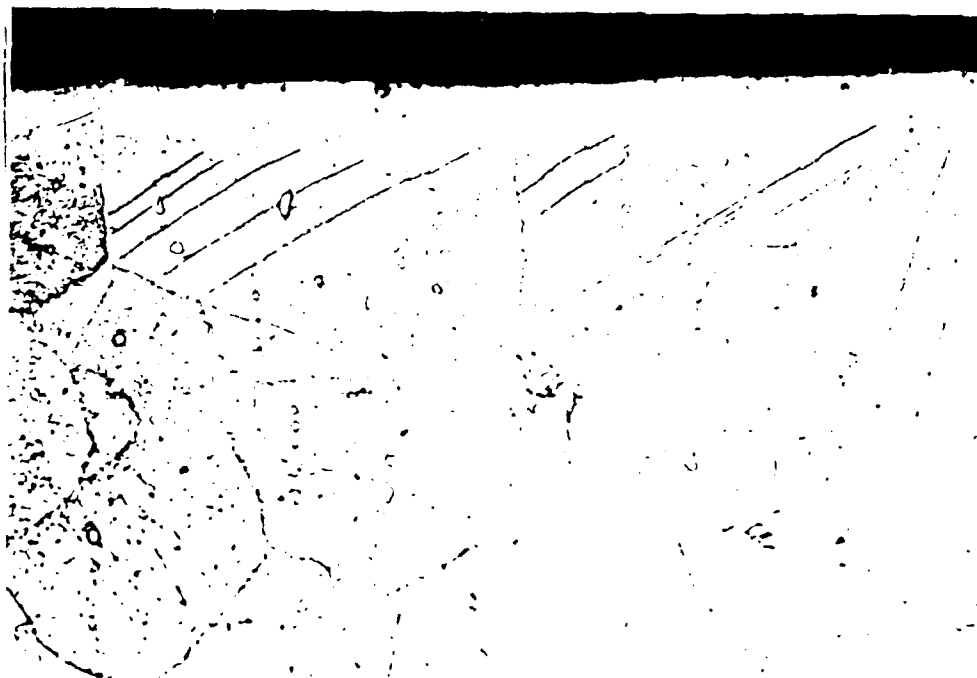


b. Inner edge near end cap at low magnification.

Figure 9. TES capsule wall showing inner edge in contact with salts and outer edge exposed to vacuum.



a. Inner edge of the sample at higher magnification. (100 X).



b. Inner edge at 200 X.

Figure 10. Inner edge damage at various magnifications.

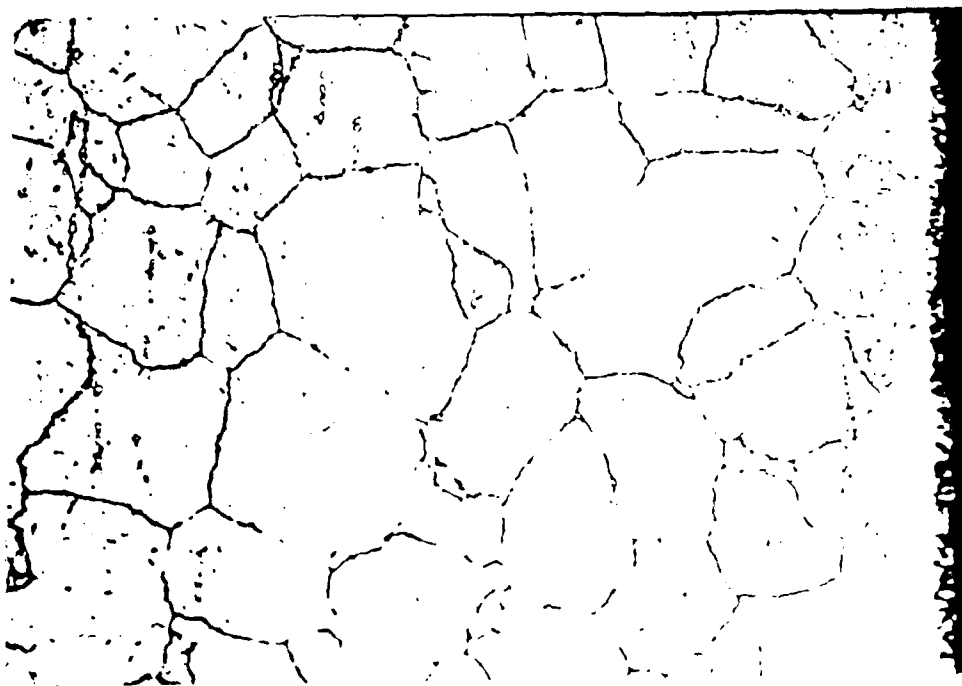
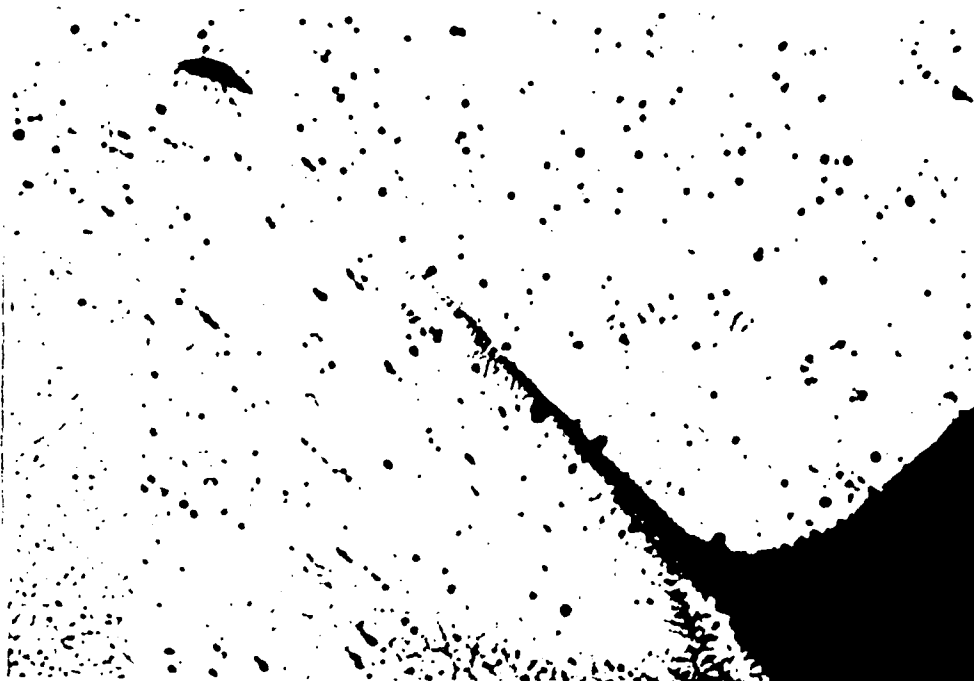


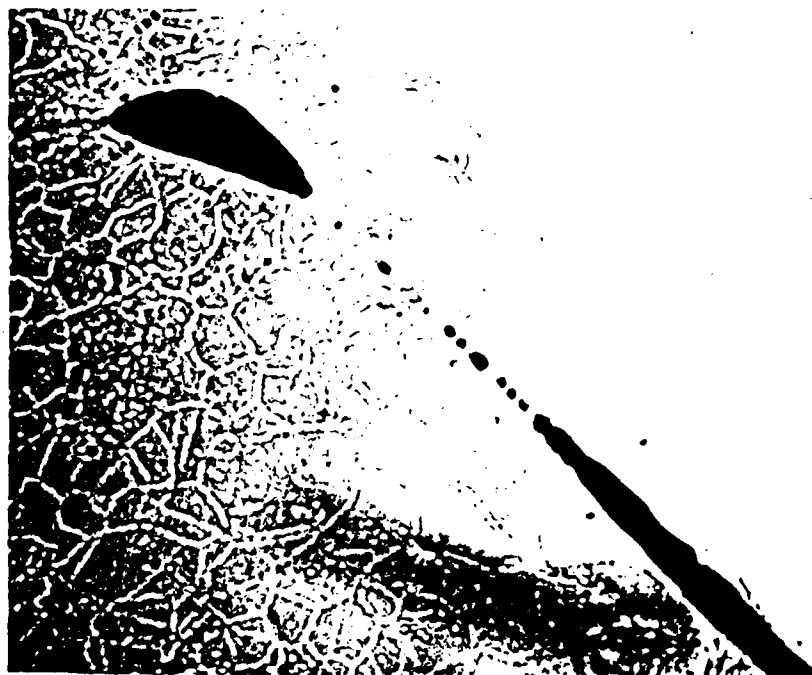
Figure 11. Section of tube wall showing damage on outer edge exposed to vacuum.



Figure 12. Micrograph showing outer edge damage at higher magnification.



a. Gap between end cap and wall (50X).



b. Magnified view of similar gap.

Figure 13. End cap regions at various magnifications.

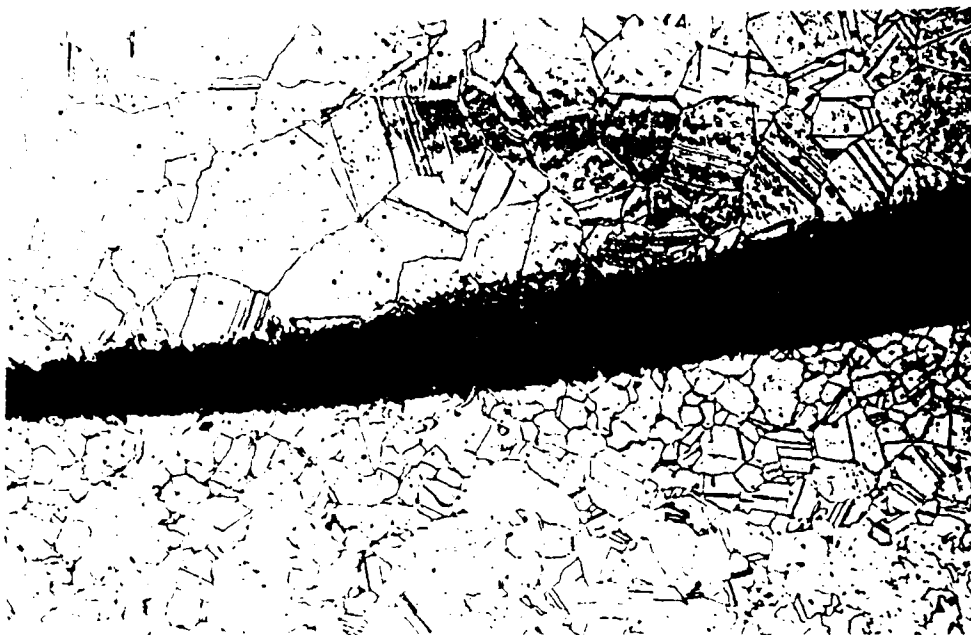


Figure 14. Microstructure across the gap near the end cap region.



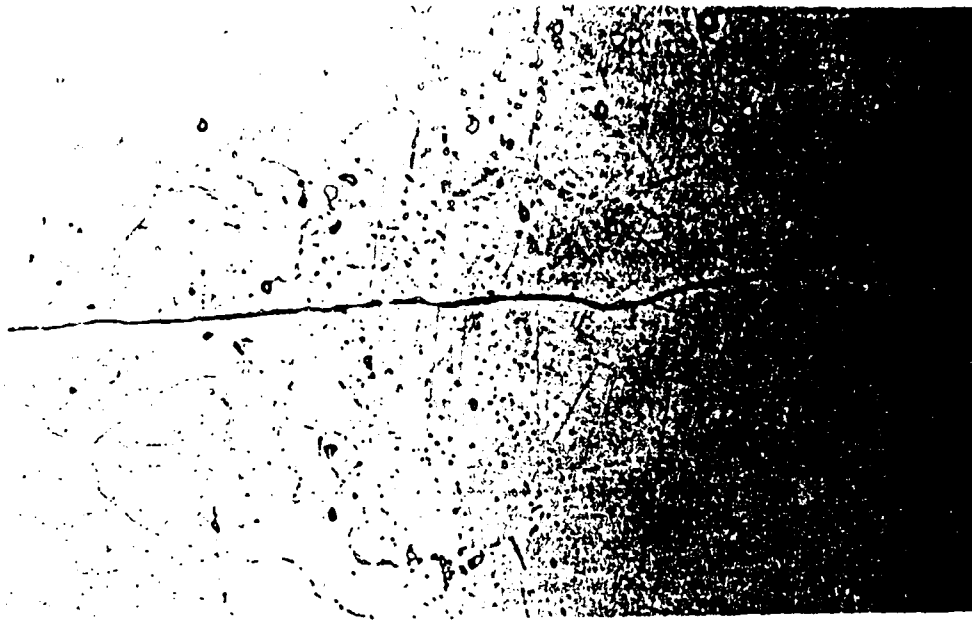
Figure 15. Similar micrograph showing microstructure across gap.



Figure 16. Microstructure near end cap showing edge (X 500)



Figure 17. Microstructure on opposite side of gap (X 500).



a. Discontinuity near the end cap region.



b. Continuation of the previous discontinuity.

Figure 18. Series of discontinuities in the end cap region.



Figure 19. Discontinuous gaps in the end cap regions.

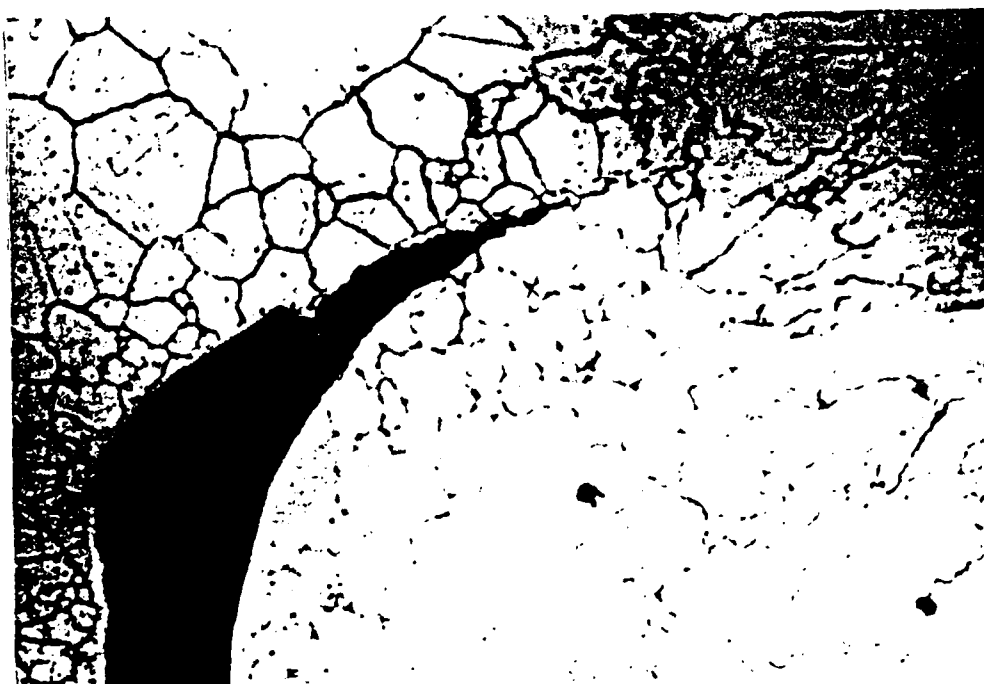
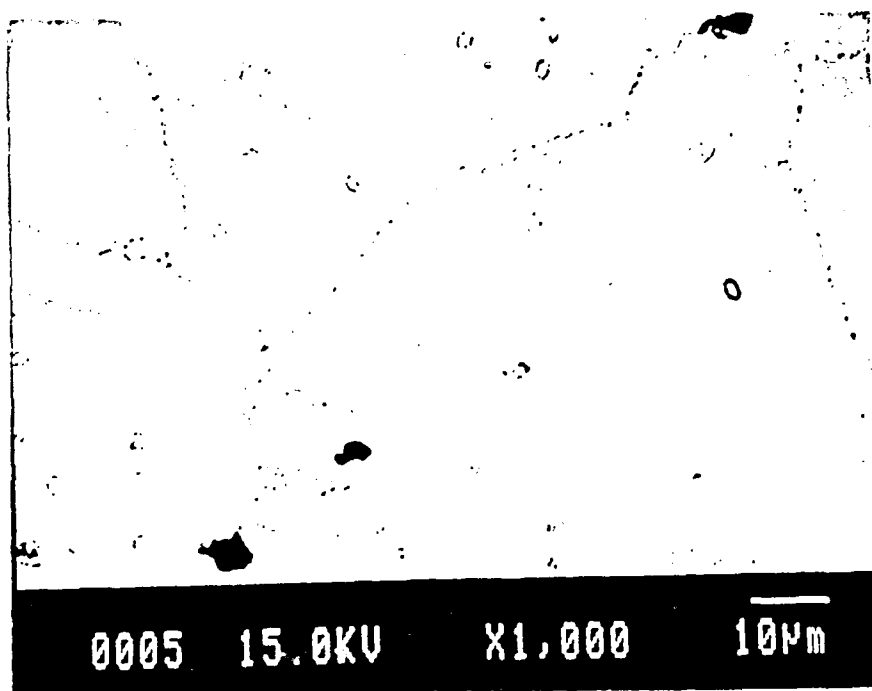


Figure 20. Elongated grains probably due to extrusion or heat effects.

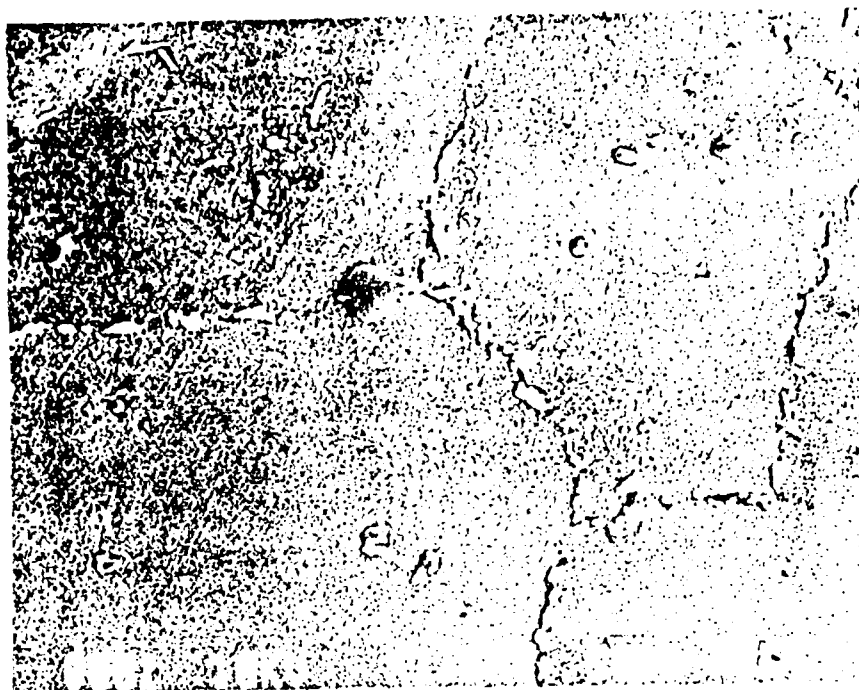


a. Secondary Electron Image (SEI) of #20 showing grain boundary precipitates.

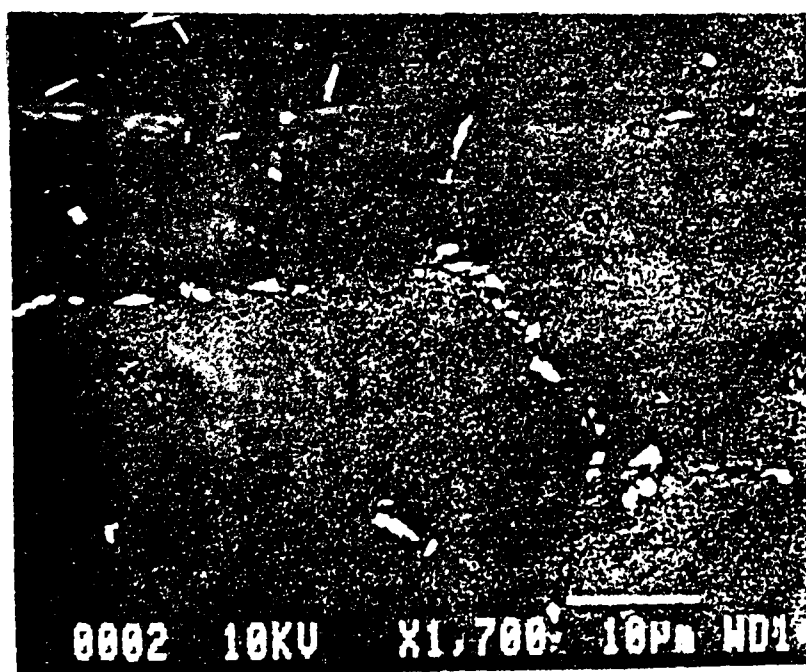


b. Backscattered Electron (BSE) image of # 14 from a different region.

Figure 21. SEM images of tested samples.



a. SEI of sample #20 showing precipitates.



b. BSE image showing three kinds of precipitates in sample # 20.

Figure 22. SEM images of sample #20.

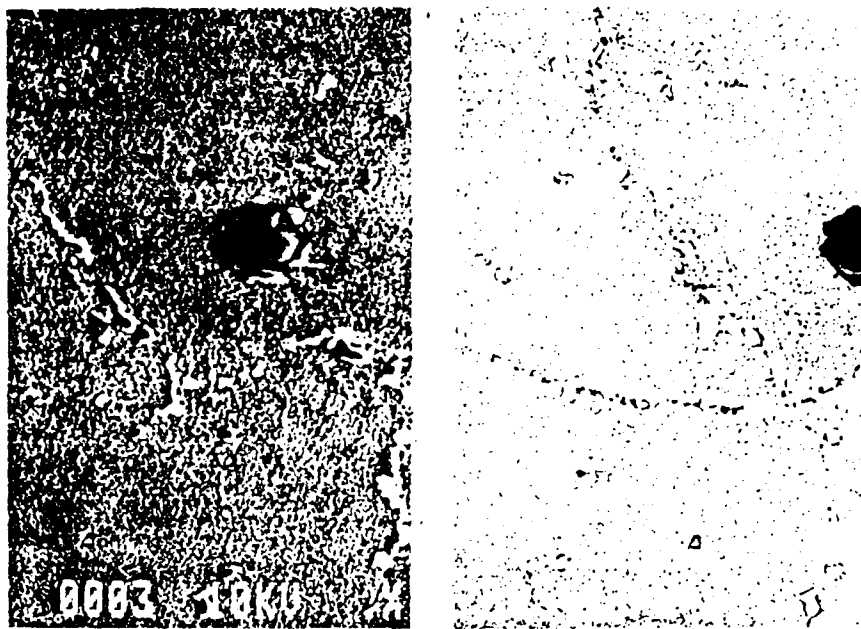


Figure 23. Composite SEI and BSE image of sample # 17 for comparison.

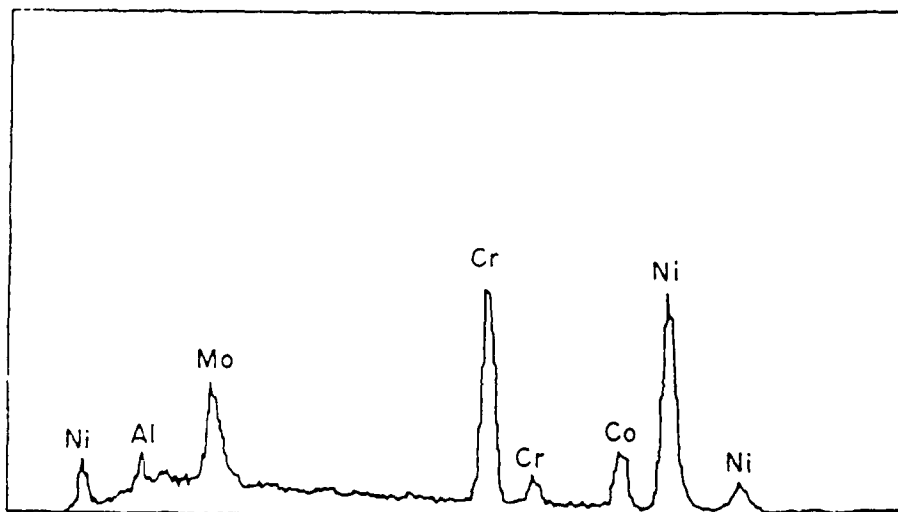
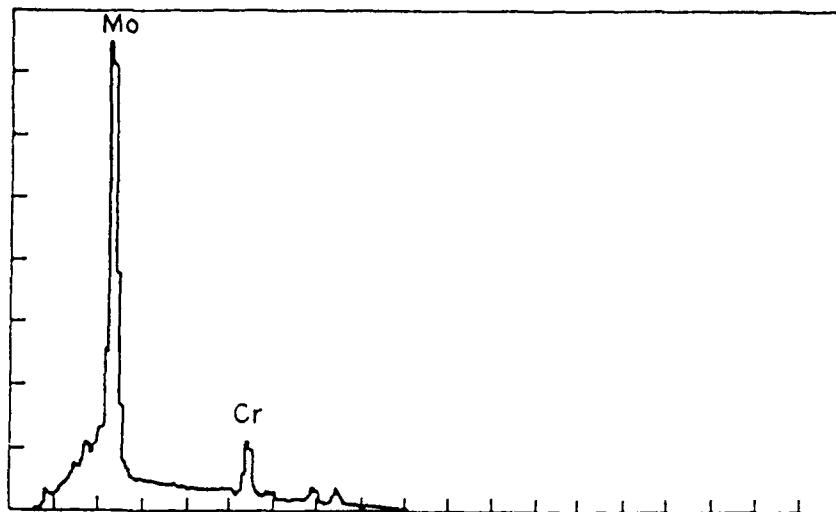
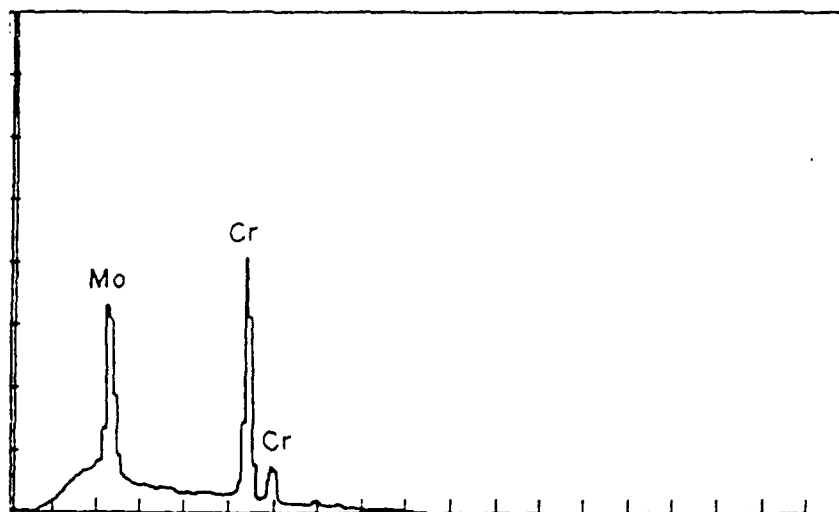


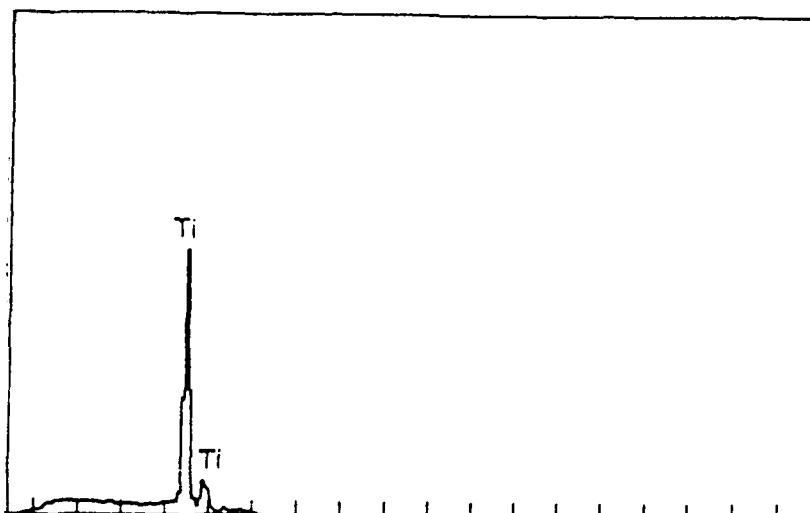
Figure 24. Energy Dispersive X ray spectrum (EDS) of tested sample (#20).



a. EDS spectrum of a Mo rich precipitate.



b. EDS of Cr rich , probably (Cr, Mo) precipitate.



c. EDS of a Ti rich precipitate.

Figure 25. EDS plots of the various phases in the samples.

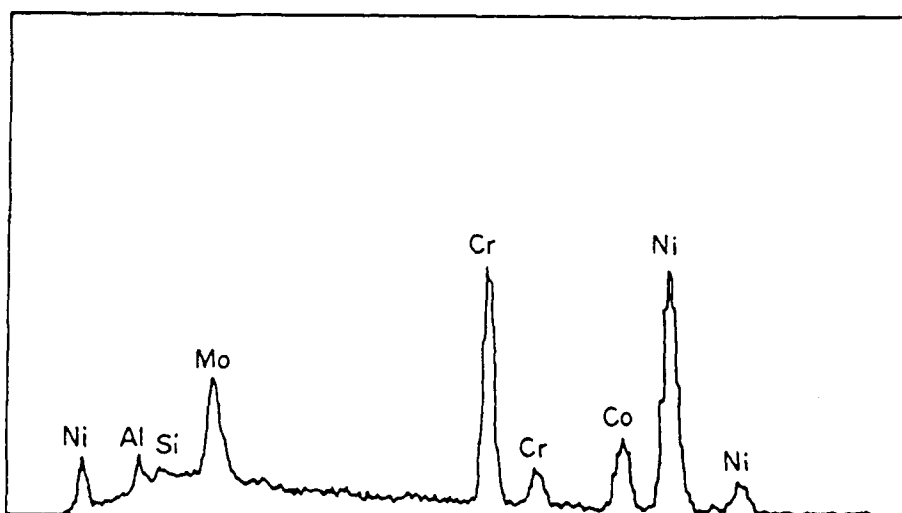
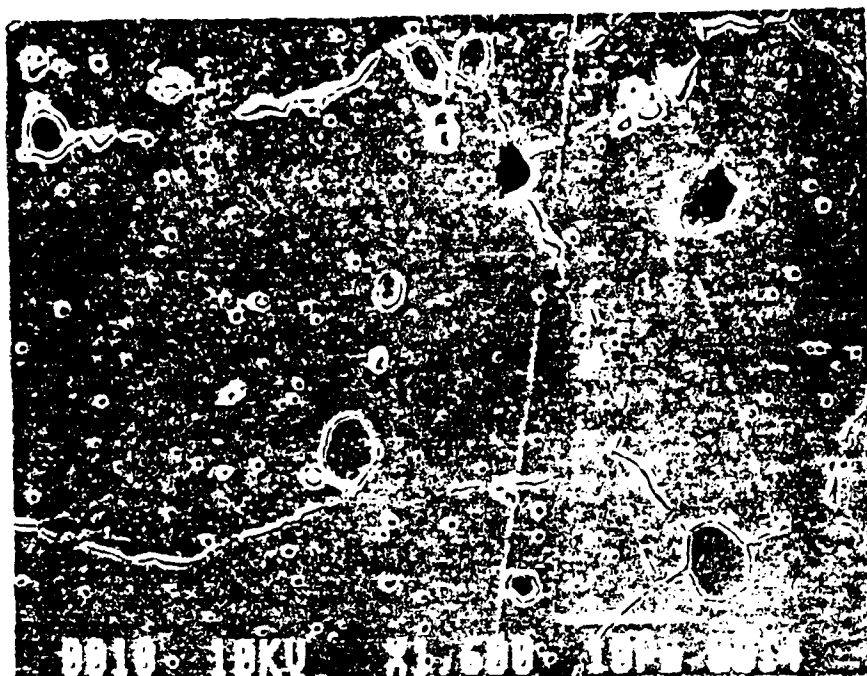
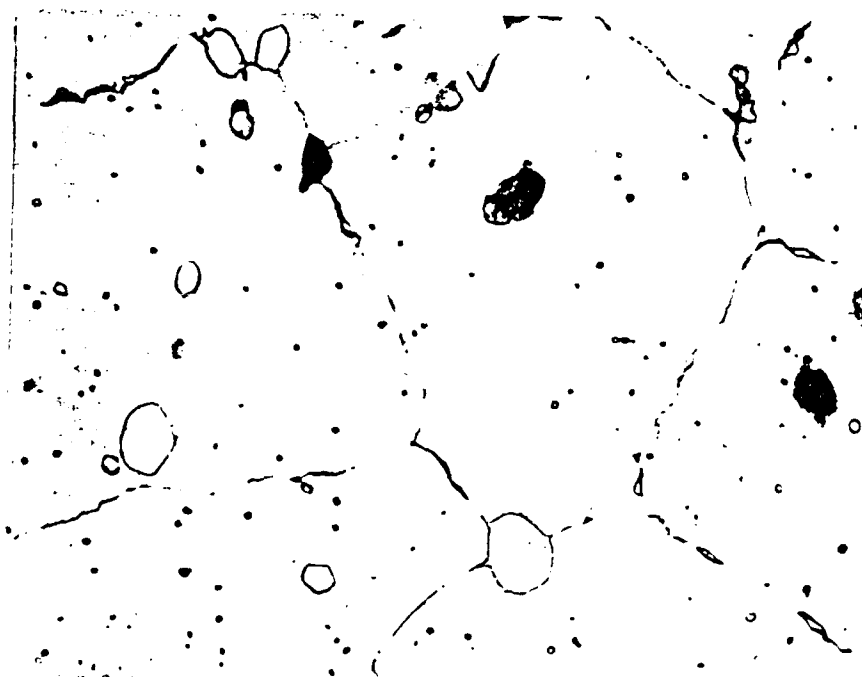


Figure 26. EDS plot of untested sample of I 617.



a. SEI image of untested I 617.

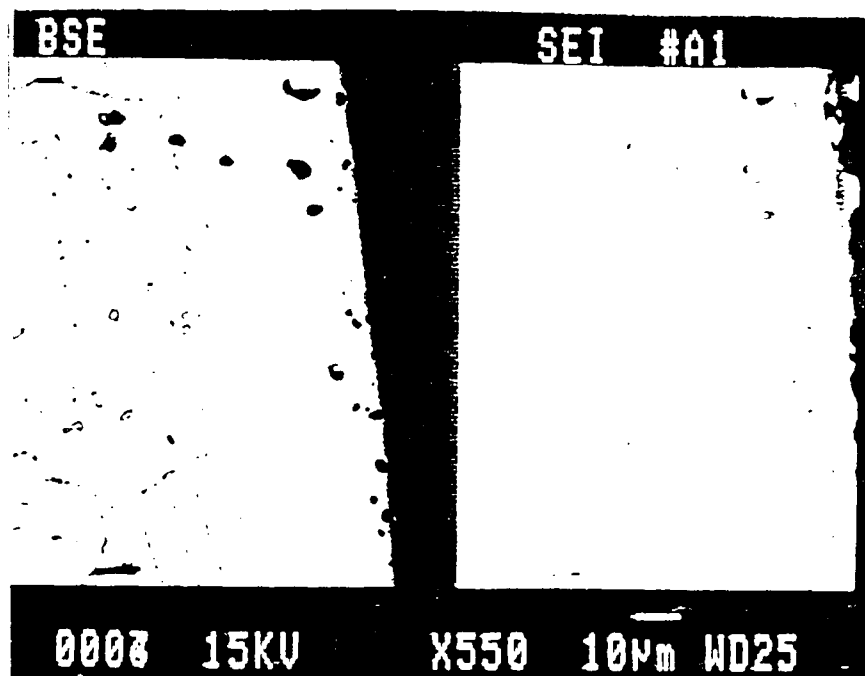


b. BSE image of untested I 617.

Figure 27. Details of composition of untested sample of I 617.

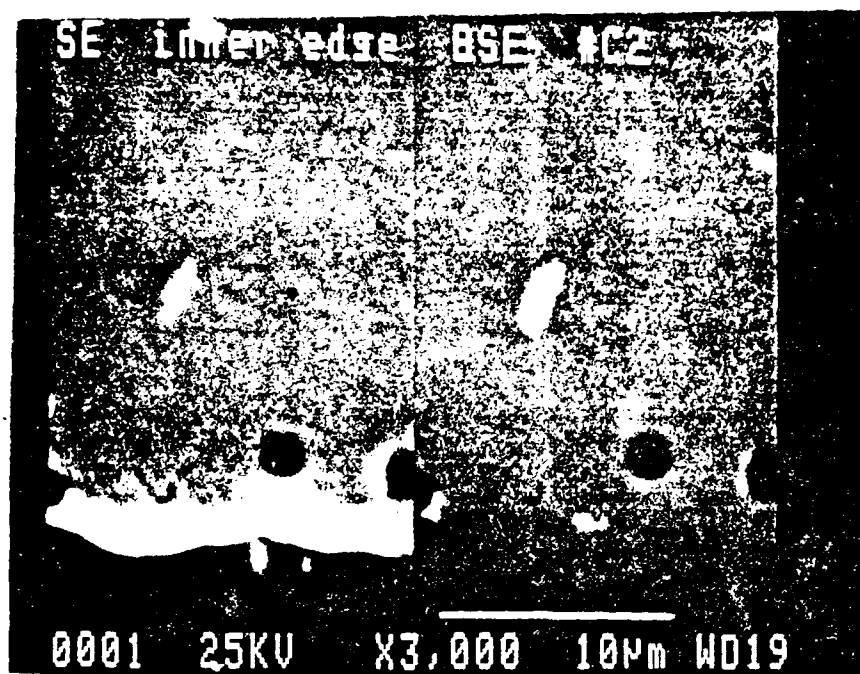


a. Inner edge profile of sample #20 showing damage.

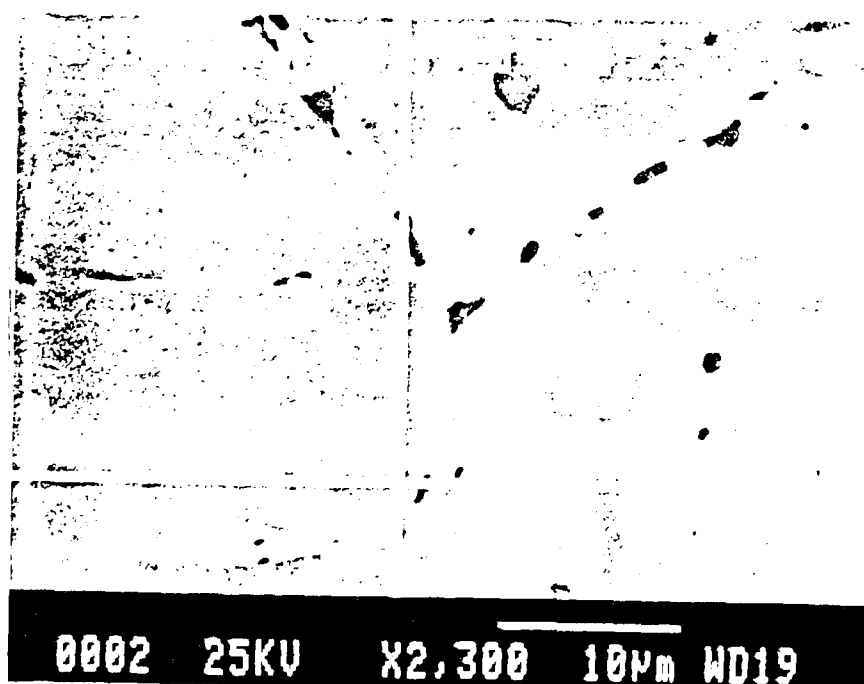


b. Composite image of inner edge of sample #20.

Figure 28. Microstructure of the inner edge in contact with the salt.

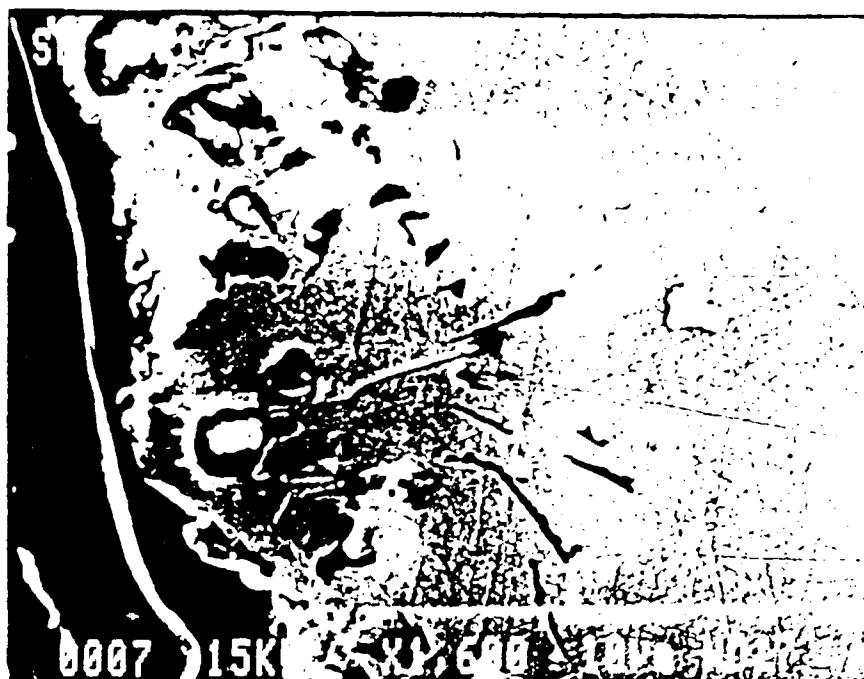


a. Inner edge region in sample # 17.

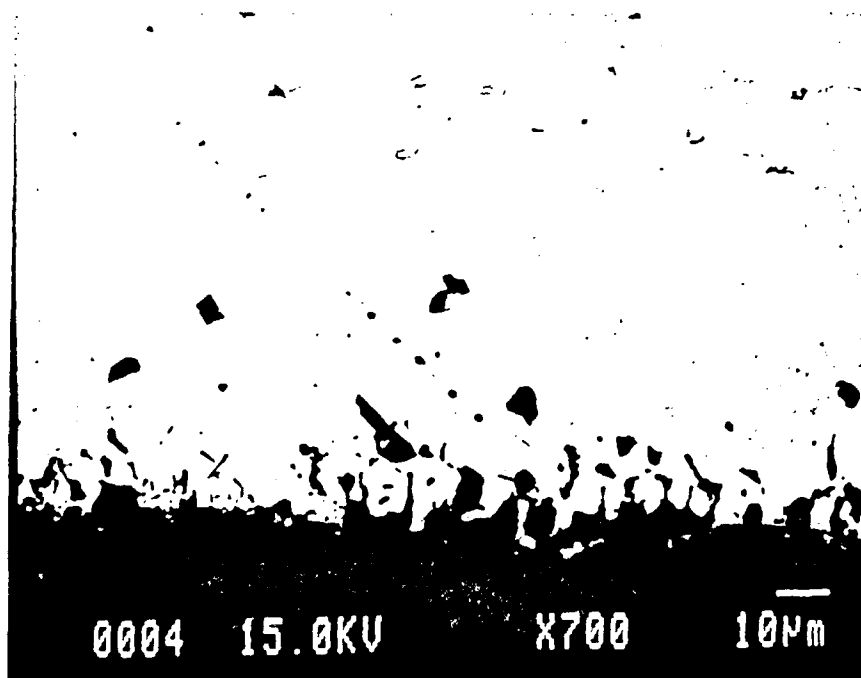


b. BSE image of grain boundary near the edge.

Figure 29. Images near the inner edge of sample # 17.

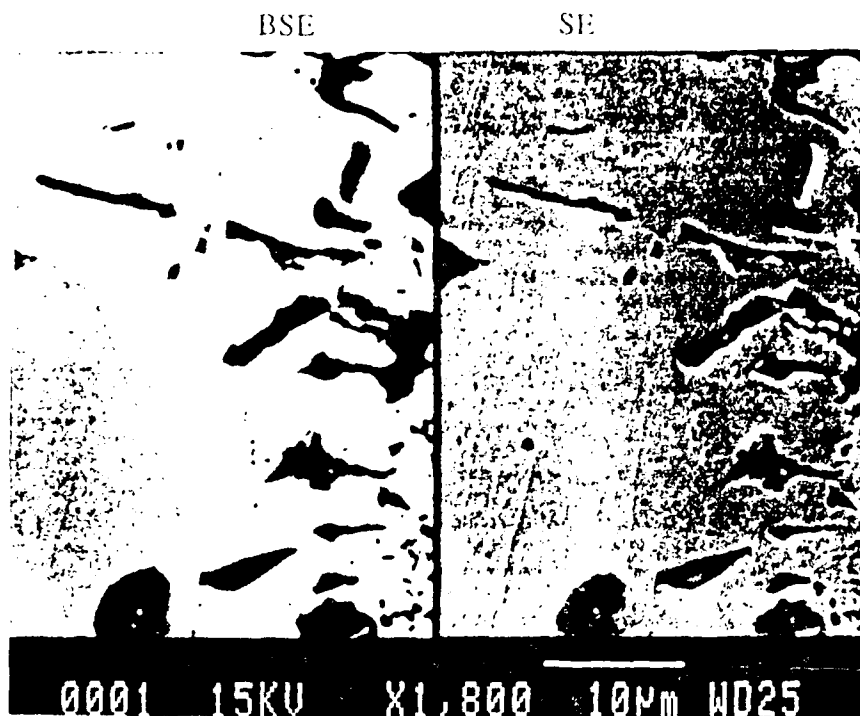


a. SEI of outer edge profile.

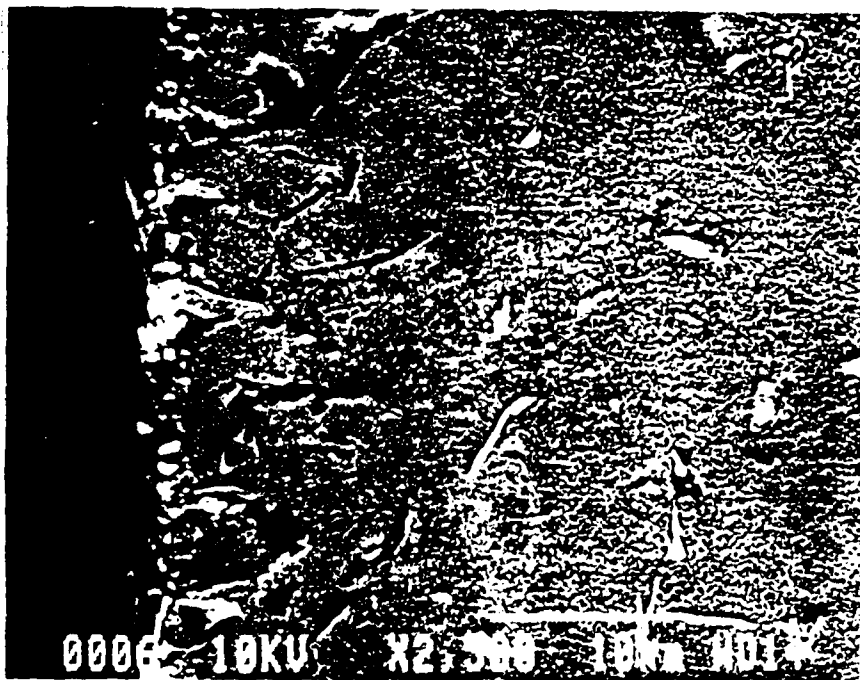


b. BSE of a different region near the outer edge.

Figure 30. Microstructural damage near the outer edge exposed to vacuum.

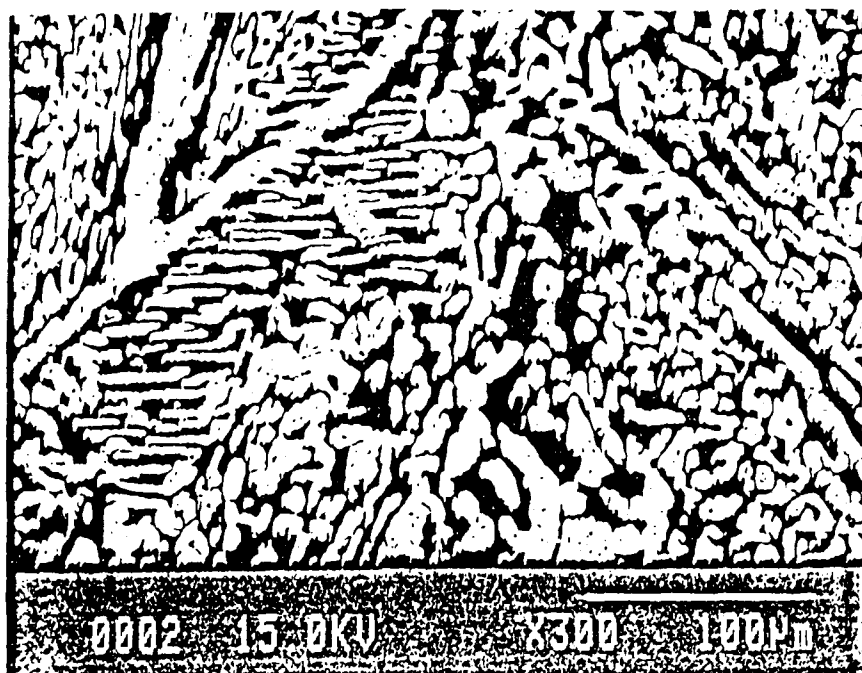


a. Composite image of outer edge damage extending to about 30 microns.

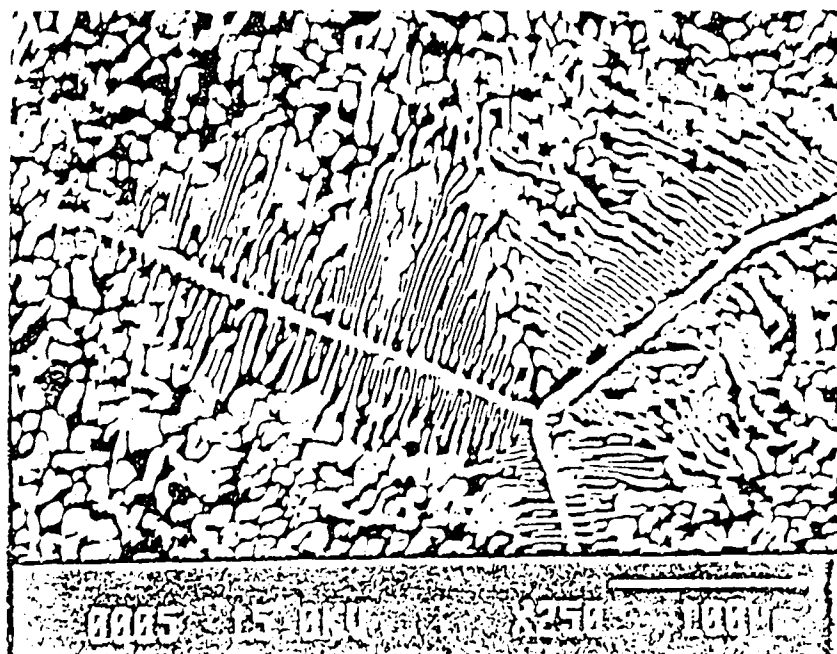


b. SEI image of the outer edge region showing elongated precipitates.

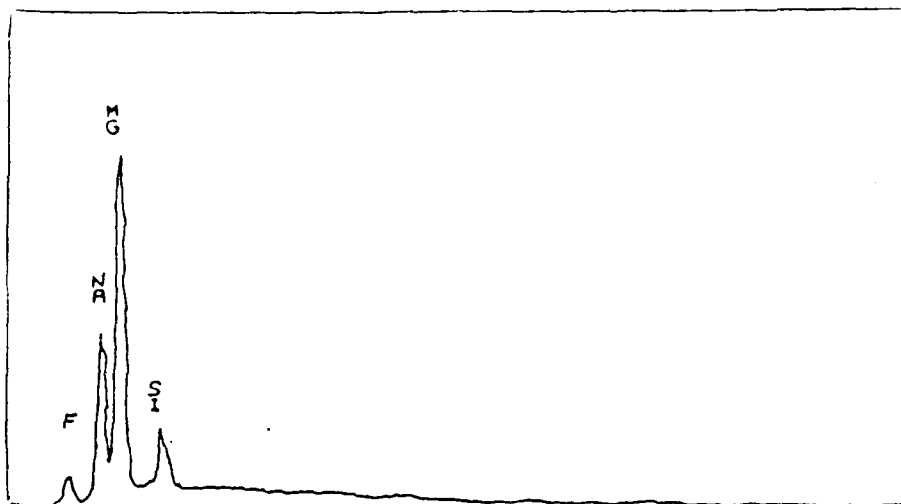
Figure 31. Extent and form of outer edge damage.



a. Eutectic solidification structure of salt A in BSE mode.



b. Eutectic structure of salt B.



c. EDS plot of eutectic B.

Figure 32. Characterization of the eutectic salt.

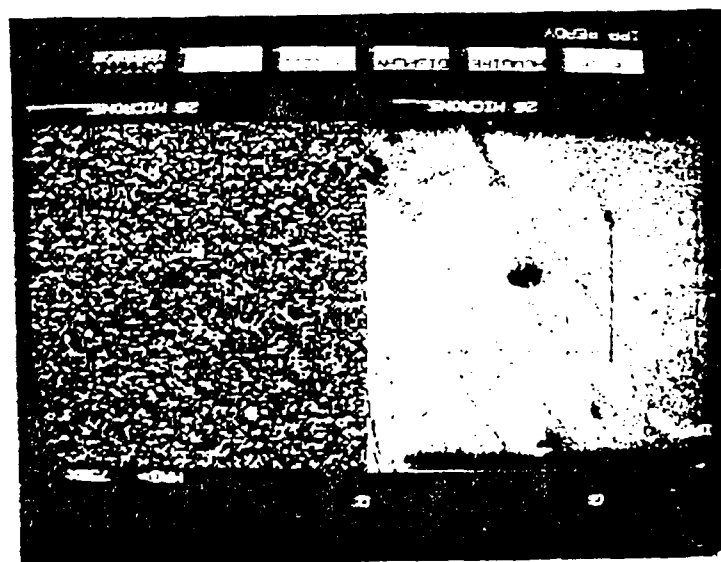
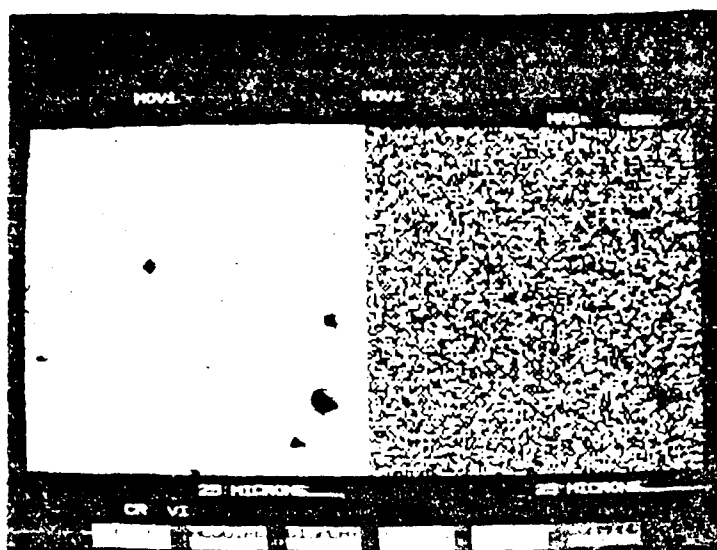
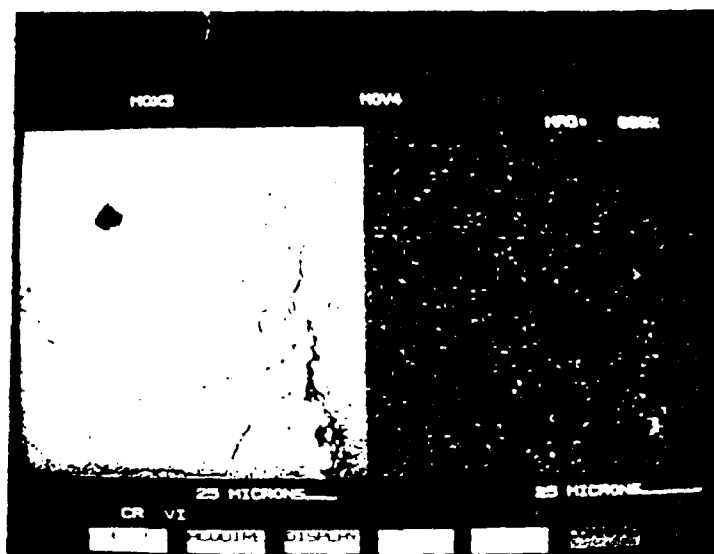


Figure 33. Composite X-ray map of Cr $K\alpha$ and Video image on the left.

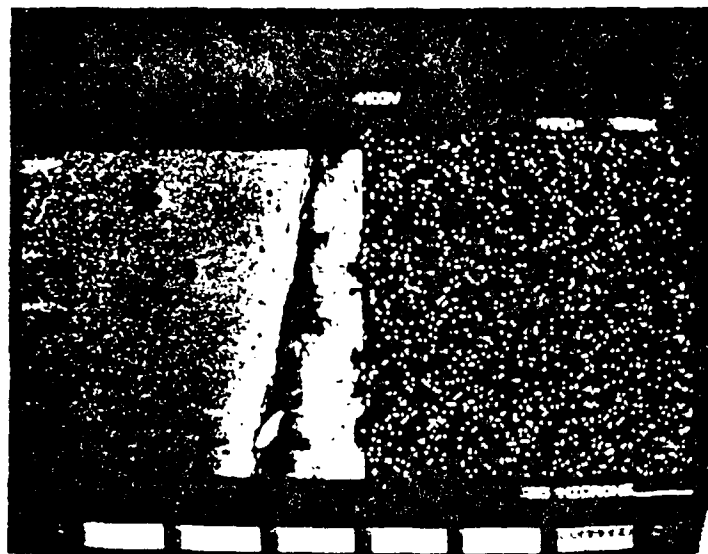


a. Mo L_{α} X-ray map showing general microstructural distribution.

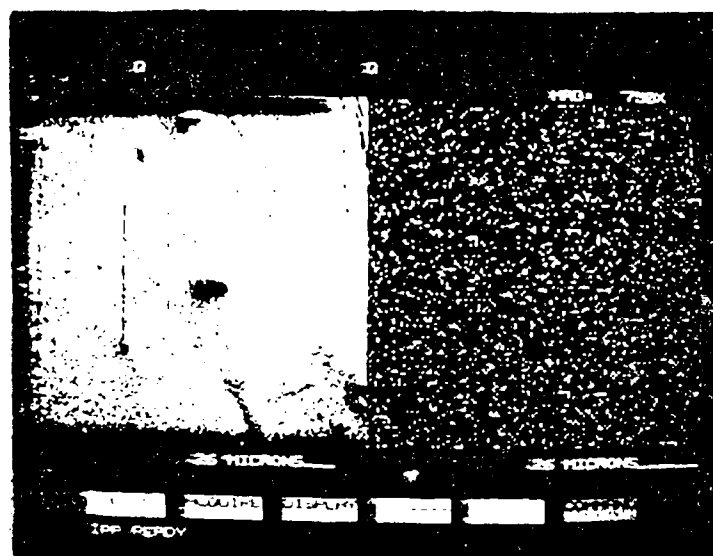


b. Al distribution in general microstructure.

Figure 34. General microstructure and elemental distribution.



a. Al K_{α} X-ray map near the inner edge.

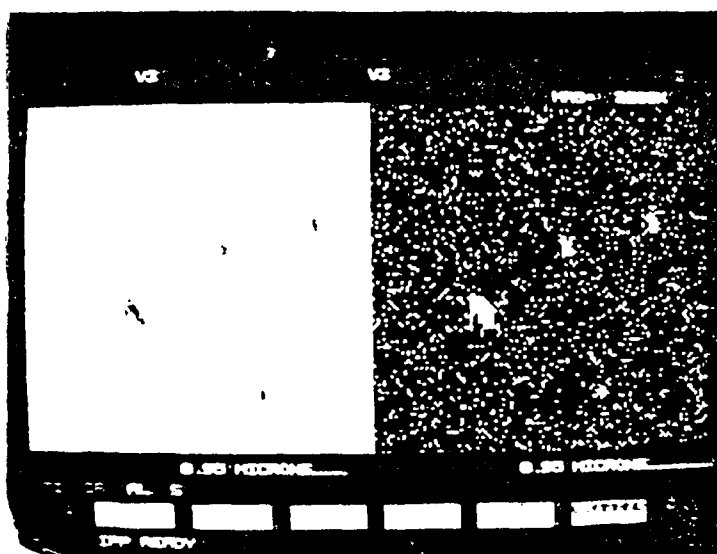


b. Similar Al map from different edge region.

Figure 35. Al distribution showing slight indication of near edge depletion.



a. Cr distribution near end cap region.



b. Ti distribution in the microstructure.

Figure 36. Elemental maps near end cap region.

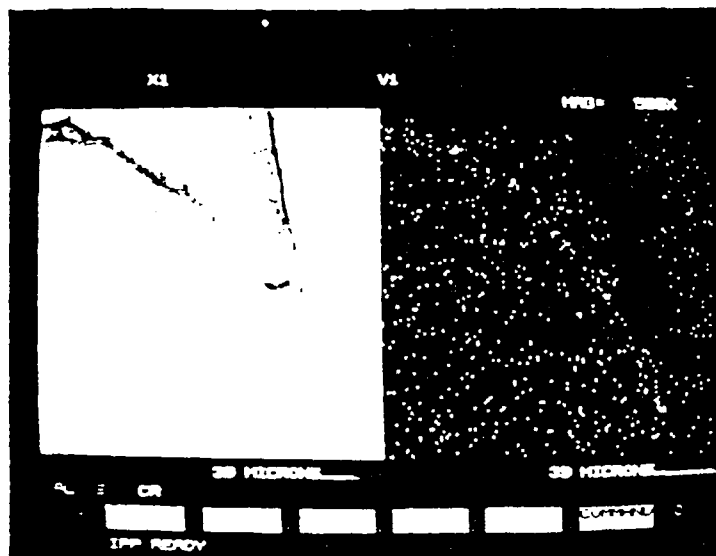


Figure 37. Al distribution near end cap showing alumina in crevice due to polishing.

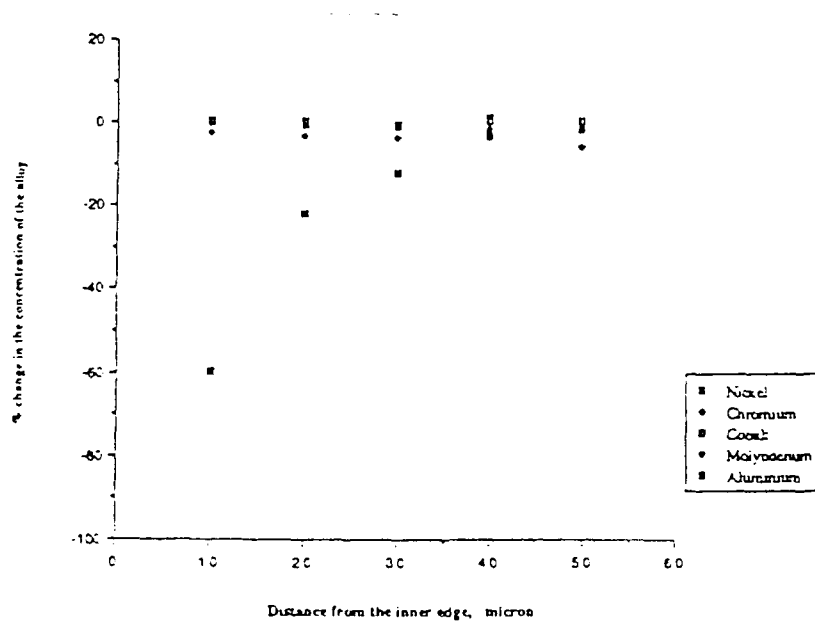
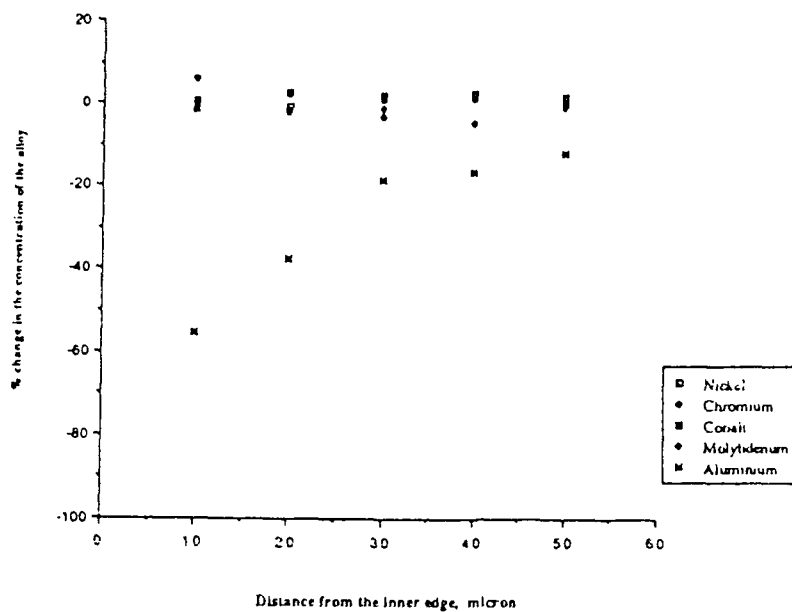
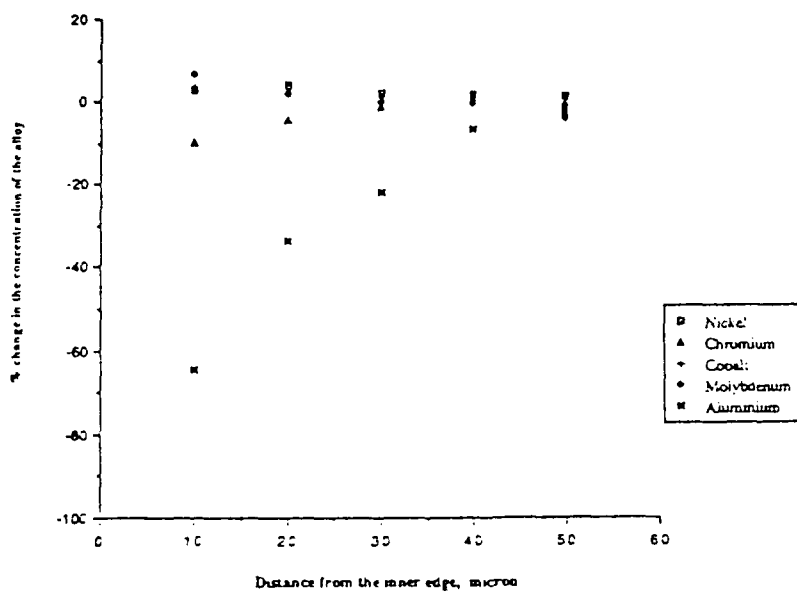


Figure 38. Normalised change in concentration of constituents in #14.



a. Normalized Change in Concentration of Constituents in #17.



b. Normalised change in concentration of constituents in #20.

Figure 39. EPMA determinations of the concentration profile across the tube wall upto 50 microns from inner edge.

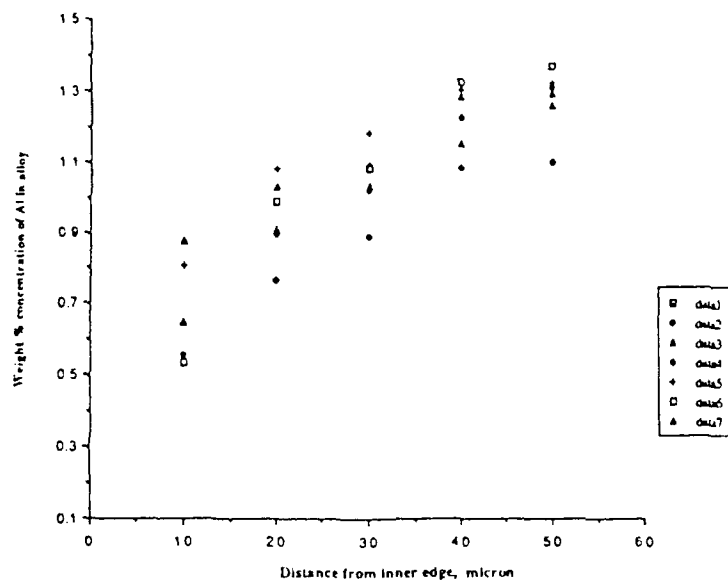


Figure 40. Plots of the weight percent concentration of Al versus the distance from the inner edge of the tube wall as determined by EPMA.

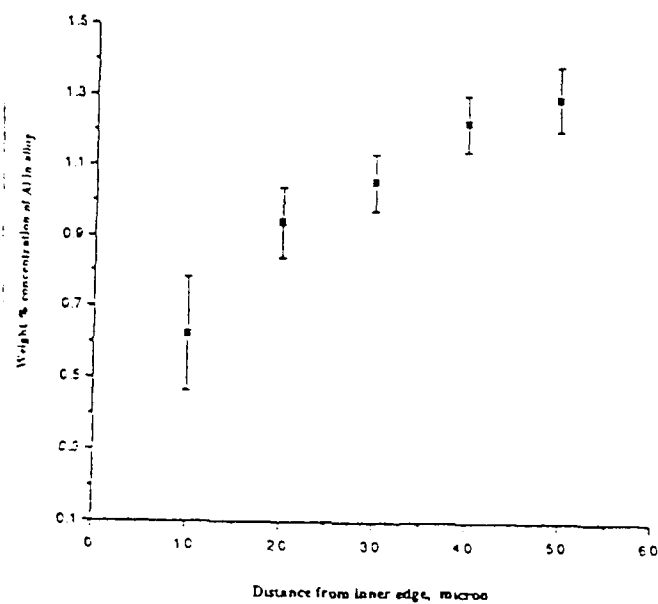


Figure 41. Plot of the average concentration of Al as determined from Fig.40. above.

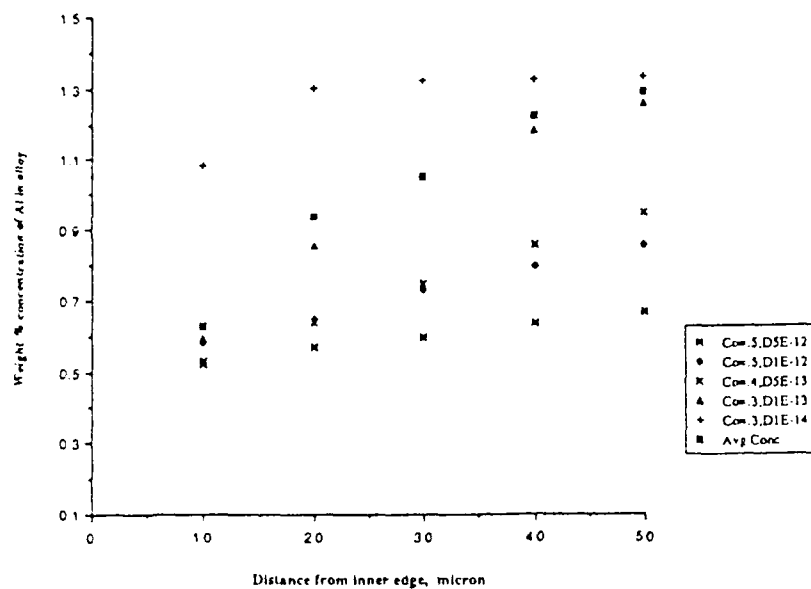


Figure 42. Plots based on the diffusion model with varying C_0 and D and compared to the average experimental values obtained from above.

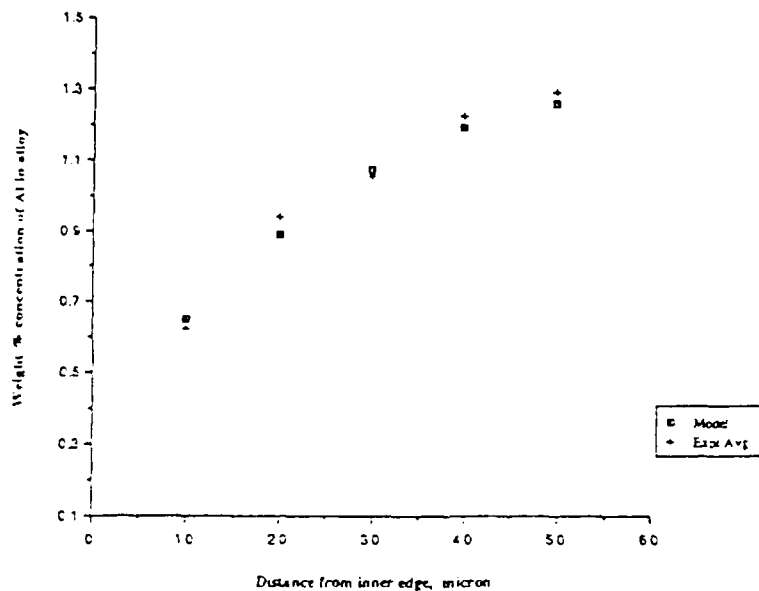


Figure 43. Diffusion curve based on the best fitting C_0 and D from least squares analysis and compared with the experimental curve.

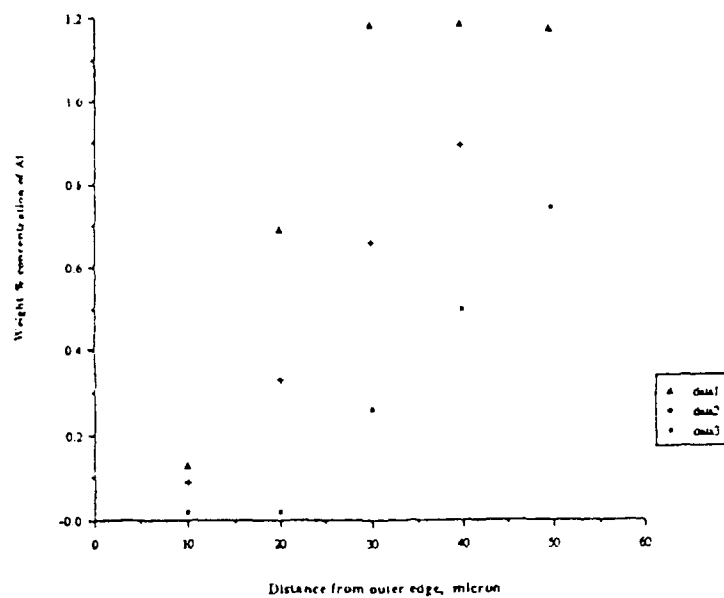


Figure 44. Concentration Profile of Al near the Outer Edge Exposed to Vacuum.

APPENDIX C

Data Tables

Table I. Weight Percent Compositions of the Eutectic Salts

	Eutectic A	Eutectic B	Eutectic C
LIF	42.27	39.83	46.94
MgF ₂	48.76	47.05	53.06
NaF	-----	13.12	-----
KF	8.95	-----	-----

Table II. Nominal Composition of the Container Alloy in Weight Percent

	Ni	Cr	Co	Mo	Al	Ti	Fe, Si, C
1617 Container	54.8	21.8	12.6	8.6	1.34	0.2	Rest

Table III. Weight Percent Composition of Alloy #17 Near Inner Edge

Dist. from inner edge (microns)	Ni	Cr	Mo	Co	Al
10	55.4	21.2	8.4	12.7	.65
20	55	21.2	8.3	13	.91
30	55.3	21.1	8.5	12.8	1.09
40	54.8	22.1	8.3	12.8	1.15
50	55.6	22.3	8.3	12.9	1.26

Table IV. Weight Percent of Al and Cr in the Tested Salts

	Eutectic A	Eutectic B	Eutectic C
Aluminium	0.31	0.25	0.29
Chromium	0.00034	0.00043	0.00043

Table V. Weight Percent Composition of Alloy #17 Near Outer Edge

Dist. from Outer edge (microns)	Ni	Cr	Mo	Co	Al
10	58.3	14.3	10.6	13.6	.11
20	58.2	15.8	9.9	13.6	.1
30	58.4	18	8.6	13.1	.33
40	56.9	20.0	8.2	13.2	.66
50	56.1	21.0	8.1	12.8	.89

REFERENCES

1. A. K. Misra and J. D. Whittenberger: J. Electrochem Society, 1988, Vol. 135, 4, pp 850.
2. R. Ponappan, J. E. Beam et al: 20th Intersoc. Energy Conv. Engg Conference, 1982, pp. 202.
3. W. Smyrl: SAND - 79 - 0246C, 1978 pp. 2.
4. G. A. A. Asselman: Energy Conversion 1976, Vol. 16 pp. 35.
5. A. K. Misra and J. D. Whittenberger: J. Materials Engg., 1987, Vol. 9, pp 293.
6. J. E. Davison: AFAPL-TR-75-92, October 1975, pp. 20.
7. J. E. Beam et al: AFAPL-TR-75-92 part II, March 1977.
8. D. Jacobson: AFWAL-TR-81-2122, 1982, pp. 138.
9. A. K. Misra and J. D. Whittenberger: J. Materials Energy Systems, 1987, Vol. 8 pp. 4.
10. J. E. Davison: AFAPL-TR-77-70.
11. A. K. Misra and J. D. Whittenberger: NASA Technical Memorandum, 87320, May 1986.
12. J. W. Koger: Adv Corr Sci and Tech., 1974, Vol. 2, pp. 245.
13. A. K. Misra and J. D. Whittenberger: Intersociety Energy Conversion Engineering Conference (IECEC), 1987.
14. Y. K. Rao: Met Trans B, 1982, Vol. 14B pp. 701.
15. J. Lumsden: *Thermodynamics of molten salt mixtures*, 1966, Academic Press.
16. D. E. Tracy et al: IECEC, 1987, pp. 169.
17. Phillip Daniel and R. A. Rapp: Adv Corr Sci and Tech., 1975, Vol. 5, pp. 55.
18. S. N. S. Reddy and R. A. Rapp: Met. Trans B, 1980, 11B, pp. 533.
19. A. deS Brasunas: Metals Progress, 1952, Vol. 62, 6, pp. 68.
20. D. Jacobson: AFWAL-TR-77-9, 1977, pp. 5-6.
21. Sims and Hagel: *The Superalloys*, John Wiley and Sons.
22. Metals Handbook: 9th Edition, Vol. 9, ASM International.

23. Pankratz, Stuve et al: *Thermodynamic data for mineral technology*, ed. 1984, Bureau of Mines, Bulletin 677.
24. Evans, Koger and DeVan: ORNL 4575, Vol. 2, June 1971.
25. Diffusion and Defect Data: 1977, Vol. 15, pp. 108.
26. Venkatesetty and Saathof: International symposium of molten salts proc. 1976, pp. 329.
27. G. Baudo et al: Corrosion, 1970, Vol. 16, 7, pp. 193.
28. Nishikata and Haruyama: Corrosion, 1986, Vol. 42, 10, pp. 578.
29. D. G. Lovering and R. J. Gale: '*Molten salt techniques*' Eds. 1983, Vol. 1, 2, 3, Plenum Press, N. Y.

PART II

THE REFLECTIVITY OF SUPERALLOYS AT 10.6 MICRONS

2.1 Introduction

In many high temperature systems, stainless steels and superalloys are often used as structural materials. Consequently, the radiative properties of these materials become important parameters. To effectively heat a metal with a laser, the absorptivity of the metal must be known at the wavelength of interest. This can be determined from the spectral emissivity of the material. For opaque materials, the spectral emissivity is related to the spectral reflectivity through the relationship

$$\epsilon_{\lambda} = 1 - R_{\lambda} \quad (1)$$

The spectral reflectivity (and consequently the emissivity) of a metal alloy is influenced by many factors including the temperature at which the tests are performed, the composition of the alloy, the surface roughness, whether or not an oxide is present (and if so, the thickness of this oxide), the wavelength of the incident radiation, and the laser characteristics (power, CW or pulsed).

2.2 Literature and Background Research

For pure nickel, the reflectivity ranges from approximately 10% at 0.1 microns to >90% at wavelengths longer than 4 microns [1]. This is true of all pure metals, with the reflectivity being the highest in the infrared, usually greater than 90%. Table 2.1 presents the values of the emissivity of many pure metals at 20°C for various laser wavelengths, and Fig. 2.1 presents the variation with wavelength of the normal spectral emissivity for a variety of polished metals at elevated temperatures. With the exception of copper, all the metals exhibited the same trend of decreasing spectral emissivity (i.e. increasing spectral reflectivity) with increasing wavelength. Fig. 2.2 illustrates the effect of wavelength and surface temperature on the hemispherical spectral emissivity of tungsten. It is evident that the temperature effects are much smaller than the wavelength effects (under vacuum conditions). Fig. 2.3 shows the effect of wavelength on the directional spectral emissivity of pure titanium.

The values in Table 2.1 show that generally the absorption of laser radiation is almost an order of magnitude larger in the visible region than in the infrared. Yet these tests were performed

on very clean pure metal surfaces under vacuum conditions. In practical laser heating, these are not valid conditions, and the presence of surface contamination and oxide growth increase the spectral emissivity substantially in the infrared with little effect on it in the visible region [2]. Therefore in practical applications the differences in the emissivities is probably not as large as it appears in Table 2.1 [2]. Figure 2.4 illustrates the typical values of reflectivity of various surfaces at 10.6 μm . It is clearly evident that surface condition affects both the direct and diffuse reflectivities of steel, although increased surface roughness effects direct reflectivity to a lesser degree than diffuse. It is also clear that the oxidation of the steel has a more profound effect on the reflectivity than the surface conditions. The other materials shown in Figure 2.4 are often applied to materials to increase their absorbance of 10.6 μm radiation. Table 2.2 presents the absorbance of a variety of aerospace materials to CO_2 laser radiation.

The effects of surface roughness on the bidirectional reflectivity of nickel has been investigated by Birkebak et al [5]. Reflectivities of four rough specimens were tested using a beam incident 10° from the normal. The tests were performed at room temperature. The results are illustrated in Fig. 2.5. In this figure, the reflectivities of the rough surfaces are expressed as a ratio to the reflectivity of the polished samples. The reflectivity rises with increasing wavelength (due to the decrease in optical roughness [6]) and decreasing surface roughness. At 10.6 μm , the reflectivity for the 0.14 μm surface roughness is twice that of the samples roughened to 0.35 μm .

The effects of surface condition on the absorptivity of 304 stainless steel at 10.6 microns has been investigated by Wieting and DeRosa [7]. They found that when the samples were deformed by cold work (either metallurgical processing using 320 SiC or cold working in the case of the as received materials) the absorptivity at room temperature increases ~22-27%, due to increased scattering from non-planar defects at the surface [7]. When the samples were well annealed, the absorptivities of the highly polished surfaces are nearly the same as that of rougher surface over the range of temperatures 25 - 1000°C [7] as illustrated in Fig. 2.6. Though the surface prepared with 320 SiC has an initial absorptivity at room temperature that is ~27% higher than the highly polished surface, upon completion of the thermal cycle, the two absorptivities are

nearly coincident (Fig. 2.6). The tests were performed in vacuum so oxidation was not a factor. They also found that grain size did not effect the absorptivity of this material [7].

In studies performed by Duley [8] on clean metals surfaces under vacuum conditions (Figs. 2.7a through 2.7f), it was found that the simple temperature dependence exhibited by stainless steel and other metals is not followed by all metals. The metals Ti and Ta show a decrease in emissivity with increasing temperature, and Zr displays a complex $\epsilon(T)$ curve. Duley postulates that these effects may be attributable to the high-temperature annealing out of surface defects introduced during the preparation of the metal sheets used, citing the similar effect noted by Wieting and DeKosa [7] in their studies of 304 stainless steel.

In a study done by Mikino et al [9] it was found that for superalloys at room temperature, the reflectivities were also highest in the infrared. The emissivities for the superalloys were found to be higher than those of the pure metals. At longer wavelengths, the emissivity values were more than twice those of their constituent elements [9]. The variation of emissivity with wavelength is seen in Fig. 2.8. This figure also incorporates the data from earlier investigations by Wieting and Schriempf [10] on stainless steels. The results of Mikino are in good agreement with the previous results of Wieting. Makino's group also measured the reflectivity as a function of temperature. Since the tests were performed in deoxidized hydrogen, the effects of oxide growth were eliminated. The samples received no initial heat treatment and no initial oxide thickness is mentioned. In the tests as a function of temperature, it was found that the emissivity varied little with increasing temperature (Fig. 2.9).

As a material is heated, Bramson [11] found that the reflectivity is reduced by an amount that can be related to the materials temperature dependent electrical resistivity according to the equation

$$\epsilon(T) = 0.365 \left[\frac{\rho(T)}{\lambda} \right] - 0.667 \frac{\rho(T)}{\lambda} + 0.006 \left[\frac{\rho(T)}{\lambda} \right] \quad (2)$$

where

$\rho(T)$	=	Electrical Resistivity @ $T(^{\circ}\text{C})$
$\epsilon_{\lambda}(T)$	=	Emissivity @ $T(^{\circ}\text{C})$

λ = Wavelength of the Incident
Radiation (in μm)

For the CO_2 laser wavelength = $10.6 \mu\text{m}$, this expression becomes

$$\epsilon_{10.6 \mu\text{m}}(T) = 11.2[\rho_{20}(1+\alpha T)]^{1/2} - 62.9 [\rho_{20}(1+\gamma T)] + 174[\rho_{20}(1+\alpha T)]^{3/2} \quad (3)$$

where

ρ_{20} = Electrical Resistivity @ 20°C

τ = Coefficient of Resistivity Change
with Temperature

These equations can be used to obtain an estimate of the emissivity of "most simple metals over a moderate range of temperatures"[12]. Although superalloys are a complex mixture of various metals, and the resistivity data is for polished materials under vacuum conditions, these equations were used to estimate the emissivities of the various alloys. The results of these estimates are given in Tables 2.4, and graphically presented in Fig. 2.10.

Makino noted [9] that the resistivity is $\sim 1 \mu\Omega\text{m}$ in all of the alloys; from room temperature to the neighborhood of the melting range. The ratio of the resistivities at elevated temperatures to that at room temperature never exceeds 2; this is in contrast to the elements where the ratio often approaches 10.

The effects of oxidation on the emissivity of the superalloys and stainless steels will now be considered. Inconel 617 undergoes its fastest oxide growth at 850°C and 1000°C in the first five hours (Figs. 2.11 & 2.12) [15]. In performing the planned experiments for this study, it is not unreasonable that the samples may be exposed for this amount of time at this temperature. Consequently, the effects of oxidation on the reflectivity cannot be ignored.

The growth rate of NiO in pure nickel is very fast, never reaching steady state conditions [16]. The oxide scale is a crack free, macroscopically dense scale that exhibits uniform adhesion to the metal [16]. Inconel 617 develops a protective layer of Cr_2O_3 at relatively low temperatures and in a short period of time [17]. Inco Hx has been shown to develop a scale of $\text{Cr}_2\text{O}_3 + \text{NiCr}_2\text{O}_4 + \text{SiO}_2$ relatively quickly at low temperatures, that grows into a two layer scale at

higher temperatures for prolonged time. The external scale was found to be $\text{Cr}_2\text{O}_3 + \text{NiCr}_2\text{O}_4$ while the internal subscale was $\text{SiO}_2 + \text{NiCr}_2\text{O}_4$ [15].

The effects of oxidation on the normal spectral emissivity of Inconel X are shown in Fig. 2.13. The details of the oxide characteristics are not described [6], but oxidation has a substantial effect on the emissivity. At the longest common wavelength of the investigation ($\lambda = 2.6\mu\text{m}$), the oxidized alloy had an emissivity four times that of the polished material and three times that of the as received material.

The effects of oxidation on the emissivity of 304 stainless steel, molybdenum, and tantalum was investigated by Duley et al [18]. Oxidizing stainless steel for 1 minute at 1000°C doubles the emissivity compared to oxidation of the sample at 800°C for 1 minute (Fig. 2.14). The emissivity of molybdenum varies little in 20 minutes (the length of the experiment) when the oxidation is occurring at 500°C , yet the increase is dramatic (approximately twofold in 10 minutes) when the oxidation temperature is 600°C as illustrated in Fig. 2.15. At an oxidation temperature of 700°C , the emissivity reaches 1 within 3 minutes. For tantalum, again oxidation has little effect on the emissivity when the oxidation temperature is 500°C . At 600°C it increases fourfold in 5 minutes, and at 800°C the emissivity is shown to be greater than 1; an impossibility (Fig. 2.16). It is very clear that the effects of oxidation increase quite quickly above an oxidizing temperature of 500°C .

The complex refractive index of a metal

$$m = n - in' \quad (4)$$

may also be used to estimate the emissivity of a material. The complex refractive index exhibits common behavior for all metals at wavelengths $\geq 2\mu\text{m}$ [12]. Following Duley [12] we have

$$\epsilon_\lambda(T) = 1 - R_\lambda(T) = 1 - \frac{|m-1|^2}{|m+1|^2} \quad (5)$$

Using this equation for evaporated Ni films [19] with $m = 8.86 - 22.5i$ gives

$$\epsilon_\lambda(T) = 1 - R_\lambda(T) = 1 - \frac{|m-1|^2}{|m+1|^2}$$

$$\begin{aligned}
&= 1 - \frac{|(8.86 - 22.5i) - 1|^2}{|(8.86 - 22.5i) + 1|^2} \\
&= 1 - \frac{|(7.86 - 22.5i)|^2}{|(9.86 - 22.5i)|^2} \\
&= 1 - \frac{[(7.86)^2 + (-22.5)^2]^{1/2}}{[(9.86)^2 + (-22.5)^2]^{1/2}} \\
&= 1 - \frac{(23.833)^2}{(24.566)^2} = 1 - .9412 \\
&= .0588
\end{aligned}$$

Using this equation for Cr [20] with $m=15.3 - 23.5i$ gives

$$\begin{aligned}
\epsilon_\lambda(T) = 1 - R_\lambda(T) &= 1 - \frac{|m-1|^2}{|m+1|^2} \\
&= 1 - \frac{|(15.3 - 23.5i) - 1|^2}{|(15.3 - 23.5i) + 1|^2} \\
&= 1 - \frac{|(14.3 - 23.5i)|^2}{|(16.3 - 23.5i)|^2} \\
&= 1 - \frac{[(14.3)^2 + (-23.5)^2]^{1/2}}{[(16.3)^2 + (-23.5)^2]^{1/2}} \\
&= 1 - \frac{(27.51)^2}{(28.60)^2} = 1 - .9252 \\
&= .0748
\end{aligned}$$

Using this equation for SS 304 [20] with $m=16.0 - 18.6i$ gives

$$\begin{aligned}
\epsilon_\lambda(T) = 1 - R_\lambda(T) &= 1 - \frac{|m-1|^2}{|m+1|^2} \\
&= 1 - \frac{|(16.0 - 18.6i) - 1|^2}{|(16.0 - 18.6i) + 1|^2}
\end{aligned}$$

$$\begin{aligned}
&= 1 - \frac{|15.0 - 18.6i|^2}{|17.0 - 18.6i|^2} \\
&= 1 - \frac{|[(15)^2 + (-18.6)^2]^{1/2}|^2}{|[(17)^2 + (-18.6)^2]^{1/2}|^2} \\
&= 1 - \frac{(23.89)^2}{(25.20)^2} = 1 - .9480 \\
&= .0520
\end{aligned}$$

Using this equation for Cr_2O_3 [20] with $m=1.3 - .05i$ gives

$$\begin{aligned}
\epsilon_\lambda(T) = 1 - R_\lambda(T) &= 1 - \frac{|m-1|^2}{|m+1|^2} \\
&= 1 - \frac{|(1.3 - .05i) - 1|^2}{|(1.3 - .05i) + 1|^2} \\
&= 1 - \frac{|0.3 - .05i|^2}{|2.3 - .05i|^2} \\
&= 1 - \frac{|[(0.3)^2 + (-.05)^2]^{1/2}|^2}{|[(2.3)^2 + (-.05)^2]^{1/2}|^2} \\
&= 1 - \frac{(.304)^2}{(2.30)^2} = 1 - .0175 \\
&= .9825
\end{aligned}$$

Table 2.5 gives the complex refractive indices of additional materials.

The nature of the incident laser radiation is also important in studying the reflectivity of surfaces. At low power densities using a CW laser, typical reflection phenomena is to be expected. This is because there is not enough energy to melt the surface of the samples. Yet at high power densities, usually from pulsed CO_2 lasers, the reflectivity characteristics are much different. As the energy density increases the reflectivity decreases as is illustrated in Fig. 2.17. The reflectivity decreases dramatically when the beam intensity is sufficient to initiate a breakdown

plasma in the focal region [2]. This plasma aids in the absorption, transferring the resulting energy to the sample via hydrodynamic expansion [2]. In the region of the melting point, a well conducting metal can absorb much higher amounts of energy [21]. The importance of emissivity is diminished when material has been removed to the point where a cavity or keyhole has formed in the metal. At this point, the cavity acts as a blackbody absorber with the emissivity being effectively equal to one [2].

Duley has shown that the maximum surface temperature attainable with a stable uniform power source on a flat metal slab is given by [12]

$$T(r,z,t) = T(0,0,\infty) = \frac{P\alpha}{\pi r K}$$

where

r	= distance from the focal spot
z	= depth into the material
t	= time

and where

P	= Beam Power (Watts)
a	= fraction of energy absorbed
r	= radius of beam (cm)
K	= Thermal Conductivity (W/cm°C)

Consequently, since we will be using a fraction of the beam (70%), we have, using some typical values ($P = 25$ Watts, $\epsilon = \alpha = 0.6$, effective beam radius 0.33 cm, and appropriate values for K from Table 2.6):

For 304 Stainless Steel

$$T(0,0,\infty) = \frac{(.7)25 \text{ Watts } (.6)}{\pi(.33 \text{ cm})(.186)} = 54.45^\circ\text{C}$$

For Monel

$$T(0,0,\infty) = \frac{(.7)25 \text{ Watts } (.6)}{\pi(.33 \text{ cm})(.213)} = 47.55^\circ\text{C}$$

For Ni 200

$$T(0,0,\infty) = \frac{(.7)25 \text{ Watts } (.6)}{\pi(.33 \text{ cm})(.72)} = 14.07^\circ\text{C}$$

The amount of energy that needs to be absorbed to raise the temperature of a material is given by

$$Q_{in} = \text{Weight} \times \text{Specific Heat} \times (T_{final} - T_{orig}) \quad (5)$$

where

- Weight = Volume x density
- Specific heat = (BTU/lb°F) or (J/gm°C)
- T_{final} = 1000°C
- T_{orig} = 25 °C

$$\text{Volume} = \pi r^2 l = \pi (0.265)^2 (0.180) = 0.0397 \text{ in}^3$$

Using specific heats found in Table 2.7 we have:

For Incoloy 800 we have

$$\begin{aligned} \text{weight} &= 0.0397 \text{ in}^3 \times 0.290 \text{ lbs/in}^3 = 0.0115 \text{ lbs} \\ \text{specific heat} &= 0.12 \text{ BTU/lb}^\circ\text{F} \end{aligned}$$

$$Q_{in} = \frac{0.115 \text{ lbs}}{1} \left| \frac{0.12 \text{ BTU}}{\text{lb}^\circ\text{F}} \right| \left| \frac{1 \text{ W} \cdot \text{hr}}{3.412 \text{ BTU}} \right| \frac{1725^\circ\text{F}}{1}$$

$$Q_{in} = 0.6977 \text{ W hrs}$$

For Inconel 600 we have

$$\begin{aligned} \text{weight} &= 0.0397 \text{ in}^3 \times 0.304 \text{ lbs/in}^3 = 0.0121 \text{ lbs} \\ \text{specific heat} &= 0.11 \text{ BTU/lb}^\circ\text{F} \end{aligned}$$

$$Q_{in} = \frac{0.121 \text{ lbs}}{1} \left| \frac{0.11 \text{ BTU}}{\text{lb}^\circ\text{F}} \right| \left| \frac{1 \text{ W} \cdot \text{hr}}{3.412 \text{ BTU}} \right| \frac{1725^\circ\text{F}}{1}$$

$$Q_{in} = 0.6729 \text{ W hrs}$$

For 304 Stainless we have

$$\begin{aligned} \text{weight} &= 0.0397 \text{ in}^3 \times 0.289 \text{ lbs/in}^3 = 0.0115 \text{ lbs} \\ \text{specific heat} &= 0.12 \text{ BTU/lb}^\circ\text{F} \end{aligned}$$

$$Q_{in} = \frac{0.0115 \text{ lbs}}{1} \left| \frac{0.12 \text{ BTU}}{\text{lb}^\circ\text{F}} \right| \left| \frac{1 \text{ W} \cdot \text{hr}}{3.412 \text{ BTU}} \right| \frac{1725^\circ\text{F}}{1}$$

$$Q_{in} = 0.6977 \text{ W hrs}$$

For Monel 400 we have

$$\begin{aligned} \text{weight} &= 0.0397 \text{ in}^3 \times 0.319 \text{ lbs/in}^3 = 0.0127 \text{ lbs} \\ \text{specific heat} &= 0.11 \text{ BTU/lb}^\circ\text{F} \end{aligned}$$

$$Q_{in} = \frac{0.0127 \text{ lbs}}{1} \left| \frac{0.11 \text{ BTU}}{\text{lb} \cdot ^\circ\text{F}} \right| \left| \frac{1 \text{ W} \cdot \text{hr}}{3.412 \text{ BTU}} \right| \frac{1725 \cdot ^\circ\text{F}}{1}$$

$$Q_{in} = 0.7063 \text{ W hrs}$$

For Nickel 200 we have

$$\text{weight} = 0.0397 \text{ in}^3 \times 0.321 \text{ lbs/in}^3 = 0.0127$$

$$\text{specific heat} = 0.11 \text{ BTU/lb}^\circ\text{F}$$

$$Q_{in} = \frac{0.0127 \text{ lbs}}{1} \left| \frac{0.11 \text{ BTU}}{\text{lb} \cdot ^\circ\text{F}} \right| \left| \frac{1 \text{ W} \cdot \text{hr}}{3.412 \text{ BTU}} \right| \frac{1725 \cdot ^\circ\text{F}}{1}$$

$$Q_{in} = 0.7063 \text{ W hrs}$$

2.3. Experimental Approach and Equipment

2.3.1. Objective

The objective of this investigation is to measure the emissivity at 10.6 μm (the nominal output wavelength of a CO_2 laser) for various superalloys as a function of temperature and angle of incidence. The primary intent is to measure this material parameter for the materials under practical conditions (i.e. the surface conditions are as received, and the measurements are made in air). In doing this, the effects of oxidation cannot be ignored. If, in the course of doing the investigation, the reflectivity is found to deteriorate with time representing oxide growth, it may become necessary to heat treat and pre-oxidize the materials to a point where oxide growth within the time frame of the experiment is not a factor. This is one of the aspects the investigation will be concentrating on.

2.3.2. Materials

The materials to be tested are as follows:

- 1) Monel alloy 400
- 2) Inconel 617
- 3) Inconel 718
- 4) Incoloy 800
- 5) Inco Alloy HX
- 6) 316 Stainless Steel
- 7) Nickel (pure)

8) Inconel 600

The compositions (in weight %) of these alloys is given in Table 2.8; and the densities and melting points are presented in Table 2.9.

The sample dimensions are given in Appendix A - Drawing 1.

All of the samples listed above (except 316 SS) were provided courtesy of Inco Alloys International. The eight other companies that were contacted with the same request all gave negative responses.

2.3.3. Experimental Approach

The experimental apparatus is schematically illustrated in Fig. 2.18. The radiation source is a CO₂ laser with a nominal output power of ~30W. In practice, it is desirable to operate the laser at lower powers to minimize the hazards. As the beam leaves the lasing tube, it enters a plexiglass containment box. The beam passes through a chopper and then through a beam diameter limiter of 6 - 7 mm. In order to determine the reflectivity, it is necessary to know the power of the beam that strikes the sample of interest. If the laser power is reproducible each time the laser is employed, a calibration of output power vs. high voltage potential (or milliamperes of current) will be developed. This will allow the specimen holder to be rigidly mounted upon the stage and will minimize the continuous alignment procedure that will be necessary if the output is not stable. If the output of this laser fluctuates with each use, a system employing a different specimen stage will be necessary. This second stage will have to employ an additional mirror mounted 180° away from the sample. When the beam passes through the chopper, it bounces off the mirror providing knowledge of the original power that will strike the sample. A firebrick will then be inserted in the laser path while the mirror and specimen are rotated 180°. The firebrick is then removed, allowing the beam to strike the sample and reflect to the detector. The reflectivity is calculated by $\text{Power(Reflected)}/\text{Power(Incident)}$. Obviously, a reproducible stable output will make the procedure much simpler, minimizing the number of alignments necessary at each stage.

The samples will be tested in the temperature range 25 - 1000°C. Heating will be done using a radiant, half cylinder, electrical resistive heater manufactured by Thermcraft, Inc. It was

determined that the desired high temperatures, which necessitated the fabrication of the stage described above, could only be achieved by placing this type of heater above the sample holder. It is to be supported by Grade A lava stone. The original design of placing a firerod cartridge heater within the Inconel sample holder had to be rejected because the maximum working sheath temperature currently being manufactured (by GE) is 1500°F (=816°C), not sufficiently high enough for this study. The radiation losses as the sample is heated and as the emissivity changes (presumably due to oxide growth) are displayed in Table 2.10.

1.3.4. Experimental Equipment

1) CO Laser -

When the laser was received from Wright-Patterson, it was received in a damaged condition (Fig. 2.19). Consequently, it was repaired in the ASU glass shop. The laser itself has a nominal power potential of ~30 watts and has been assigned a value of \$3000 [22]. In practice, it would be desirable to operate the laser at less than full power. The equipment is pictured in Fig. 2.20. The relevant dimensions for the laser output point are detailed in Appendix A - Drawings 2 & 3. Cables rated for 40 kV have been fabricated to connect the tube to the HV power supply.

2) High Voltage Power Supply -

The laser requires >12,000 V to initiate lasing. Its operating parameters are closer to 8 KV and ~8 - 18 milliamps. A preexisting power supply was cleaned and upgraded from 10 KV to supply ~12 KV, thus providing enough power to initiate lasing. Output voltage is monitored via a calibrated meter up to 10 KV. Associated wall wiring has also been completed.

3) Current Monitoring -

This will be accomplished via a milliamper meter that will be wired in series just prior to the high voltage connections to the laser tube. The meters located on the high voltage power supply itself are useless since their range is hundreds of milliamps and the laser has a maximum current of 15 - 20 milliamps. There is also a 10 kΩ resistor box supplied by WPAFB to be hooked in series between the power supply and the laser tube.

4) Gas Flow Control-

A mechanical pump will be used to maintain gas flow parameters. The laser tube and associated gas flow equipment will be tested as soon as a vent can be installed in 334 ERC (see 2.3.5). The gas flow control system located just prior to the mechanical pump has been completed and leak tested to a pressure of 30 millitorr = 0.030 torr, sufficient for our purpose since the laser operates at an absolute pressure of 5-8 torr.

An absolute pressure gauge (Leybold-Heraeus - Model #16063-T) has been purchased. A mounting box has been constructed to house the gauge.

5) Cooling System -

Cooling of the discharge tube will be accomplished the following way. The cooling system is a closed system consisting of a 1/200 hp in line pump (Little Giant model 1-42A) connected to a 6-1/2 gallon plastic storage tank. High quality deionized water will be recirculated through the closed system. If further cooling is necessary it is possible to install in line a small heat exchanger, although this is not believed to be necessary. In order to lower the output of the laser, the cooling of the tube may be lessened [22]. The flow rate will be controlled by varying the head to which the water must be pumped.

6) Alignment Equipment -

A table has been constructed (5 feet x 4 feet) to hold the detection equipment. This will be connected to the lab table where the laser rests.

A 3 feet x 4 feet optical workboard (Newport Corporation - Model LS-34) has been purchased.

Equipment for alignment of sample and detection equipment has been purchased. This consists of a Thermal Image Plate, a beam probe, and a UV lamp, all from Optical Engineering Corporation.

7) Detection Equipment -

A pyroelectric detection system has been purchased to detect the laser radiation. The system consists of radiometer (Model RL-3610), a probe with a detector area equal to 1 cm^2 (Model RkP-360), a remote 30 Hz chopper, and a reflective attenuator which extends the range of the RkP-360 probe from 10 watts to approximately 100 watts. All detection equipment was purchased from Laser Precision Corp. This system was chosen because, with the chopper, the effects of background signal noise can be almost totally eliminated; the power meter only responds to the radiation that is being chopped.

8) Sample Stage -

The sample stage was constructed at ASU from high temperature alloys (Stainless steels, Inconels) except for the base which is made from Al. The dimensions and materials are detailed in Appendix A - Drawings 4 through 7. In this stage, the sample maintains a sliding fit with the heater sheath so that the surface of the sample is co-axial with the rotation base. The sheath itself is bolted to a horizontal positioner through an insulating nest made from Grade A Lava stone that is connected to the rotation base through a piece of heat insulating ceramic.

2.3.5. Safety Considerations

1) An interlock system has been installed in ERC 334. It is hooked up to the west side door and to the plexiglass containment box and wired into the high voltage power supply. The east door will not have an interlock but is shielded from the investigation area by a series of bookcases. This will facilitate easy entry for the four other graduate students who share the same lab.

2) A key lock has been installed on the high voltage power supply.

3) A 1/2 inch thick plexiglass beam containment box has been fabricated. Blueprints for this box are found in Appendix A - Drawings 8 through 10. The containment box covers the entire optical workboard and has one entry port for the beam. It will also be connected to the interlock system.

4) High voltage safety shields have been fabricated from plexiglass for the laser tube electrodes.

5) A plexiglass safety box has been constructed to house milliammeter.

6) Safety glasses for 10.6 micron radiation have been ordered from Frank Reed Optical. Three high quality, expensive pair for people who may work with the laser at length, two plexiglass pair for casual visitors.

7) Appropriate safety signs will be purchased for placement at all points of entry.

2.3.6. Future Considerations

1) Leaks have been detected on the laser tube where the electrodes enter. It is believed that "epoxy patch" manufactured by the Hi-Sol division of Dexter Corp. (chemically identical to Varian's "Torr Seal") will sufficiently seal these leaks to continue.

2) The gas flow system will have to undergo a final leak test with the mechanical pump in place and all auxiliary equipment connected.

3) The laser gas must be purchased. This will be 1:2:3 gas of CO_2 , N_2 , He.

4) A hand held Tesla coil should be purchased.

5) The laser must be aligned.

2.4. Conclusions

The spectral emissivity of a material is a basic material property. This property is not well known for superalloys under practical conditions for the wavelength of interest (i.e. 10.6 microns). It is the intent of this study to determine this material parameter under practical "in-use" conditions. The studies will present the spectral emissivity for the superalloys as a function of temperature (25 - 1000°C) as well as angle of incident radiation. The results of oxidation on the reflectivity will also be a large part of the study.

References

- 1) Everhart, J. L., *Engineering Properties of Ni and Ni Alloys*, Plenum Press, New York, 1971.
- 2) Duley, W. W., *Laser Processing and Analysis of Materials*, Plenum Press, New York, 1983.
- 3) Steen, W.M., "Surface Engineering With Lasers", *Applied Laser Tooling*, Ed. by Soares, O.D.D. & Perez-Amor, M., Martinus Nijhoff Pub., Dordrecht, 1987, p.137
- 4) Sona, A., "Metallic Materials Processing: Cutting and Drilling", *Applied Laser Tooling*, Ed. by Soares, O.D.D. & Perez-Amor, M., Martinus Nijhoff Pub., Dordrecht, 1987, p.109
- 5) Birkebak, R.C. and E.R.G. Eckert, *J Heat Transfer*, Vol. 87, No. 1, 1965, pp. 85-94.
- 6) Siegel, R. and Howell, J.R., *Thermal Radiation Heat Transfer*, 2nd ed., Hemisphere Publishing Corp., Washington, 1981, p.131.
- 7) Wieting, T.J. and DeRosa, J.L., *J. Appl. Phys.*, 50[2], 1979, pp. 1071 - 1078.
- 8) Duley, W.W., "Laser Material Interactions of Relevance to Metal Surface Treatment", in *Laser Surface Treatment Of Metals, NATO ASI Series (Series E: Applied Sciences - No. 115)*, Ed. by Draper C.W., and Massoldi P., Martinus Nijhoff Publishers, Dordrecht, 1986, pp. 3-17.
- 9) Makino, T., Kunitomo, T., Mori, T., *Bulletin of JSME*, vol. 27, no. 223, Jan. 1984.
- 10) Wieting, T.J. and Schriempf, J.R., *J. Appl. Phys.*, 47[9], 1976, pp. 4009-4011.
- 11) Bramson, M.A., *Infrared Radiation: A Handbook of Applications*, Plenum Press, New York, 1968.
- 12) Duley, W. W., *CO2 Lasers: Effects and Applications*, Academic Press, New York, 1976, pp. 136-137.
- 13) *Handbook of Tables for Applied Science Engineering*, 1973.
- 14) *Metals Reference Handbook*, Smithells (ed.), 5th Ed., 1978.
- 15) Christ, H.J., Berchtold, L., Sockel, H.G., *Oxid. of Met.*, 26[1-2], 1986, pp.45-76.
- 16) Wasielewski, G.E., Rapp, R.A., *The Superalloys*, Chap.10, Ed. by Sims, C., Hagel, W., John Wiley & Sons, 1972
- 17) Smialek, J.L., Meier, G.H., *The Superalloys II*, Chap.11, Ed. by Sims, C., Stoloff, N., Hagel, W., John Wiley & Sons, 1987
- 18) Duley, W. W., Semple, D.J., Morency, J.P., and Gravel, M., *Opt. Laser Technol.*, [11], 1979, p. 281.
- 19) Ozisik, M.N., *Radiative Transfer and Interactions With Conduction and Convection*, 1973, p.89.

- 20) Ohno, J., Abe, S., and Kobayashi, H., Japan Journal of Applied Physics, 26(7), July 1987 pp.1056-63
- 21) Koebner, H. (Ed.), *Industrial Applications of Lasers*, John Wiley & Sons, Chichester, 1984, p. 83.
- 22) Telephone correspondence with Alan Gascarden (WPAFB).

Table 2.1. Values of Emissivity for Various Metals at Laser Wavelengths (Ref. 2)

Metal	Emissivity ^a			
	Ar ⁺ (500 nm)	Ruby (700 nm)	Nd-YAG (1000 nm)	CO ₂ (10 μm)
Aluminum	0.09	0.11	0.08	0.019
Copper	0.56	0.17	0.10	0.015
Gold	0.58	0.07	—	0.017
Iridium	0.36	0.30	0.22	—
Iron	0.68	0.64	—	0.035
Lead	0.38	0.35	0.16	0.045
Molybdenum	0.48	0.48	0.40	0.027
Nickel	0.40	0.32	0.26	0.03
Niobium	0.58	0.50	0.32	0.036
Platinum	0.21	0.15	0.11	0.036
Rhenium	0.47	0.44	0.28	—
Silver	0.05	0.04	0.04	0.014
Tantalum	0.65	0.50	0.18	0.044
Tin	0.20	0.18	0.19	0.034
Titanium	0.48	0.45	0.42	0.08
Tungsten	0.55	0.50	0.41	0.026
Zinc	—	—	0.16	0.027

^aAt 20°C

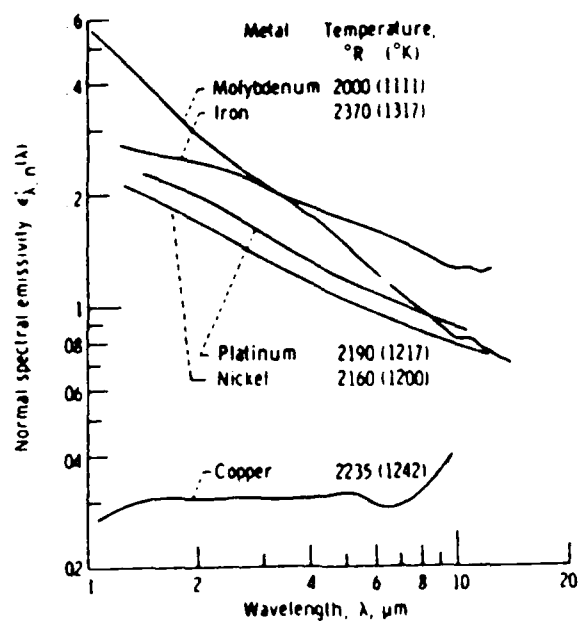


Fig. 2.1 Variation With Wavelength of Normal Spectral Emissivity for Polished Metals (Ref. 6)

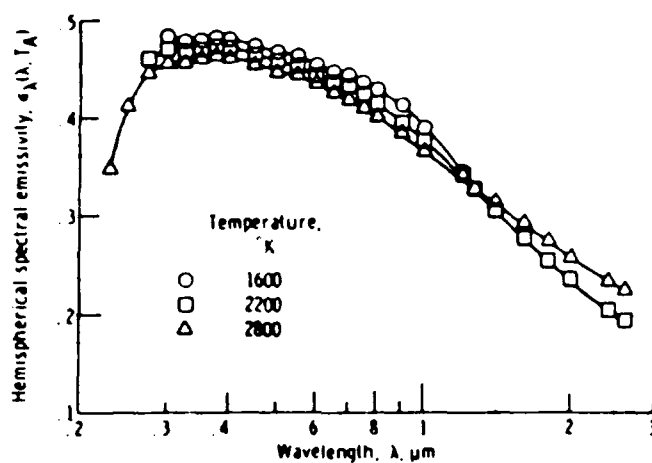


Fig. 2.2. Effect of Wavelength and Surface Temperature on Hemispherical Spectral Emissivity of Tungsten (Ref. 6)

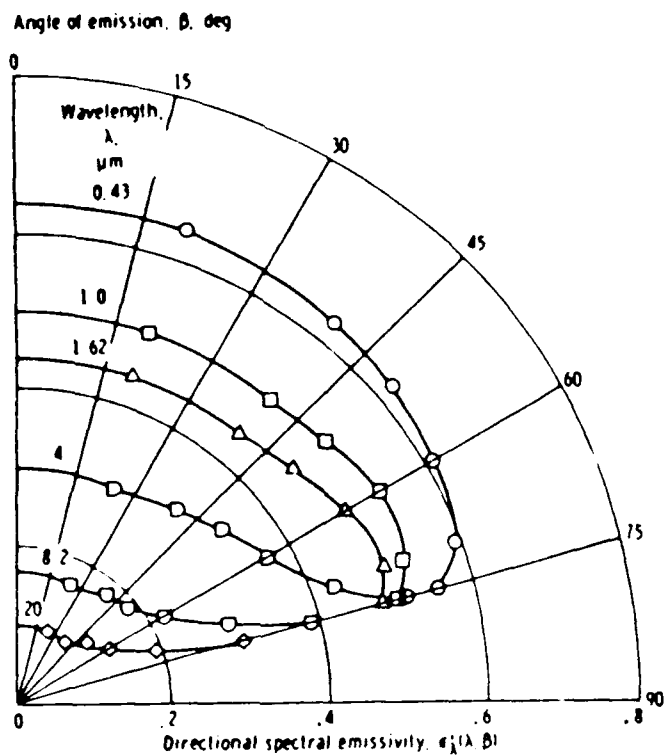


Fig. 2.3. Effect of Wavelength on Directional Spectral Emissivity of Pure Titanium. Surface Ground to $0.4\mu\text{m}$ (Ref. 6)

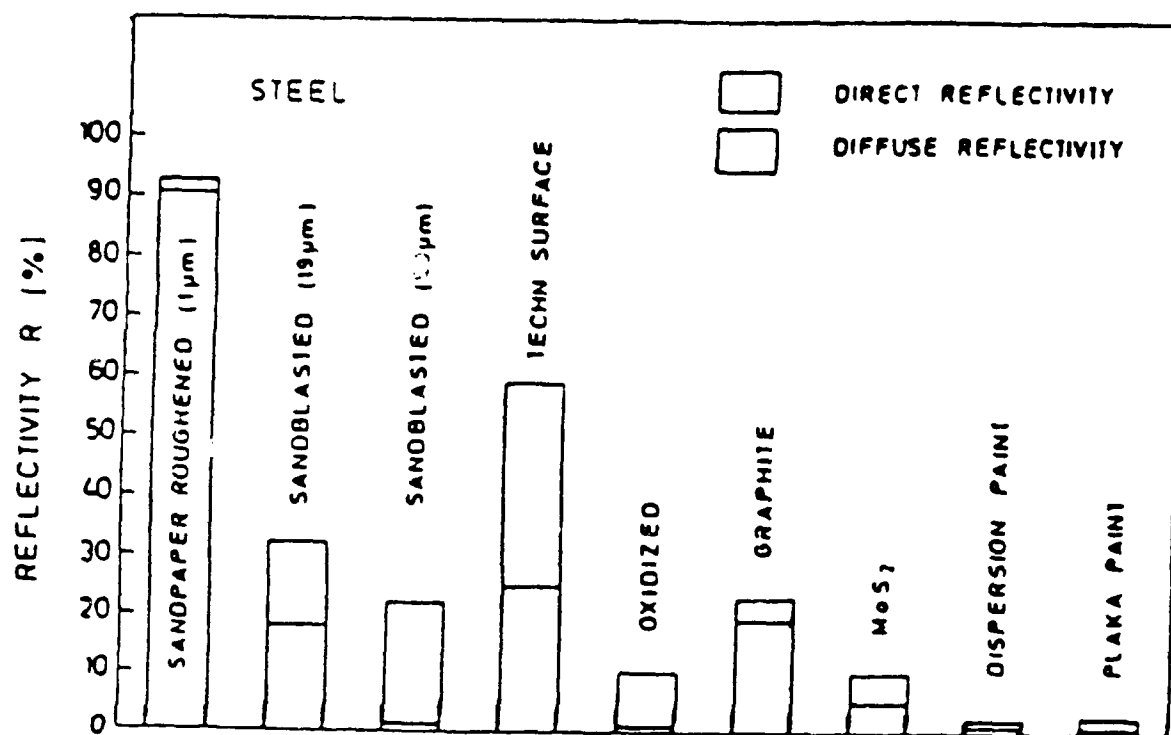


Fig. 2.4. Typical Values of Reflectivity For Various Surfaces to 10.6 μm radiation at Normal Angles of Incidence (Ref. 3)

Table 2.2: Room Temperature Absorptances of Aerospace Metals And Alloys @ 10.6 μm for Various Surface Conditions and @ Normal Incidence (Ref.4).

Room Temperature Absorptances of Aerospace Metals and Alloys @ 10.6 μm for Various Surface Conditions and @ Normal Incidence				
Metal of Alloy	Ideal	Surface Condition Polished	As Received	Sand-blased
Al	0.013	0.030	0.04 ± 0.02	0.115 ± 0.015
Au	0.006	0.010	0.02	0.14
Cu	0.011	0.016		0.06
Ag	0.005	0.011		
2024 Al		0.033	0.07 ± 0.02	0.25
304 Stainless Steel		0.110	0.40 ± 0.20	
Ti Alloy (6 Al, 4 V)			0.65 ± 0.20	
Mg alloy AZ-31B			0.06 ± 0.03	

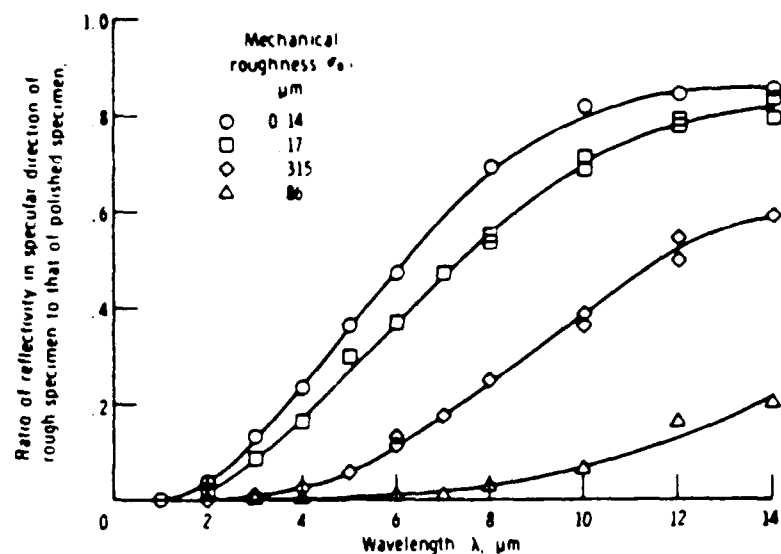


Fig. 2.5. Effect of Roughness on Bidirectional Reflectivity in Specular Direction from Ground Ni Specimens, (Mech. Roughness of Polished Specimen is $0.015 \mu\text{m}$) (Ref. 6)

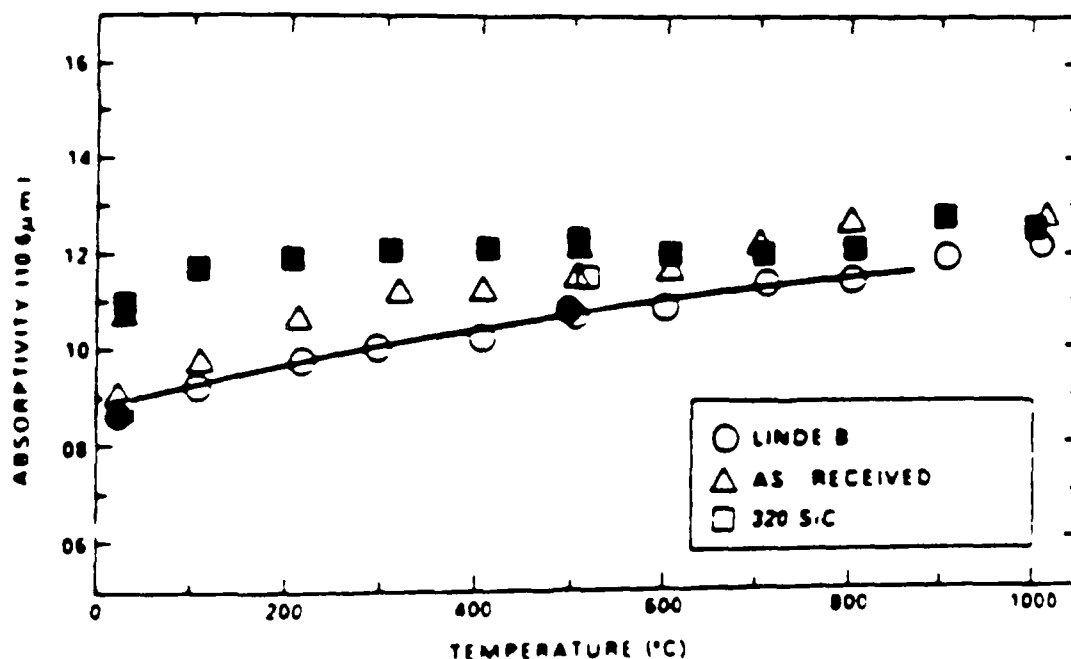
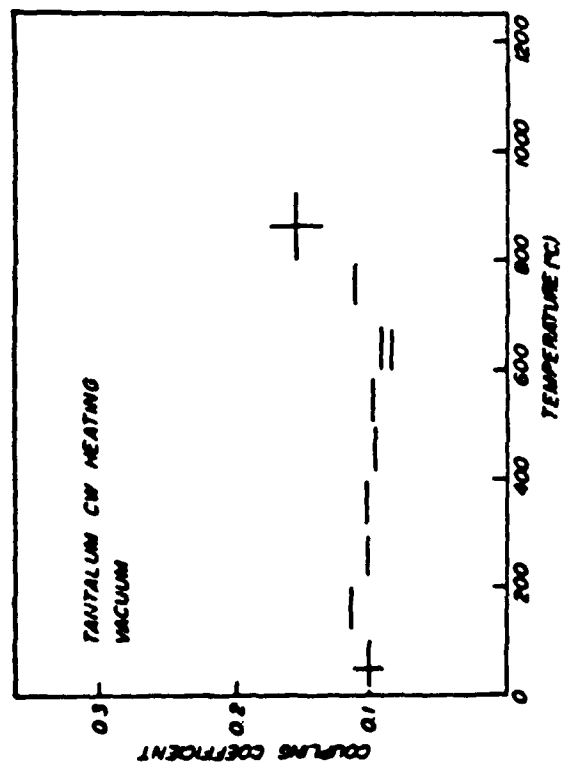
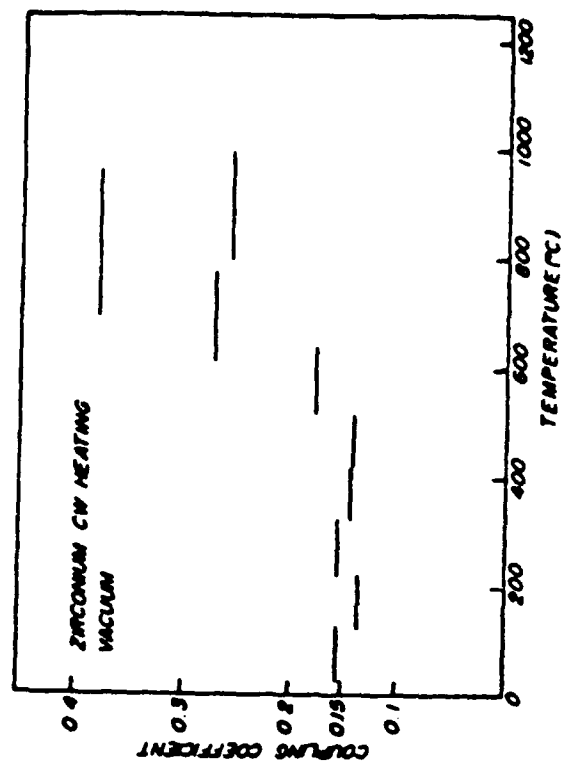


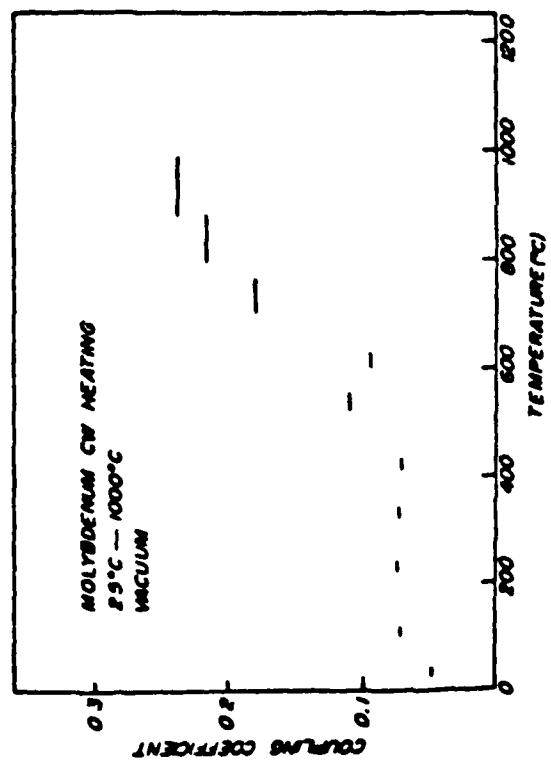
Fig. 2.6 Absorptivity of 304 stainless steel at $10.6 \mu\text{m}$ as a function of temperature and surface condition. The black dot points were obtained while increasing the furnace temperature from 25 to 1000°C , the other data points marks the return half of the temperature cycle. Each point represents an average of between two and four measurements (Ref. 7).



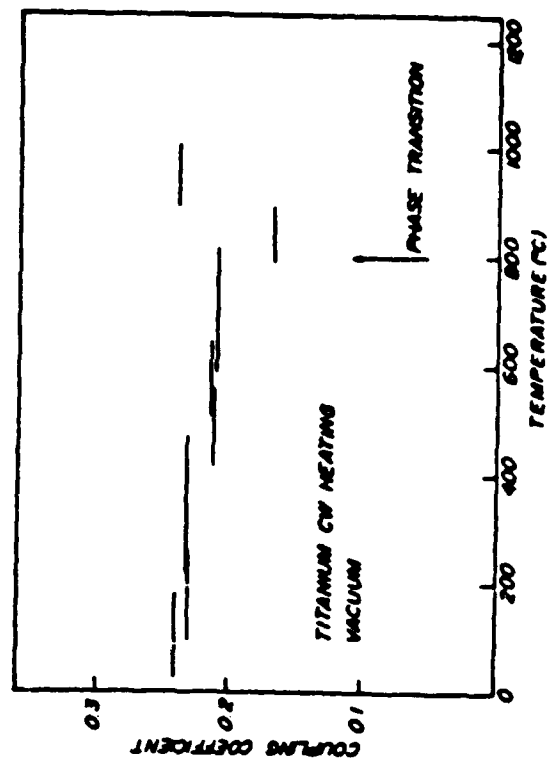
a: A (10.6 μm) vs. T for tantalum.



b: A (10.6 μm) vs. T for zirconium.

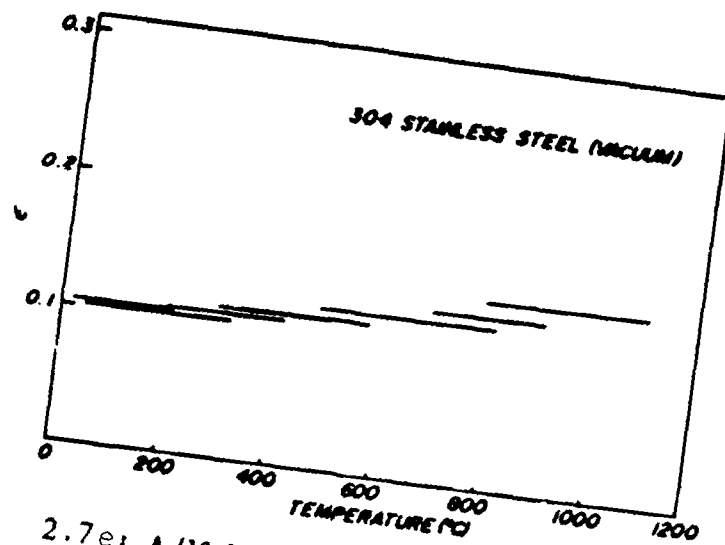


c: A (10.6 μm) vs. T for molybdenum.

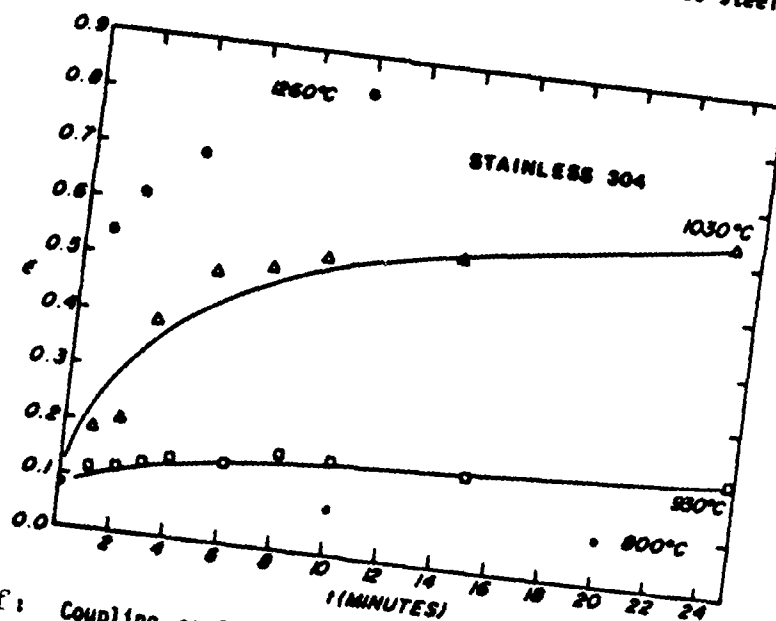


d: A (10.6 μm) vs. T for titanium.

Fig. 2.7 (a-d): Emissivities of Selected Elements @ 10.6 μm (Ref. 8).



2.7e: ϵ ($10.6 \mu\text{m}$) vs. T for 304 stainless steel.



2.7f: Coupling coefficient $\epsilon (\equiv A)$ for cw CO_2 radiation incident on 304 stainless steel oxidized for various times at indicated temperatures. A theoretical fit using Eq.(12) is shown for two data sets.

Fig. 2.7 (e-f): Emissivities of Stainless Steels @ $10.6 \mu\text{m}$ (Ref. 8).

Table 2.3. Chemical Compositions of Specimens (Figs. 8 & 9) (wt %)

	Pu	Si	Co	Cr	C	Al	Mn	
a. JIS SUS 304	Bal.	0.76	-	18.04	0.052	0.94	1.04	
b. JIS SUS 316	Bal.	10.28	-	16.68	0.074	0.75	1.07	2.11Mo
c. Incoloy 800	45.87	31.23	-	21.04	0.059	0.33	0.77	0.42Ti, 0.51Al
d. Hastelloy X	18.32	Bal.	0.99	21.34	0.068	0.46	0.56	0.90Mo, 0.51W
e. Inconel 600	9.86	75.65	-	14.30	0.035	0.38	0.31	
f. Inconel 617	0.20	Bal.	12.4	22.09	0.073	0.20	0.040	0.88Mo, 0.35Ti, 0.04Al
g. X-40	0.26	10.07	Bal.	25.14	0.52	0.54	0.037	7.36W

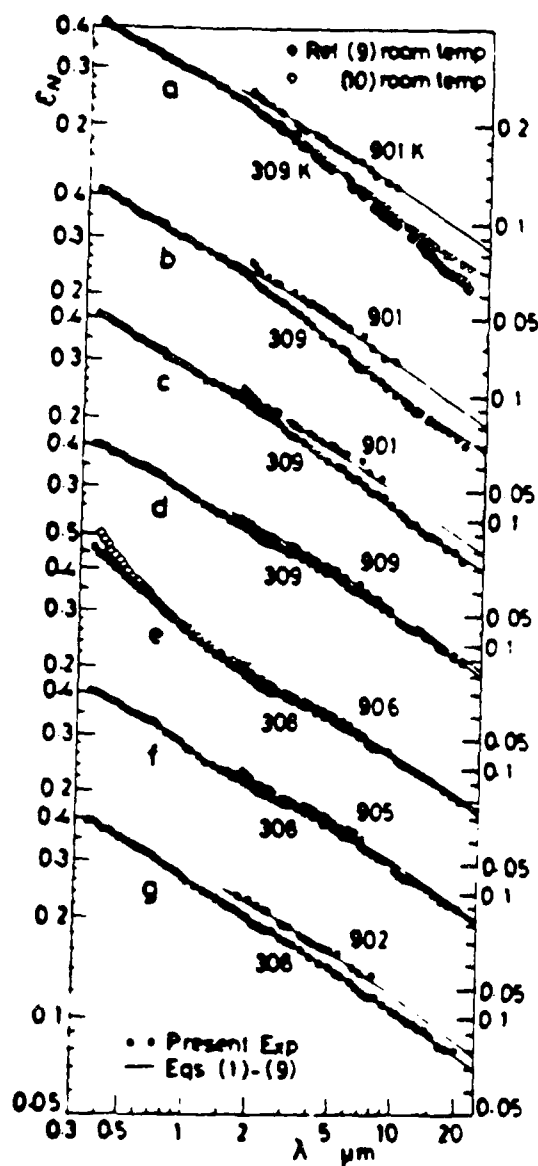


Fig. 2.8. Spectra of Normal Emissivity (Ref. 9)

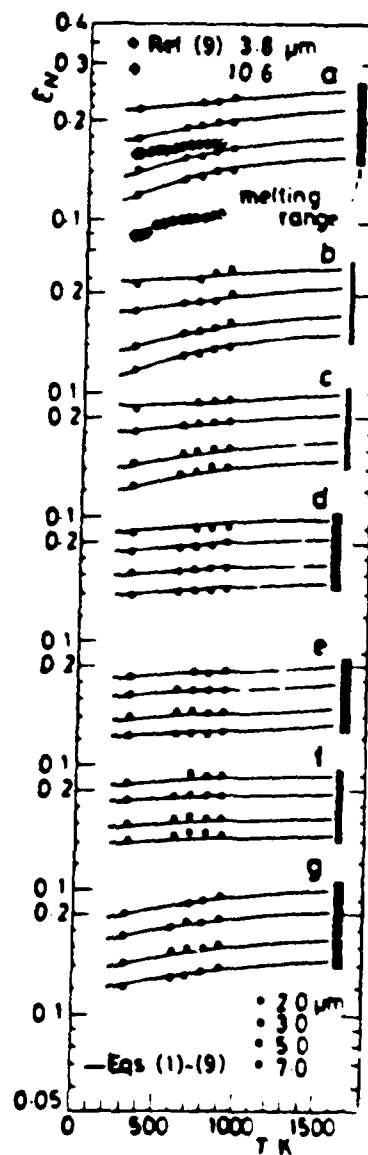


Fig. 2.9. Temperature Dependence of Normal Emissivity (Ref. 9)

Table 2.4: Resistivities of Sample Alloys

Physical Properties of Alloys In Vacuum @ Normal Incidence					
Property / Alloy	Temp (°C)	Resistivity (Ω-cm)	$\epsilon_{10.6\mu}$	$R_{10.6\mu}$	τ
Ni 200**	@ 20°C	7×10^{-6}	.0292	.9708	.006
	@ 227°C		.0445	.9555	
	@ 477°C		.0566	.9434	
	@ 727°C		.0663	.9337	
	@ 977°C		.0747	.9253	
Monel 400 Monel **	@ 20°C	42×10^{-6}	.070	.930	.002
	@ 227°C		.0838	.9162	
	@ 477°C		.0964	.9036	
	@ 727°C		.1074	.8926	
	@ 977°C		.1172	.8828	
Inconel 600	@ 227°C	113×10^{-6}	.1123	.8877	
	@ 477°C	117.5×10^{-6}	.1144	.8856	
	@ 727°C	117.5×10^{-6}	.1144	.8856	
	@ 977°C	121×10^{-6}	.1159	.8841	
Inconel 617	@ 227°C	127×10^{-6}	.1186	.8814	
	@ 477°C	130×10^{-6}	.1199	.8801	
	@ 727°C	130×10^{-6}	.1199	.8801	
	@ 977°C	130×10^{-6}	.1199	.8801	
Inconel 718					
Incoloy 800 !!	@ 227°C	110×10^{-6}	.1109	.8891	
	@ 477°C	125×10^{-6}	.1177	.8823	
	@ 727°C	130×10^{-6}	.1199	.8801	
	@ 977°C	137×10^{-6}	.1229	.8771	
++ !! Inco HX (Hastalloy X)	@ 0°C	113.8×10^{-6}	.1126	.8874	
	@ 227°C	121×10^{-6}	.1159	.8841	
	@ 477°C	128×10^{-6}	.1190	.8810	
	@ 727°C	130×10^{-6}	.1199	.8801	
	@ 977°C	132×10^{-6}	.1208	.8792	

!! Ref. 9

** Ref. 13

++ Ref. 14

Emissivity vs. Temp

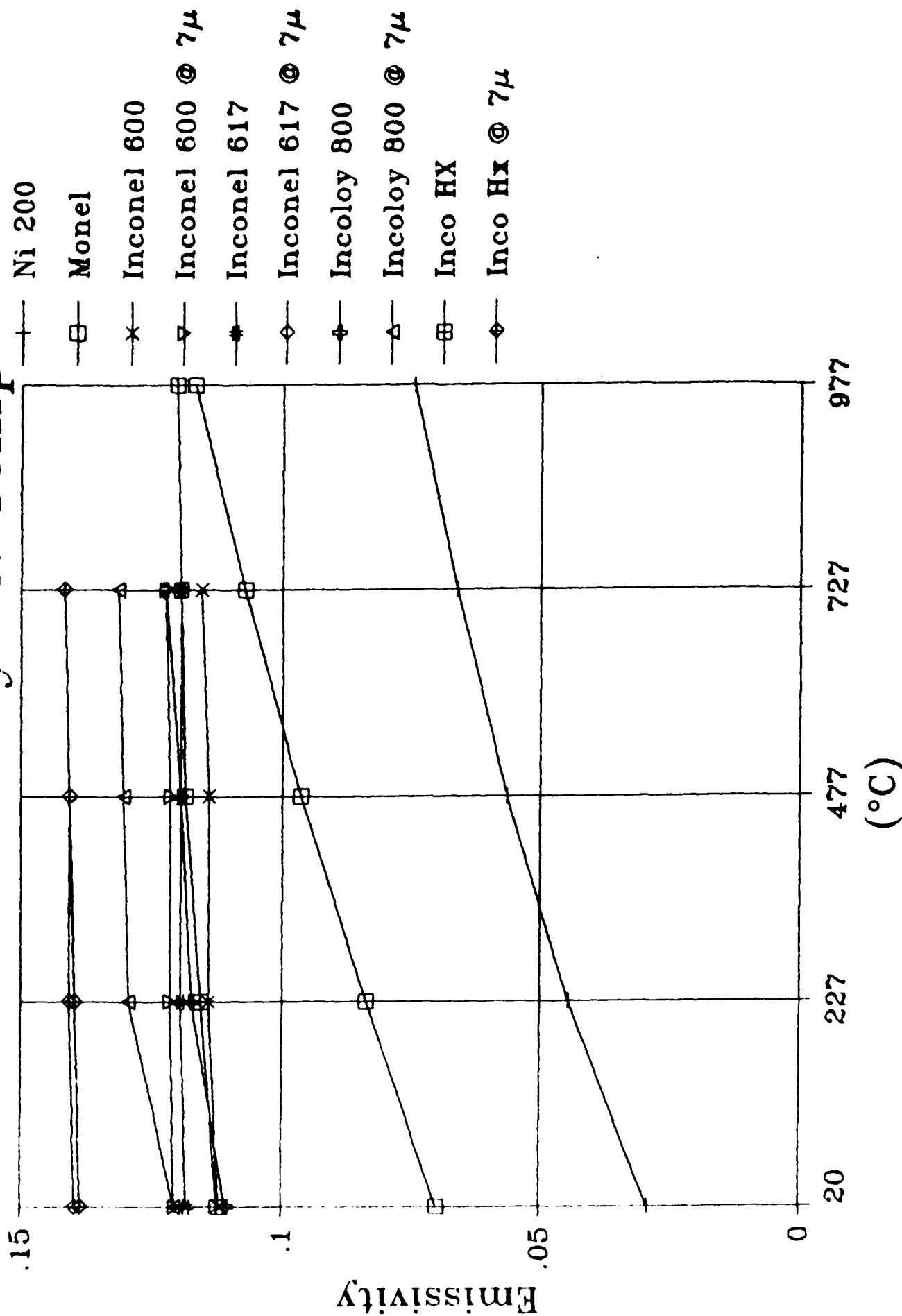


Fig. 2.10. Plot of Emissivity vs. Temperature (°C) Corresponding to Calculated Values From Table 2.4.

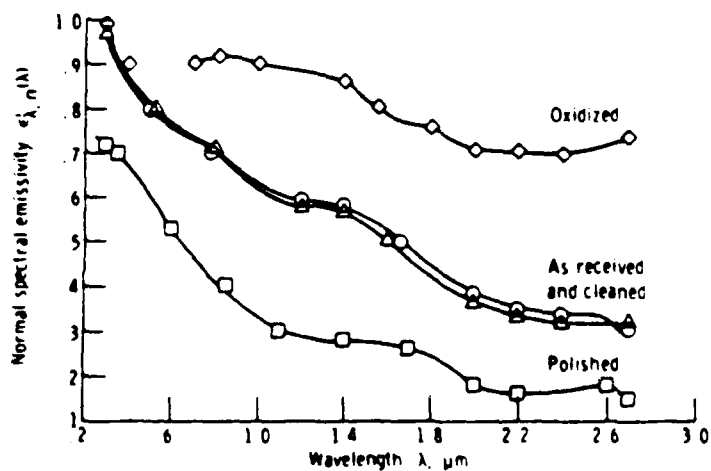
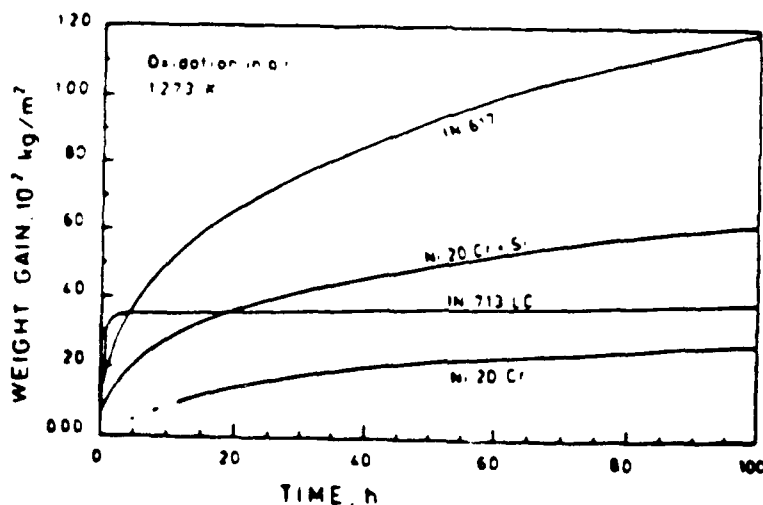
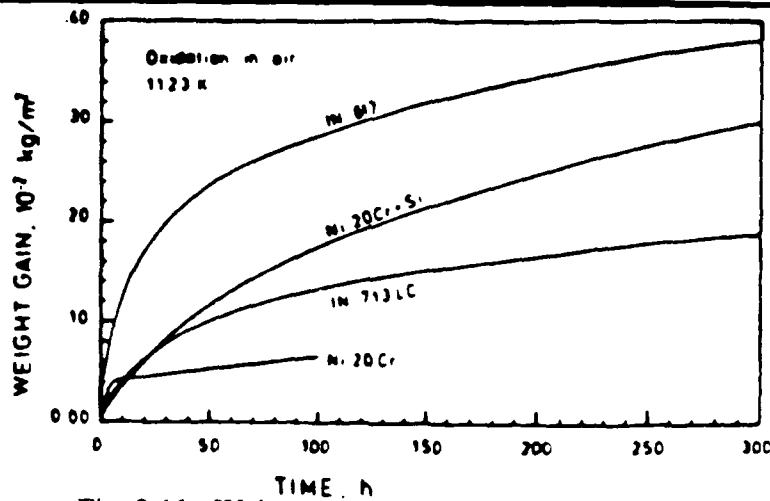


Table 2.5: Complex Indices of Refraction of Absorbing Materials @ Ordinary Temperature (Ref. 19)

Complex Indices of Refraction, $m = n - in'$, of Absorbing Materials at Ordinary Temperature

Substance	λ, μ	n	n'	Substance	λ, μ	n	n'
Aluminum ^a (evap.)	0.22	0.14	2.35	Nickel ^a (evap.)	1.12	2.63	4.28
	0.4	0.40	4.45		2.0	3.74	8.80
	0.9	1.96	7.7		4.4	4.35	10.59
	2.0	2.3	16.5		6.75	5.86	15.2
	6.0	10.8	42.6		10.5	8.86	22.5
	10.0	26.0	67.3	Silver ^a (evap.)	0.3	1.2	0.8
Copper ^a (evap.)	0.5	2.42	0.88		0.6	0.060	3.75
	1.0	6.27	0.197		1.0	0.129	6.83
	5.0	27.45	2.92		4.0	1.89	28.7
	10.25	60.6	11.0		10.0	10.69	69.0
Germanium ^a (evap.)	0.4	2.3	2.8	Silver ^a (bulk)	0.316	1.13	0.43
	1.0	5.1	0.45		0.500	0.17	2.94
	2.0	4.35	0.03		0.589	0.18	3.94
	5.0	4.3		Silver ^a (chemically deposited)	0.75	0.17	5.16
Gold ^a (evap.)	10.0	4.3			1.00	0.24	6.96
	0.2	1.24	0.92		1.50	0.45	10.7
	0.5	0.84	1.84		4.37	4.34	32.6
	1.0	0.179	6.04	Sodium ^a (vacuum deposited)	0.254	0.026	0.621
	1.95	1.3	10.7		0.365	0.042	1.44
	6.65	12.9	35.5	Tungsten ^a (bulk)	0.579	2.76	2.71
Iron ^b	9.9	25.2	55.9		0.589	3.46	3.25
	0.441	2.66	3.84	Water ^d (liquid)	0.45	1.34	0.0
	0.559	3.46	3.88		0.70	1.33	0.0
Iron ^a (bulk)	0.668	3.57	4.03		1.61	1.315	0.0
	0.589	2.36	3.20		2.25	1.290	0.0
	0.441	1.28	1.37		3.90	1.353	0.0059
Mercury ^a (liquid)	0.589	1.51	1.63		5.30	1.315	0.0143
	0.668	1.70	1.84		8.15	1.29	0.0472
	0.4	0.73	3.01		10.00	1.212	0.0601
Zinc ^a	0.6	1.39	4.39		0.257	0.554	0.612
	0.8	2.14	5.33		0.361	0.720	2.610
					0.468	1.049	3.485
					0.668	2.618	5.083

^a From American Institute of Physics Handbook [45].

^b From D. Deirmendjian, R. Clasen, and W. Viezse [37] (based on data from Yolken and Kruger).

^c From H. C. Van de Hulst [27].

^d From D. Deirmendjian, R. Clasen, and W. Viezse. [37] (based on data from M. Centeno)

Table 2.6: Thermal Conductivities of Sample Alloys

Physical Properties of Alloys				
Property / Alloy	melt pt (°C)	Thermal Cond. (BTU) (in) (Hr) (ft ²) (°F)	Thermal Cond (W/cm °C)	Temp Coeff Exp (°C)
Ni 200**	1455	468	@ 0°C 0.94* @227°C 0.72* @727°C 0.72*	0.006
Monel 400	1300	151		
Monel **	1330		@ 0°C .213 *	0.002
Inconel 600	1355	109		
Inconel 617				
Inconel 718				
Incoloy 800		97		
Inco HX				
304 Stainless Steel			@ 0°C 0.168* @227°C 0.186* @727°C 0.255*	

* Ref. 12

** Ref. 13

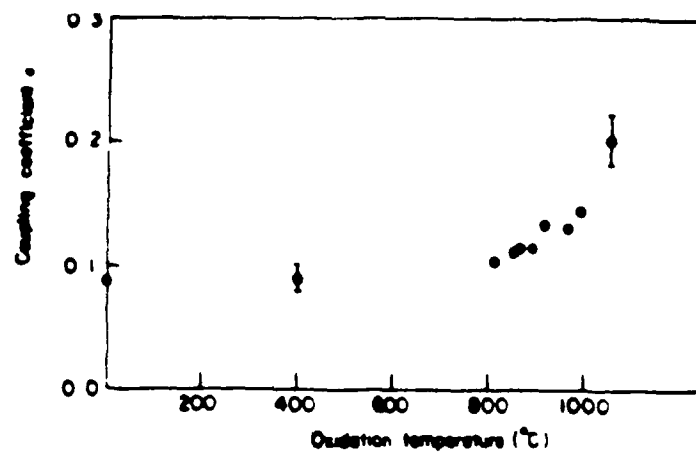


Fig. 2.14. Emissivity (@ 10.6 microns) vs. Temp. for 304 Stainless Steel for 1 min in air (Ref. 16).

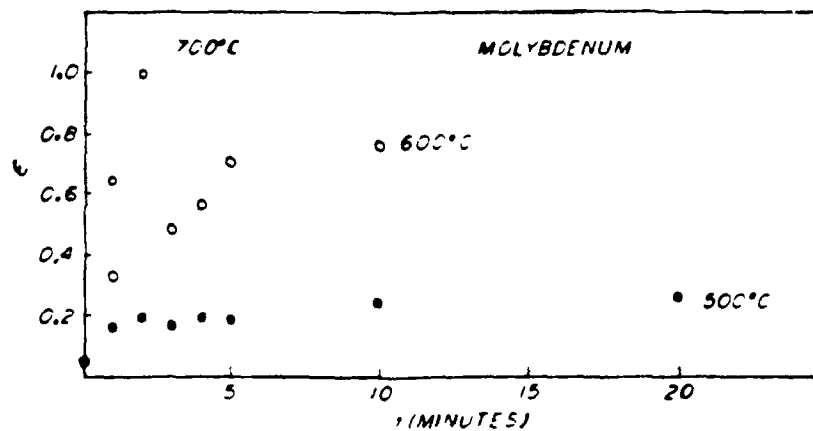


Fig. 2.15. Variation of Emissivity (@ 10.6 microns) for Mo with oxidation time at various temperatures. Oxidation is in air (Ref. 16).

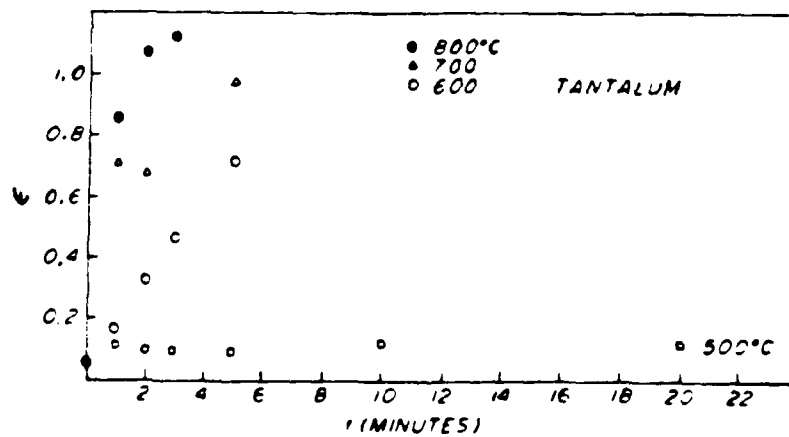


Fig. 2.16. Variation of Emissivity (10.6 microns) for Ta (Ref. 16).

Table 2.7: Thermal Diffusivities and Specific Heats of Sample Alloys

Physical Properties of Alloys					
Property / Alloy	Temp (°C)	Thermal Diff. cm ² Sec	Specific Heat J gm°C BTU lb°F		
Ni 200	25	.20	.46	.11	++
	0		.44	.105	**
	223		.52	.124	**
	723		.56	.133	**
Monel 400 Monel	25		.46	.11	++
	0		.42	.10	**
Inconel 600	0		.41	.098	**
	25		.50	.12	++
Incoloy 800	25		.50	.12	++
304 Stainless Steel	25		.50	.12	++
	0		.37	.088	**
	223		.383	.091	**
	723		.45	.107	**

** Ref 12

++ Watlow Corp.

Table 2.8: Compositions (wt. %) of Sample Alloys

ALLOY INFORMATION							
Composition/ Alloy	Cr	Co	Fe	Mn	Mo	Ni	Other
Ni 200						99	
Monel 400	0.1		1.0	1.0		67	31 Cu
Inconel 600	16		8.0	0.2		76	0.5 Si 0.04 C
Inconel 617	22	13.0	2.0		9.0	52	1 Al
Inconel 718	19		19.0	0.2	3.0	53	5 Nb 1 Ti 0.4 Al 0.3 Si
Incoloy 800	21		46	1		32	
Inco HX	22	2	19		9	47	1 Si
316 Stainless Steel	17		70			12	0.1 C

Table 2.9: Densities of Sample Alloys

PHYSICAL PROPERTIES OF ALLOYS				
Property / Alloy	melt pt (°C)	density (lbs/ft ³)	density (lb/in ³)	density (g/cm ³)
Ni 200	1455	554	0.321	8.890
Monel 400	1300	551	0.319	8.826
Inconel 600	1355	525	0.304	8.409
Inconel 617				
Inconel 718		527	0.305	8.440
Incoloy 800	1357	501	0.290	8.025
Inco HX				
316 Stainless Steel	1400	500	0.289	8.009

Losses

Blackbody gives

$$E_b = \sigma T^4$$

$$\sigma = 3.6574 \times 10^{-11} \frac{\text{Watts}}{\text{in}^2 \text{K}^4}$$

$$r = 0.265 \text{ inch}$$

$$t = 0.180 \text{ inch}$$

$$\text{Front Surface} = \pi r^2 = 0.2206 \text{ in}^2$$

$$\text{Back Surface} = \pi r^2 = 0.2206 \text{ in}^2$$

$$\text{Side} = 2 \pi r t = 0.2997 \text{ in}^2$$

$$\text{Total Surface Area} = 0.7409 \text{ in}^2$$

Losses are $E_b \times \epsilon$ where ϵ is the emissivity

Table 2.10: Radiative Losses for Samples During Heating

T (°F)	T (°C)	E_b (W /in ²)	with $\epsilon = .3$	with $\epsilon = .6$	with $\epsilon = .9$	Q1 (Watt) for $\epsilon = .3$	Q2 (Watt) for $\epsilon = .6$	Q3 (Watt) for $\epsilon = .9$
212	100	0.71	0.213	0.426	0.639	0.156	0.312	0.468
392	200	1.83	0.546	1.10	1.65	0.407	0.814	1.22
572	300	3.94	1.18	2.36	3.55	0.874	1.75	2.62
752	400	7.50	2.25	4.50	6.75	1.67	3.34	5.01
932	500	13.0	3.90	7.80	11.70	2.89	5.78	8.67
1112	600	21.2	6.36	12.72	19.1	4.71	9.42	14.1
1292	700	32.8	9.84	19.68	29.5	7.29	14.6	21.9
1472	800	48.5	14.55	29.10	43.65	10.8	21.6	32.4
1652	900	69.2	20.76	41.52	62.3	15.4	30.8	46.2
1800	983	91.0	27.30	54.60	81.9	20.2	40.4	60.6
1832	1000	96.0	28.80	57.60	86.4	21.3	42.6	63.9

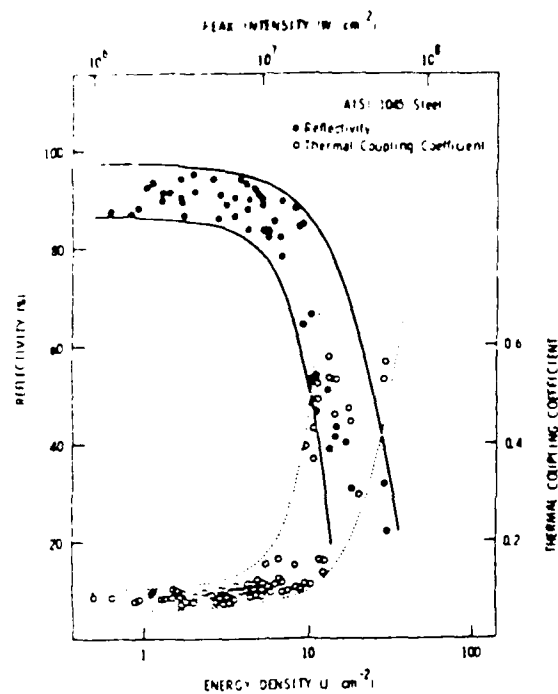


Fig. 2.17. Reflectivity & Thermal Coupling for
AISI 1045 Steel @ 10.6μ (Ref.4)

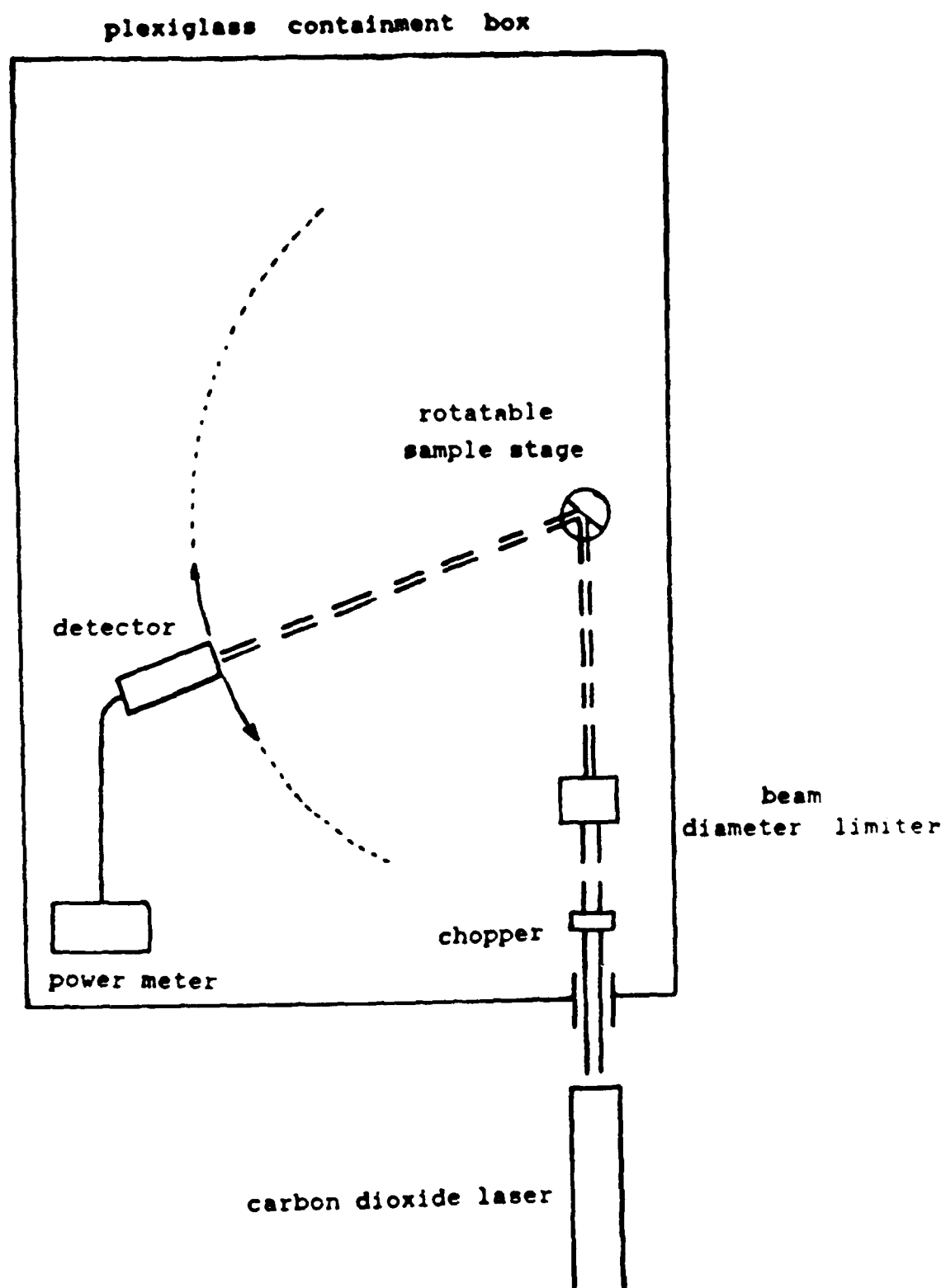


Fig. 2.18. Schematic of Experimental Aparatus

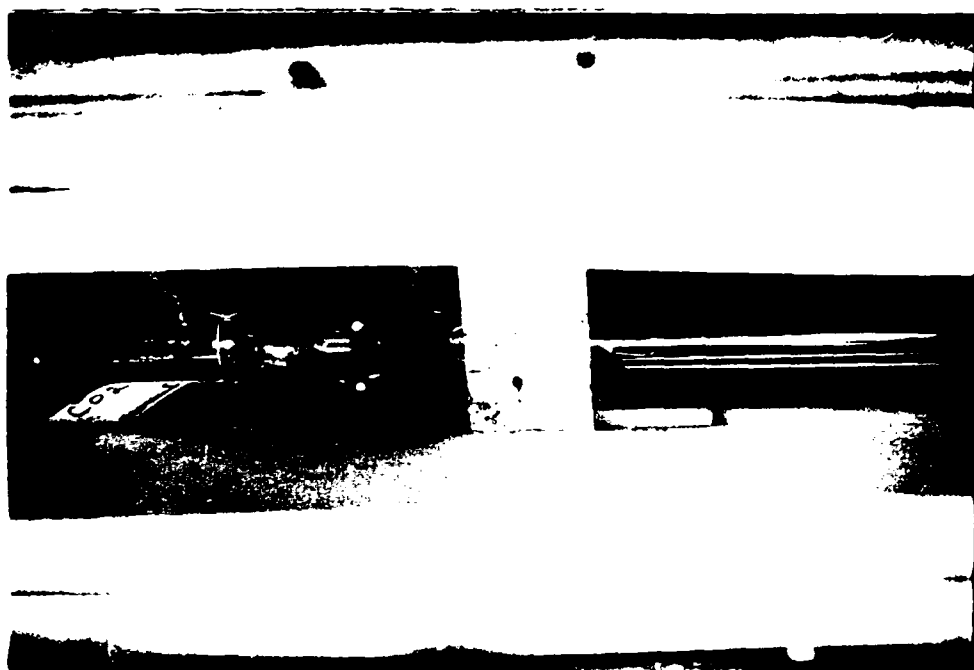


Fig. 2.19. Laser Condition Upon Arrival from WPAFB

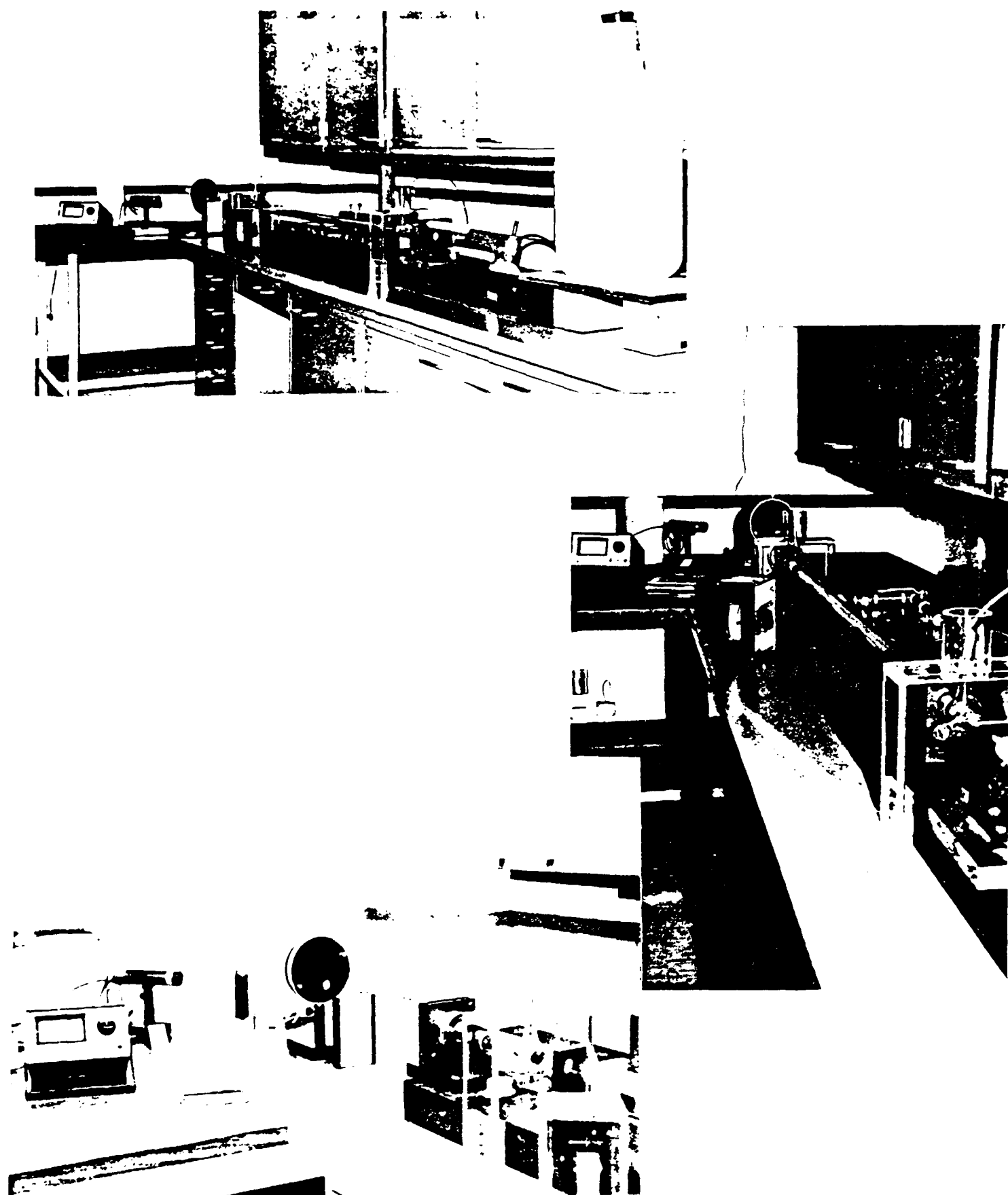


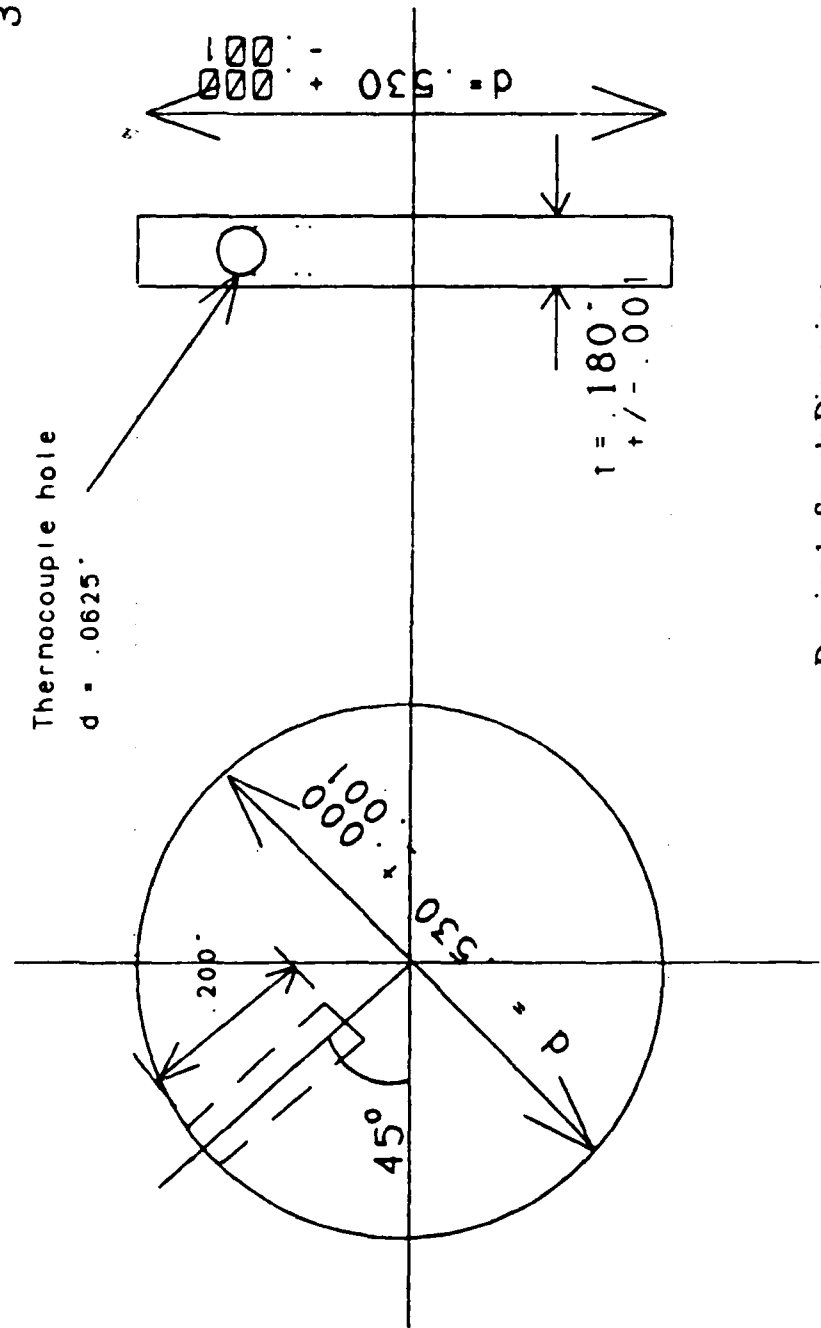
Fig. 2.20: CO₂ Laser with Partial Supply of Associated Equipment

Appendix A

Blueprints of Experimental Equipment Constructed at ASU

Sample Dimensions

Ni 200
 Monel 400
 Inconel 600
 Inconel 617
 Inconel 718
 Incoloy 800
 Inco HX
 316 Stainless

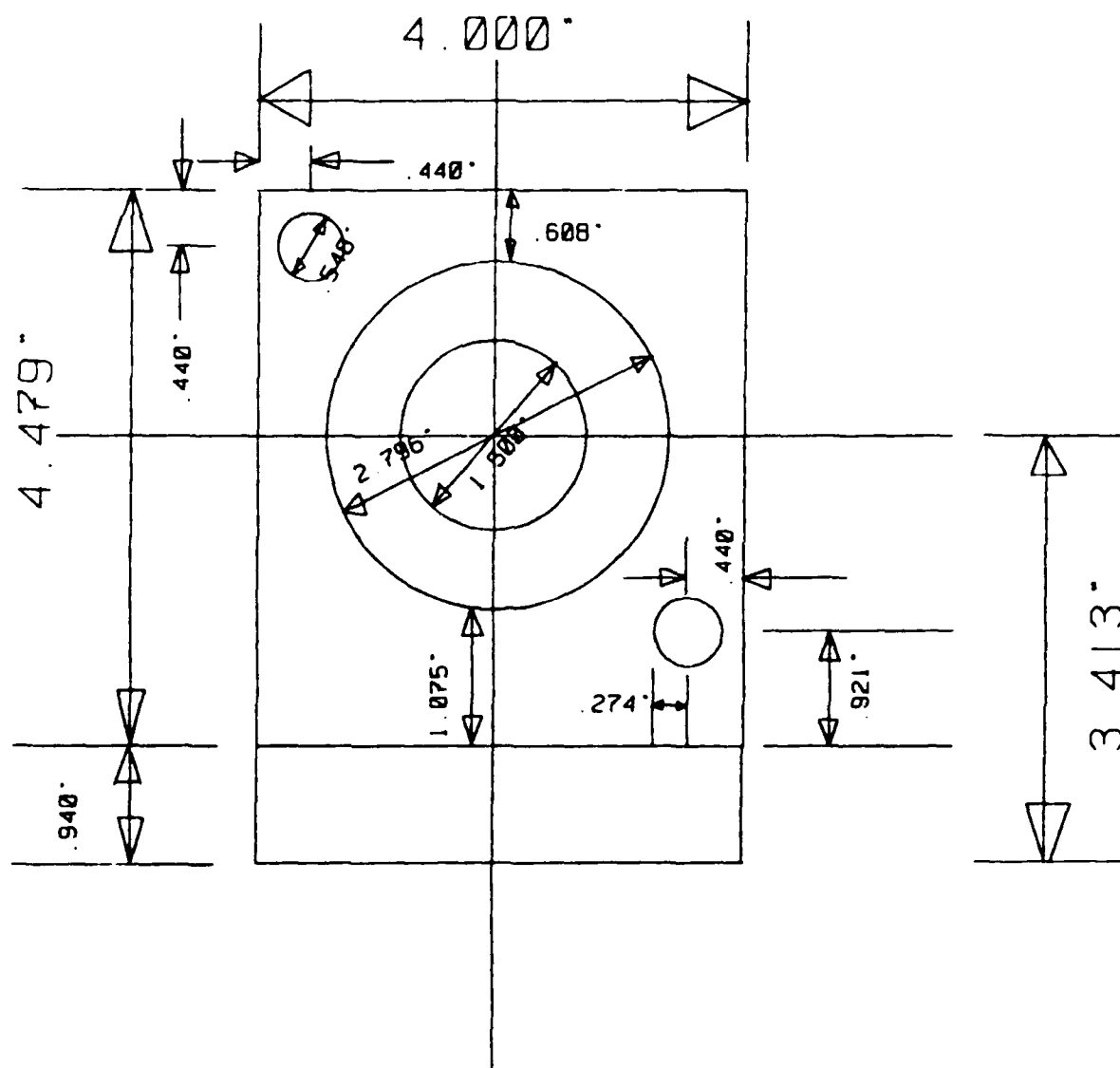


Drawing 1: Sample Dimensions

Laser Output

SCALE

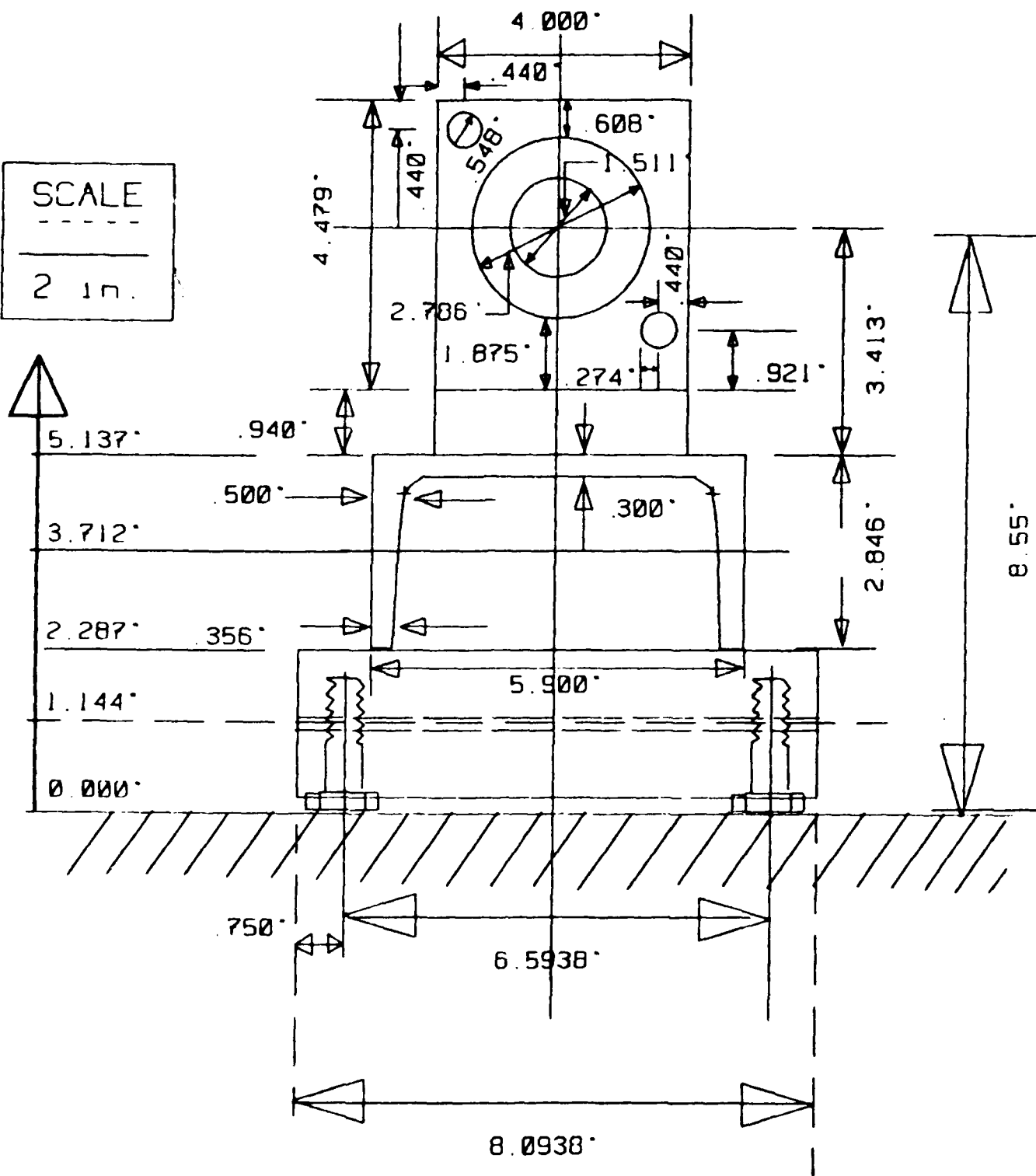
2 in.



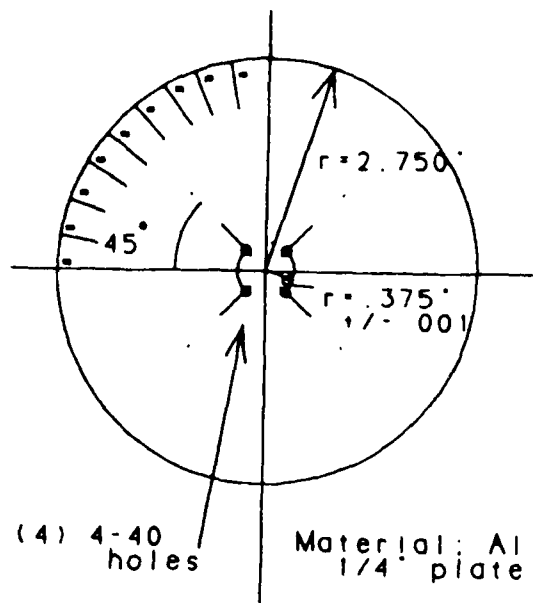
Drawing 2: Laser Output Dimensions

SCALE

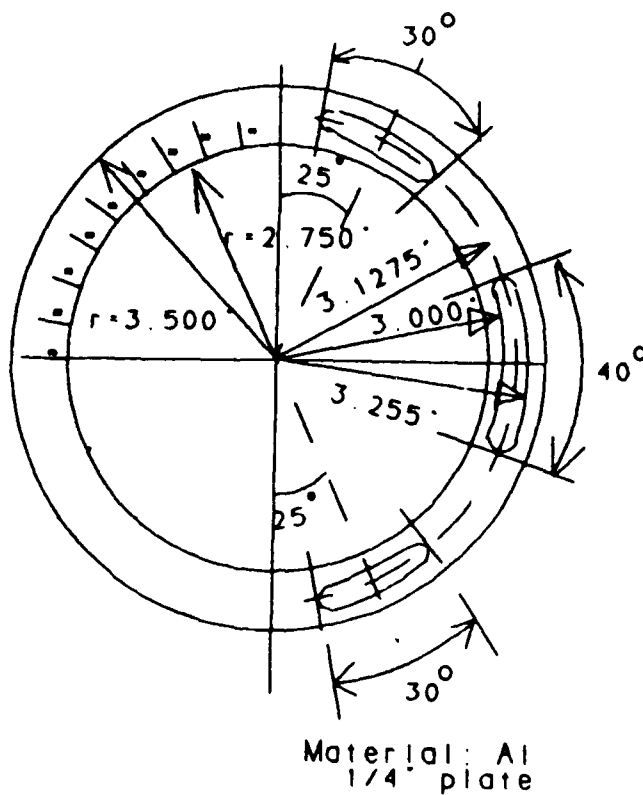
2 in.



Drawing 3: Laser Output Dimensions with Laser Bases and Leveler Included

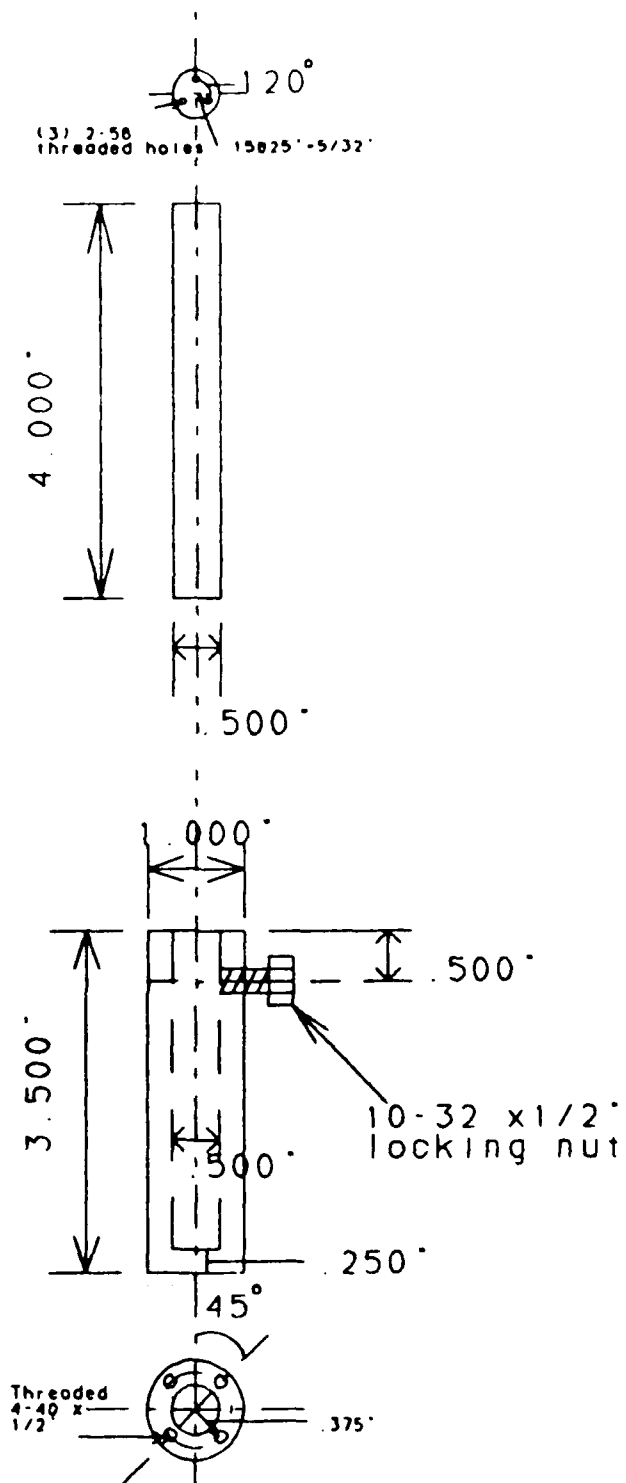


Piece 1



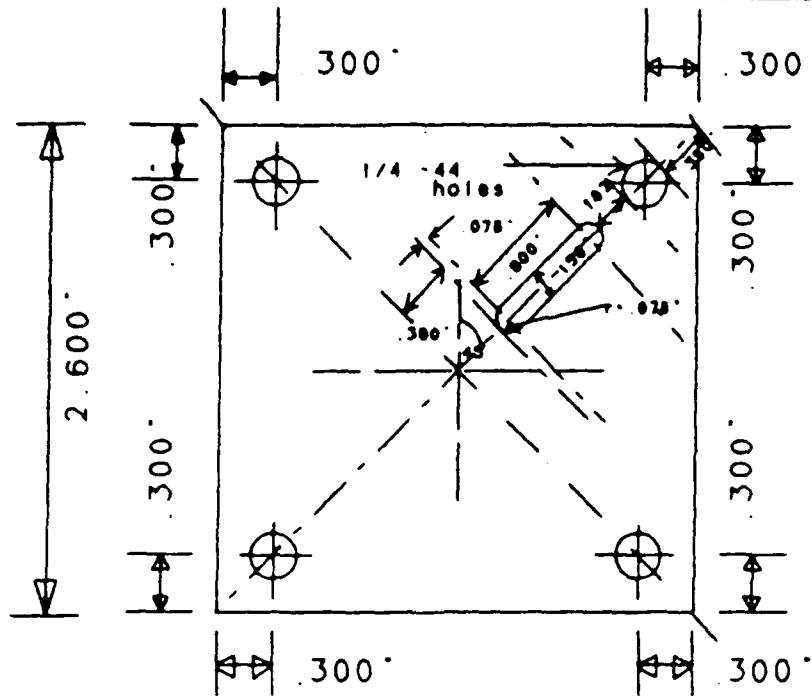
Piece 2

Drawing 4: Baseplates for High Temperature Sample Stage



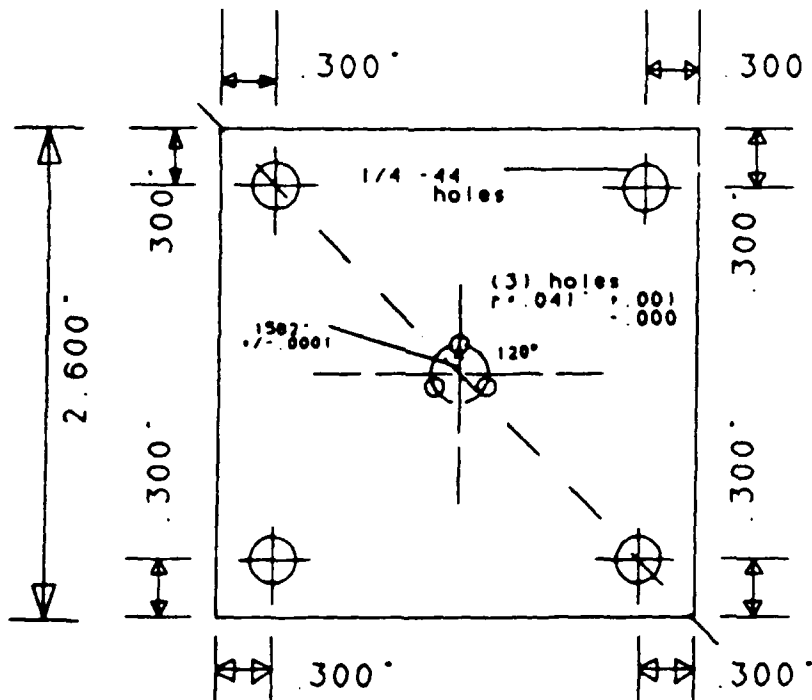
Specimen holder
rod & base attachment

Drawing 5: Stage Rod & Base Attachments



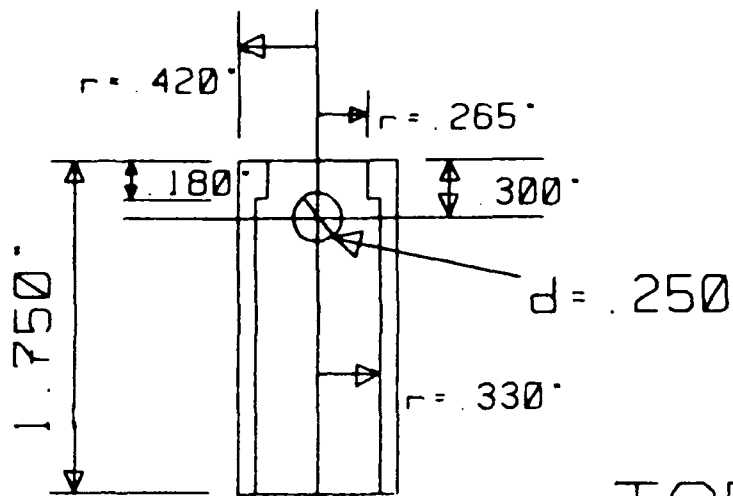
Material: Inconel 718

Bottom Plate

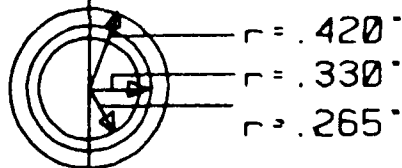


Material: Inconel 718

Drawing 6: Stage Balancing Plates

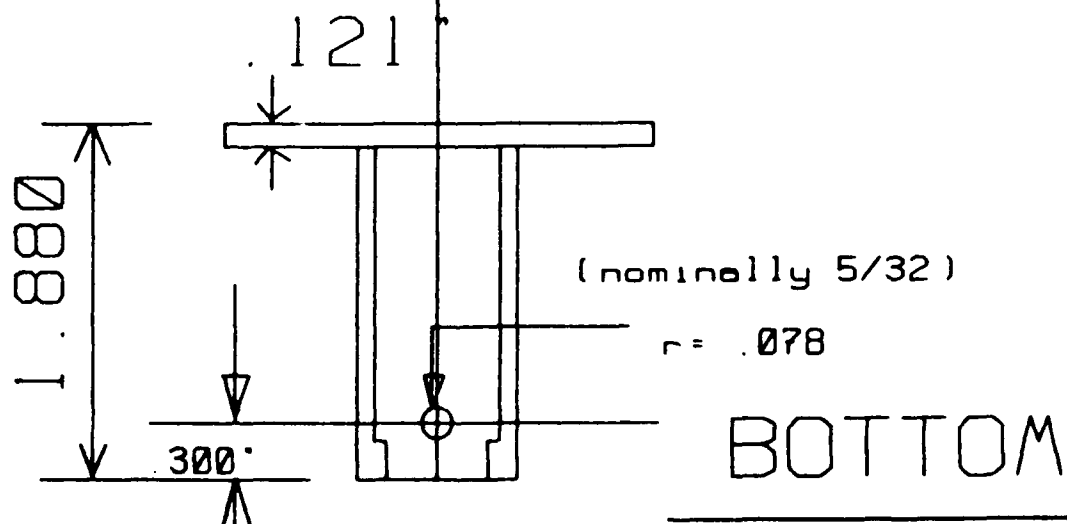


TOP



BACK

Material:
Inconel 601



BOTTOM

Drawing 7: Sample Holder

Safety Containment Box

Material

1/2" Plexiglass

36"

Vents

Beam Entry Port

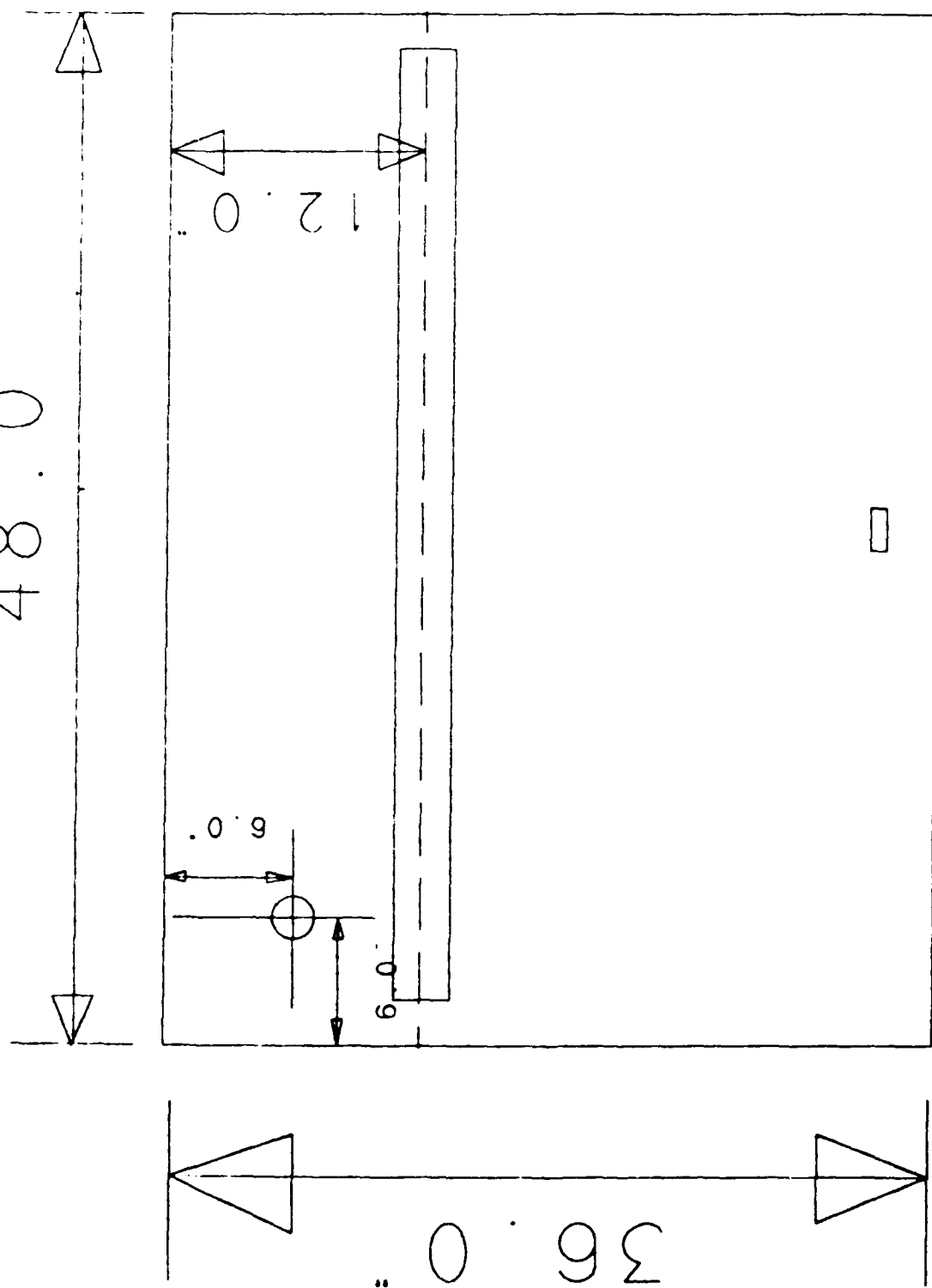
d = 2.5"

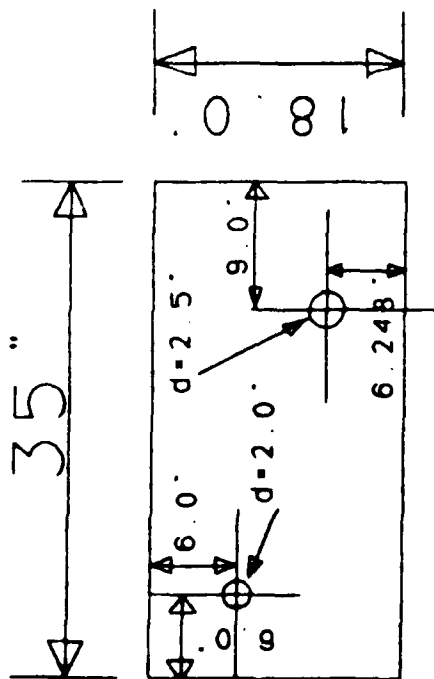
d = 2.0"

Drawing 8: Safety Containment Box

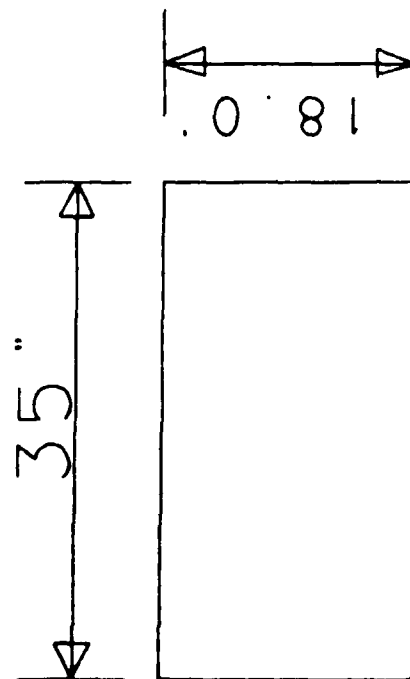
Material: 1/2" Plexiglass Top Panel

Drawing 9: Safety Containment Box Component

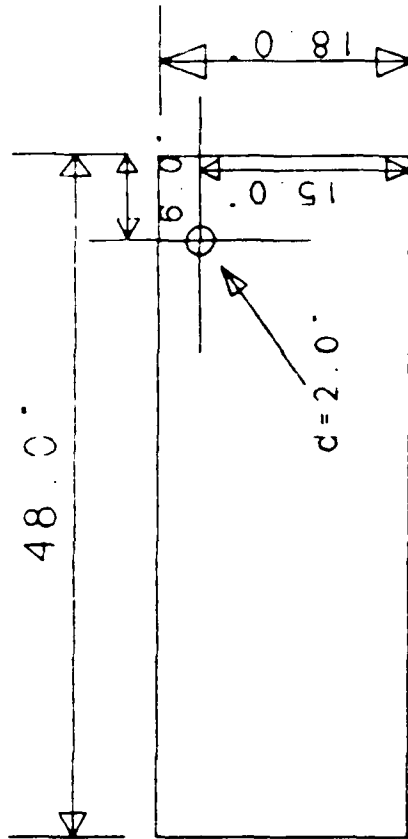




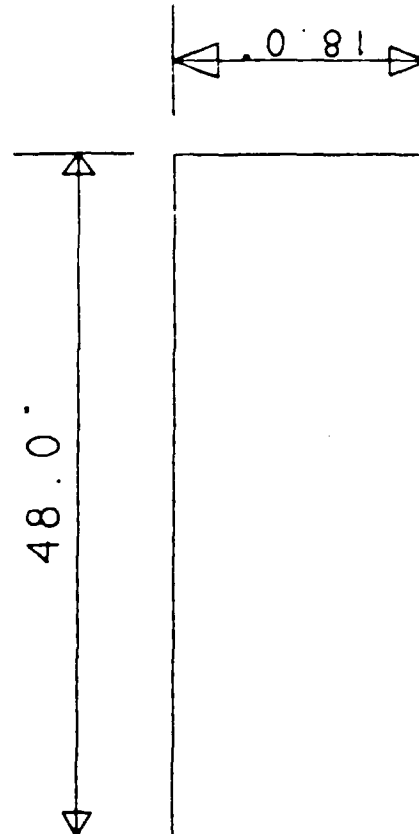
Front Panel



Back Panel



Right Panel



Left Panel

Drawing 10: Safety Containment Box Components